DTIC FILE COPY

AD-A217 202

Final Report
Contract N00014-84-K-0472; NR 650-025

# SPRAY DEPOSITION : A FUNDAMENTAL STUDY OF DROPLET IMPINGEMENT, SPREADING AND CONSOLIDATION

D. Apelian, A. Lawley and P. Mathur
Department of Materials Engineering
Drexel University
Philadelphia, PA 19104

December 1989

Approved for public release; distribution unlimited. Reproduction in whole or in part is permitted for any purpose of the United States government.

DTIC
ELECTE
JAN 26 1990
S E D

Prepared for
Dr. Donald E. Polk
OFFICE OF NAVAL RESEARCH
Code 1131, 800 N. Quincy Street
Arlington, VA 22217

90 01 25 057

# TABLE OF CONTENTS

Executive Summary 1

- Introduction 1
- Summary of Results 2

  A. Process Fundamentals 2

    Atomization 3
    Droplet Flight 3
    Spray Characteristics 4
    Droplet Consolidation 5
    Preform Shape 5
    Heat Transfer Parameters 5
    Preform Solidification 6
    Preform Microstructure 6

  B. Processing of HSLA Steels 7

    Preform Integrity 8
    Mechanical Properties 8

Attachments

Attachment 'A'

- List of Publications

Attachment 'B'

- Degrees Awarded

Attachment 'C' : Selected Published Papers on Spray Casting

- "Analysis of the Spray Deposition Process"
- "Spray Casting: A Review of Technological and Scientific Aspects"
- "Process Control, Modeling and Applications of Spray Casting"
- "Spray Casting of HSLA Steels"

DTIC COPY INSPECTED 1

Accession For
NTIS GRA&I ☒
DTIC TAB ☐
Unannounced ☐
Justification
By
Distribution/
Availability Codes
Dist | Avail and/or Special
A-1

# EXECUTIVE SUMMARY

This report summarizes the objectives, approach and salient results of the ONR program on spray casting at Drexel University over the last five years. It also includes three papers in Attachment 'C' to augment the contents of previous annual reports* by providing specific details of the research.

## Introduction

Spray casting via the Osprey™ process is emerging as a promising technology to produce near-net-shaped components of advanced materials. The process involves the sequential stages of gas atomization and droplet consolidation on a substrate to produce a disk, billet, tube and/or strip. The major advantage of spray casting is the ability to produce uniform, fine grained materials at deposition rates in the range 0.25-2.5 kg/s in a single operation from the melt. Composite materials can be manufactured by injecting second phase particles into the spray of droplets, or by in-situ reactions between the droplets and the gas during flight.

The objectives of the research program were two fold :

- *Process Fundamentals* : To develop a scientific understanding of the physical and thermal phenomena that are active during spray casting and which govern the shape and microstructural integrity of the preforms. Knowledge of the effect of key process parameters and the mathematical model which evolved from this analysis are generic to various shapes and sizes of components, and applicable to a variety of alloy systems. It is envisaged that this knowledge base, in conjunction with appropriate sensor and control schemes, will provide a means to extend the scope of current spray casting technology (e.g. production of tailored microstructures, knowledge-based control of spray casting, ...).

---

* *D. Apelian, A. Lawley, G. Gillen and P. Mathur, "Spray Deposition : A Fundamantal Study of Droplet Impingement, Spreading and Consolidation", ONR Technical Reports 1-4, NR 650-025, Contract N 00014-84-K-0472, Office of Naval Research, Arlington, VA (1984-1988)*

- *High Strength Low Alloy Steels* : To evaluate the Osprey process for processing bulk HSLA steels. A major advantage of the Osprey process appears to be its flexibility in terms of the choice and range of processing parameters, particularly for the HSLA-100 class of steels. These steels are difficult to process by conventional ingot metallurgy.

Experiments were conducted on the pilot scale Osprey spray casting facility at Drexel University under license from Osprey Metals Ltd. The equipment comprises (i) a 175kW melting and dispensing unit with a capacity of 30kg of steel, (ii) a gas distribution and atomizing system using Osprey atomizers, (iii) a spray chamber and preforming device to produce disk and tube components, (iv) a fluidized bed particle injector system for second phase particles, and (v) control panels.

A list of publications from research conducted on this program is given in Attachment 'A'. Student thesis details are given in Attachment 'B'.

## Summary of Results

We present a concise overview of our approach and the results of the research. More detailed descriptions of the approach, model formulation and experiments have been provided in previous reports and in Attachment A.

### A. Process Fundamentals

Due to the microscopic size of the droplets in the spray, and the small time intervals over which the processes occur, the Osprey process was analyzed by formulating a mathematical model using established tenets of heat transfer, phase transformations and fluid mechanics. Specific inputs for the analysis, and the model predictions, were assessed experimentally utilizing the Osprey spray casting facility at Drexel University.

The analysis was conducted in two component stages which occur in sequence, namely : (i) droplet gas interactions in flight, and (ii) droplet consolidation at the substrate. Modeling and experimental work in these stages was synthesized into an integral process model. The analysis describes the velocity and enthaply profiles of the droplets in flight, the heat and mass distribution in the spray vs flight distance, the build up of preform shape/geometry with different substrate configurations and motion, and the temperature distribution in the consolidated material during, and after, deposition. It also delineates parameters which affect the preform yield. Significant results are provided here for values of the process parameters normally in use on our Osprey facility.

*Atomization*

- The distribution of droplet sizes was determined by collecting droplets from the spray. The powders are spherical and have a smooth morphology; their size distribution is Gaussian. Typically, the mass-median droplet diameter $d_m$ is in the range 80-150μm for Cu-, Ni- and Fe-base alloys, in increasing order of $d_m$. The log-normal standard deviation $\sigma$ is 1.75–2.20, thus 95% of the droplets are in the size range 20-1000μm.

- Data on droplet sizes were correlated with the material and processing parameters using Lubanska's empirical relationship for atomization. The atomizer-specific constant $K_L$ and exponent m were found to be ~ 100 and 0.5, respectively, for the Osprey atomizer used. This correlation facilitates computation of $d_m$ and $\sigma$ under different processing conditions when experimental data are unavailable. $d_m$ can be decreased by increasing the melt superheat or gas:metal ratio. The substitution of argon for nitrogen as the atomizing gas does not lead to any significant effect on the droplet size distribution.

*Droplet Flight*

- Velocity of droplets during flight is primarily a function of their mass. Predicted droplet velocities on impact with the substrate are in the range 10-100 m/s for droplet sizes from 20-250μm, under standard operating Osprey conditions. Still photography with a 1/4000s exposure time confirms the predictions within an order of magnitude; accurate measurements of droplet size and velocity are currently limited due to the microscopic size of the droplets and the time scale of droplet flight (a few milliseconds).

- The variation of a droplet's temperature with flight distance can be divided into four stages. In Stage I, the liquid droplet cools ( and undercools) primarily by losing heat to the surrounding gas via forced convection, until the nucleation temperature is reached. In Stage II, the droplet nucleates solid and begins to solidify during recalescence up to the arrest temperature. Subsequent solidification (Stage III - "normal" solidification) occurs with an attendant drop in temperature and is governed by the rate of heat extraction by the gas. In Stage IV, the droplet cools in the solid state by forced convection.

- From theoretical calculations, and by estimating the extent of droplet solidification during flight (by intercepting droplets on glass slides), the degree of droplet undercooling $f$ (= fraction of the undercooling required for homogeneous nucleation) is found to decrease exponentially with increasing droplet volume. Thus, droplets smaller than the mean size (< 85μm for Fe-5 w/o Ti) are predicted to undergo an initial phase of partitionless solidification.

- Density, melting point and heat contained within the freezing range of the alloy are the three significant material parameters which affect the state of the droplets at impact :

(i) droplets of diameter less than a critical value d* are completely solidified upon impact. Typically d* is predicted to be in the size range 30μm-125μm for the alloys described; it increases with increasing melting point of the alloy.

(ii) droplets of diameter greater than d* impact the deposition surface in a "mushy" condition with varying fractions of liquid. These droplets comprise a solidified dendritic skeleton, as observed from glass slides. Their impact on to the deposition surface fragments the dendrites and generates many nucleation sites for deposit solidification .

(iii) only droplets greater than about 300μm for Al and 900μm for the other metals arrive at the deposition surface in a completely liquid state.

## *Spray Characteristics*

- The percentage of liquid in the spray is found to decrease rapidly with increasing flight distance during the initial stages, but subsequently the decrease is retarded. At operative spray heights of 300-400mm, the spray comprises 10-40 v/o liquid upon impact. Both melt superheat and gas:metal ratio affect the amount of liquid in the spray to a similar extent but in the opposite directions. Nitrogen is approximately four times more effective in cooling the spray than argon.

- Qualitatively, the width of the spray decreases with increasing gas pressure and/or gas:metal ratio.

## *Droplet Consolidation* :

- Only a portion of the droplets reach the substrate; this fraction is defined as the target efficiency of the spray, $\Pi_t$. Furthermore, only a fraction of the droplets arriving at the substrate "stick" and contribute to deposit growth; the remaining droplets "bounce-off". The fraction which adheres is termed the sticking efficiency, $\Pi_s$. Deposit yield is determined by the product of these two efficiencies. $\Pi_t$ depends upon the size of the substrate, the shape of the spray, the stand-off distance, the distribution of droplets within the spray and the substrate motion. Target efficiency for the production of a 120mm dia. disk preform is ~85%. $\Pi_s$ is a metallurgical parameter which is governed by the state of the spray at impact, the state of the top surface, the angle of incidence and by the substrate configuration/motion (e.g. rotation speed).

- Observation of droplets intercepted on glass slides suggest that the mode of deformation of the droplets on impact depends primarily upon the extent of their solidification. Small, fully solidified droplets ($<d_m$) undergo minimal deformation and have a spherical morphology with smooth surfaces. Larger, partially solidified droplets fragment along interdendritic regions, while the fully liquid droplets spread radially and splat with attendant jetting and cavitation.

## *Preform Shape*

- Under "standard" conditions of spraying onto a horizontal stationary substrate, the maximum deposit growth rate at the spray axis was ~ 5.25mm/s, and the radial distribution coefficient that governs the spread of the spray for the Gaussian distribution was ~0.0005mm$^{-2}$ for Fe alloys.

- Deposit/preform geometry is predicted by combining the variation of deposition rate across the spray cone with a mathematical description of the substrate motion. This model is used to predict the growth of the disk, tube and/or strip for any combination of substrate motion parameters.

## *Heat Transfer Parameters*

- Measured values of heat flux across the deposit-substrate interface show that the heat transfer coefficient is a maximum of ~$10^5$ W/m/K in the initial second but decreases to

~500 W/m/K during the bulk of the deposition period. This decrease is the result of the formation of an air gap between the deposit and the substrate.

- Heat transfer coefficient at the deposit-gas interface is estimated to be in the range 100-500 W/m$^2$/K, depending upon the gas pressure (6-10 bar), spray height (300-400mm) and angle of inclination.

*Preform Solidification:*

- In the initial stages of deposition, the deposit solidification rate is greater than the heat influx, thus impinging droplets impact a solidified top surface of the growing deposit. This rapid cooling results in a high degree of interconnected porosity (~14%) in the first millimeter of the deposited material.

- With continued time of deposition, the solidification rate decreases and the temperature at the top surface of the deposit begins to rise. A partially liquid layer forms on the surface of the deposit and increases in thickness during deposition. The deposit comprises two "layers" during its build up: (i) a bottom layer of solidified metal, and (ii) a partially liquid layer which contains decreasing amounts of solid from bottom to top.

- From the predicted thermal profiles across the deposit, and from temperature measurements within the sprayed deposits, it is concluded that the cooling rates during solidification of the bulk of the deposit are <100°C/s. Hence the solidification process occurs in two stages : a majority of the solidification occurs in flight at cooling rates in the range $10^3$–$10^4$ K/s while the remainder of the solidification occurs at <$10^2$ K/s.

*Preform Microstructure*

- The deposits exhibit a uniform distribution of equiaxed grains (20-200μm), no macrosegregation, a uniform distribution of second phases and the absence of prior particle boundaries (because of the presence of a partially liquid layer).

- Measured grain sizes in the deposit are approximately equal to, or less than, the mean droplet diameter but undergo extensive coarsening in single phase materials due to the slow second stage of cooling. The segregate spacing is smaller than estimates from the local solidification time because of the two-step solidification process, retarded coarsening of the dendrite arms at the high fraction of solid in the deposit, and/or nucleation by presolidified particles from the spray.

- Porosity in the deposit may arise from gas entrapment, inadequate feeding of liquid due to solidification shrinkage and rapid cooling. Except in the bottom zone of high interconnected porosity, the bulk of the deposit contains less than 1% porosity and the the pores are <1μm in diameter.

- The level of gas porosity is a function of the atomizing gas (either nitrogen or argon) used for atomization. An unreactive/inert gas (e.g. argon for superalloys) leads to a higher level of porosity since gas bubbles are trapped during deposition, while bubbles of reactive gases 'dissappear' by reacting with the metal/alloy.

- Since the mechanism of deposit solidification resembles liquid phase sintering, the level of porosity from shrinkage and cooling is governed by a balance between the solid/liquid ratio being deposited and the packing efficiency of the solid particles. Hot tearing may be encountered at the center of the disk if the parameters of motion are improperly set relative to the condition of the spray.

### B. Processing of HSLA Steels

This study was undertaken to assess the validity of fabricating bulk HSLA steels by spray casting. Preforms of HSLA-100, a low carbon bainitic, copper precipitation strengthened steel, were spray cast under differing conditions of superheat, atomizing gas (nitrogen) pressure, and preform cooling rate. Subsequently, portions of the spray cast material were subjected to thermomechanical processing.

Microstructure was characterized in terms of grain size and the extent of porosity. Tensile and impact properties, and microhardness, were evaluated in the spray cast, spray cast and aged, hot rolled and hot rolled and aged conditions.

*Preform Integrity*

- HSLA steels can be spray cast into bulk preforms of controlled shape. Internal integrity of the microstructure is reflected in acceptable levels and distribution of porosity, and an accompanying homogeneous grain structure. With the exception of occasional hot tears in the center of the preform, the spray cast microstructure is relatively insensitive to the spray casting conditions examined.

- The prior austenitic grain size in the preforms is relatively coarse (100-500μm), and depends on the location in the preform. This grain size range, and the accompanying coarse bainitic microstructure, are attributed to the loss of aluminum and niobium in melting and/or atomization. Hot rolling reduces the grain size to ~100μm. No significant changes in microstructure occur during aging.

*Mechanical Properties*

- After hot rolling, yield strengths >860 MPa and elongations ~20% are achieved in the HSLA-100. Toughness is also improved by hot rolling.

- Process optimization to eliminate fine-scale porosity in the spray cast preform is expected to result in attractive tensile and impact properties without the need for subsequent thermomechanical processing. The spray casting study has demonstrated that flexibility exists in terms of the choice of processing parameters; this is an advantage for this class of HSLA steels which are difficult to process by conventional ingot metallurgy.

# ATTACHMENT 'A'

## Publications on Spray Casting

Publications from Drexel University in the area of spray casting during the past several years are given below:

D. Apelian, B.H. Kear and H.W. Schadler, "Spray Deposition Processes", Rapidly Solidified Crystalline Alloys, AIME-TMS, Warrendale, PA, eds. B.H. Kear, S.K. Das, p.93,1986

G. Gillen, P. Mathur, D. Apelian and A. Lawley, "Spray Deposition: The Interaction of Material and Process Parameters", Progress in Powder Metallurgy, Metal Powder Industries Federation, Princeton, NJ, Compiled by: E.A. Carlson and G. Gaines, Vol. 42, p.753,1986

D. Apelian, A. Lawley, G. Gillen and P. Mathur, "Theoretical and Experimental Studies of Spray Deposition Processing", Horizons of Powder Metallurgy, Verlag Schmid GMBH, Freiburg, Germany,W.A. Kaysser and W.J. Huppmann, Part I, p.303, 1986

D. Apelian and G. Gillen, "Spray Deposition via the Osprey Process", Journal of Metals, Vol. 38, No. 12, p.44, 1986

G. Gillen, D. Apelian and A. Leatham, "Near Net Shape Manufacturing via the Osprey Process", Processing of Structural Metals by Rapid Solidification, ASM, Metals Park, OH, Compiled by: F.H. Froes and S.J. Savage, p.107,1987

D. Apelian, "Intelligent Particulate Processing, Net Shape Manufacturing and the Production of Novel P/M Microstructures", The International Journal of Powder Metallurgy, Vol. 23, No. 4, p.249,1987

A. Lawley, D. Apelian and P.C. Mathur, "Near Net Shape Manufacturing Via Particle Spray Deposition", Interdisciplinary Issues in Materials Processing and Manufacturing, ASME, New York, NY, eds. S.K. Samanta, et al, p.1,1987

S. Annavarapu, D. Apelian and A. Lawley, "Processing Effects in Spray Casting of Steel Strip", Metalurgical Transactions, Vol. 19A, p.3077,1988

E. Garrity, D. Wei and D. Apelian, "Modeling of the Spreading Kinetics During Droplet Consolidation Processing", Proceedings of Modeling of Casting and Welding Processes, Engineering Foundation, New York, NY, ed. T. Giamei, p.593,1988

P. Mathur, D. Wei and D. Apelian, "Modeling of the Solidification Process During Spray Casting", Proceedings of Modeling of Casting and Welding Processes, Engineering Foundation, New York, NY, ed. T. Giamei, p.275,1988

G. Gillen and D. Apelian, "Near Net Shape Casting via Droplet Consolidation", Proceedings of International Symposium on Casting of Near Net Shape Products,TMS-AIME, Warrendale, PA, ed. Y. Sahai, et al, p.225,1988

X. Luo, H. Li and D. Apelian, "Structure and Property Evaluation of Spray Cast Aluminum Alloys", Proceedings of Shenyang Intl. Symposium on Casting, Shenyang Foundry Society, Shenyang, PRC, p.219,1988

D. Apelian, A. Lawley, P.C. Mathur and X. Luo, "Fundamentals of Droplet Consolidation During Spray Deposition", Modern Developments in Powder Metallurgy, Metal Powder Industries Federation, Princeton, NJ, ed. P.U. Gummeson and D.A. Gustafson,Vol. 19, p.397,1988

G. Gillen and D. Apelian, "Spray Casting and Forming of Near Net Shape Components", Proceedings of the 1988 International Congress for Technology and Technology Exchange, Pittsburgh, PA, October 18-20,1988

P. Mathur, D. Apelian and A. Lawley, "Analysis of the Spray Deposition Process", Acta Metall, Vol. 37, No. 2, p.429,1989

D. Apelian and A. Meystel, "Knowledge Based Control of Materials Processing: Challenges and Opportunities for the Third Millennium", Metallurgical Processes for the Year 2000 and Beyond, TMS of AIME, Warrendale, PA, ed. Prof. H.Y. Sohn, p.183, 1989

D. J. Schaeffler, A. Lawley and D. Apelian, "Spray Casting of High Strength Low Alloy Steels", Advances in Powder Metallurgy, Compiled by T.G.Gasbarre and W.F.Jandeska, Vol. 2, p.161, Metal Powder Industries Federation, Princeton, NJ, 1989

D. Apelian and A. Meystel, "Knowledge Based Control in Materials Processing As Applied to Osprey Technology", Proceedings of Scaninject V, MEFOS and Jernkontoret, Lulea, Sweden, p.447,1989

D. Apelian and P. Mathur, "Spray Casting Fundamentals", Solidification Processing of Advanced Materials, OISO, Japan Society for Promotion of Science and NSF (USA), p.93, 1989

P. Mathur, S. Annavarapu, D. Apelian and A. Lawley, "Process Control, Modeling and Applications of Spray Casting", Journal of the Minerals, Metals and Materials Society, TMS, 41, No. 10, p.23,1989

S. Annavarapu, D. Apelian and A. Lawley, "Spray Casting of Steel Strip: Process Analysis", Metallurgical Transactions, In Press

P. Mathur and D. Apelian, "Evolution of the Solidification Structure During Spray Deposition (Osprey™ Process)", Proceedings of the Indo-US Workshop on Fundamentals of Solidification and Materials Processing, Hyderabad, India, January 15-18, 1988, In Press

P. Mathur and D. Apelian, "Spray Casting: A Review of Technological and Scientific Aspects", Book Series in P/M, eds. Jenkins and Wood, Vol.3, Inst. of Metals, London, In Press

P. Mathur and D. Apelian, "Osprey™ Process: Development of a Knowledge Base via Mathematical Modeling", Proceedings of the Conference on Intelligent Processing of Materials, TMS , Warrendale, PA, In Press

A. Lawley, D. Apelian, P. Mathur and A. Meystel, "Spray Forming: Process Fundamentals and Control", PM '89 - An Opportunity to Influence the Future, Conference Proceedings, The Institute of Metals, London, Paper 5.1, 1989

P. Mathur, D. Apelian and A. Lawley, "Spray Casting : Process Fundamentals, Modeling and Applications", Materials Science & Engineering, In Press

P. Mathur, D. Apelian and A. Lawley, "Fundamentals of Spray Deposition via Osprey Processing", PM'90, The Institute of Metals, London, UK, In Press

D. J. Schaeffler, A. Lawley and D. Apelian, "Mechanical Properties of Spray Cast High-Strength Low Alloy Steels", PM'90, The Institute of Metals, London, UK, In Press

D.J.Schaeffler, "Spray Deposition of High-Strength Low Alloy Steels", Proceedings Forty Seventh Electric Furnace Conference, Iron Steels Society, Warrendale, PA, In Press

# ATTACHMENT 'B'

## Degrees Awarded

The following degrees were awarded as a result of this research program :

- "A Study of Droplet Flight During Spray Forming", P.C.Mathur, M.S. Thesis, Department of Materials Engineering, Drexel University, May 1986
- "Analysis of the Spray Deposition Process", P.C.Mathur, Ph.D. Thesis, Department of Materials Engineering, Drexel University, May 1988
- "Spray Casting of HSLA Steels", D.J.Schaeffler, Department of Materials Engineering, Drexel University, May 1990

# ATTACHMENT 'C'

## Selected Published Papers on Spray Casting

"Analysis of the Spray Deposition Process"
Acta Metall, Vol. 37, No. 2, p.429,1989

"Process Control, Modeling and Applications of Spray Casting"
JOM-The Journal of the Minerals, Metals and Materials Society, 41, No. 10, p.23,1989

"Spray Casting: A Review of Technological and Scientific Aspects"
Book Series in P/M, eds. Jenkins and Wood, Vol. 3, Inst. of Metals, UK, In Press

"Spray Casting of High-Strength Low-Alloy Steels"
Advances in Powder Metallurgy, Compiled by T.G.Gasbarre and W.F.Jandeska, Vol. 2, p.161, Metal Powder Industries Federation, Princeton, NJ, 1989

Acta metall. Vol. 37, No. 2, pp. 429–443, 1989
Printed in Great Britain. All rights reserved

0001-6160/89 $3.00 + 0.00
Copyright © 1989 Pergamon Press plc

# ANALYSIS OF THE SPRAY DEPOSITION PROCESS

**P. MATHUR, D. APELIAN and A. LAWLEY**
Department of Materials Engineering, Drexel University, Philadelphia, PA 19104, U.S.A.

(*Received* 1 *February* 1988; *in revised form* 1 *June* 1988)

**Abstract**—Net or near net shape products can be manufactured by technologies involving solidification processing, metal forming, particulate processing, and droplet consolidation. One example of droplet consolidation is spray deposition in the Osprey™ mode. In this process, a stream of liquid metal is atomized by an inert gas to form a spray of molten droplets; these are accelerated towards a substrate where they impinge and consolidate. An integral model for the Osprey™ spray deposition process has been developed using established theoretical principles. Mathematical models describe the interconnected processes of droplet–gas interactions in flight and subsequent droplet consolidation on the substrate. The models predict droplet velocity and temperature as a function of flight distance, the extent of droplet solidification on arrival at the substrate, and temperature distribution in the consolidated material during deposition. This approach demonstrates the utility of modeling studies in order to establish quantitative guidelines for optimization of the process in terms of the evolution of microstructure in droplet consolidation.

**Résumé**—Des produits, de forme exacte ou approchée, peuvent être fabriqués selon des technologies qui font intervenir la solidification, la mise en forme des métaux, le frittage de particules, et la consolidation de gouttes. Un exemple de consolidation de gouttes est le dépôt par vaporisation en mode Osprey™. Dans ce procédé, un jet de métal liquide est atomisé par un gaz inerte pour former une vapeur de gouttelettes fondues; elles sont accélérées vers un support où elles se fixent et se solidifient. Un modèle intégral a été développé pour le mécanisme de dépôt par vaporisation Osprey™, à l'aide de principes théoriques bien connus. Des modèles mathématiques décrivent les processus interdépendants des interactions goutte–gaz en vol et de la consolidation ultérieure des gouttes sur le support. Ces modèles prévoient la vitesse des gouttes et la température en fonction de la distance de vol, de la proportion de gouttes solidifiées lorsqu'elles arrivent sur le support, et de la distribution des températures dans le matériau consolidé pendant le dépôt. Cette approche démontre l'utilité des études de modélisation quand on veut établir un guide quantitatif pour optimiser le processus en fonction de l'évolution de la microstructure dans la consolidation des gouttes.

**Zusammenfassung**—Werkstücke können in in endgültiger oder nahezu endgültiger From mit technologischen Verfahren wie Erstarrung, Ziehen und Verdüsen hergestellt werden. Ein Beispiel der Verdüsung ist das Aufsprühen mit der Osprey™-Methode. Bei dieser Methode wird ein flüssiger Metallstrom mit einem inerten Gas atomisiert und in einen Sprühregen von Tröpfchen verwandelt; diese Tröpfchen werden gegen ein Substrat beschleunigt, wo sie auftreffen und sich verfestigen. Mit eingeführten theoretischen Prinzipien wird für diesen Prozeß ein Gesamtmodell entwickelt. Mathematische Modelle beschreiben die miteinander zusammenhängenden Prozesse der Wechselwirkungen zwischen Tröpfchen und Gas im Flug und die darauf folgende Verfestigung auf dem Substrat. Das Modell ergibt Tröpfchengeschwindigkeit und -temperatur in Abhängigkeit vom Flugweg, das Ausmaß der Tröpfchenverfestigung bei Ankunft auf dem Substrat und die Temperaturverteilung in der verfestigten Schicht während der Abscheidung. Dieses Vorgehen zeigt den Nutzen von Modelluntersuchung für das Aufstellen quantitativer Richtlinien, mit denen der Prozeß hinsichtlich der Entwicklung der Mikrostruktur bei der Verfestigung der Tröpfchen optimiert werden kann.

## 1. INTRODUCTION

An intrinsic requirement of new processing technologies is net or near-net-shape capability [1, 2] in which the finished or nearly finished part is produced by the shortest route consistent with service and performance demands. The part must not only have the final shape needed, but it must also exhibit minimum property requirements. There are several approaches to net shape manufacturing of metallic materials; these utilize the generic technologies of solidification processing [1, 3] metal forming [1, 2, 4] particulate processing [1, 2, 4, 5] and droplet consolidation [6–8].

In this paper, attention is directed to droplet consolidation in which the material, in the form of a spray of droplets, impinges on a substrate to produce a thick deposit. Examples of droplet consolidation are low pressure plasma deposition/spraying [8] and the Osprey™ spray deposition process [6, 7]. In plasma deposition, the starting material is in the form of solid powder particles; upon injection into the hot plasma the particles melt and finally impact and consolidate at the substrate. The Osprey™ spray deposition process involves atomization of the alloy melt and impingement on the substrate with attendant consolidation. Spray deposition, spray forming, and spray casting are terms used to describe process involving droplet consolidation.

We present a model for the complex, interconnected Osprey™ process, since it is not amenable to analytical theory. Well established theoretical tenets of fluid mechanics, heat transfer and phase transformations have been combined to formulate a numerical model. It was also necessary to conduct specific experiments to arrive at input parameters for the model and to assess model predictions.

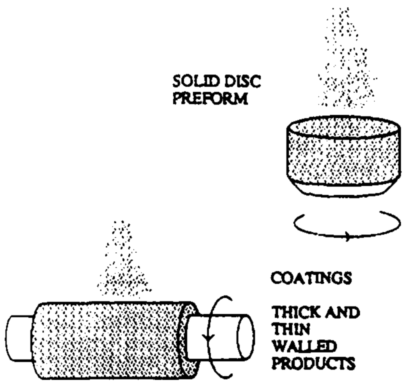

Fig. 2. Schematic of different shapes produced by spray deposition.

## 2. PROCESS DESCRIPTION

The droplet consolidation process analyzed here is Osprey™ spray deposition. A schematic of the process is given in Fig. 1. Briefly, the alloy charge is induction melted in a crucible located on top of the spray chamber. During melting, the chamber is purged with nitrogen gas and a slight over pressure of nitrogen gas is fed into the sealed crucible to prevent oxidation of the melt. The molten alloy exits through a refractory nozzle in the bottom of the crucible. In the atomizing zone below the crucible the molten metal stream is broken up into a spray of small droplets by nitrogen gas, typically at a pressure in the range 0.7–1.0 MPa. The liquid droplets are cooled by the atomizing gas and accelerated to the substrate where they impinge and consolidate to form a thick net or near-net shape deposit largely devoid of porosity. An on-line sensor linked to a microprocessor monitors the spray and the deposit during deposition, and adjusts processing conditions accordingly.

A number of shapes can be deposited by maneuvering the substrate beneath the spray, Fig. 2. For example, a solid cylindrical geometry is produced by spraying onto a rotating disc substrate. By spraying onto a rotating mandrel, coatings can be applied, or a thin or thick walled tube can be fabricated. Deposition onto a large diameter drum or wheel allows strip or sheet to be produced in a semi-continuous fashion. The major advantage of the process is that a near-net shape product can be fabricated in a single operation directly from the melt at deposition rates in excess of 0.3 kg/s. Metallurgically, the product exhibits a fine equiaxed grain structure with essentially no macroscopic segregation of alloying elements. More detailed descriptions of the Osprey™ process are given elsewhere [6, 7].

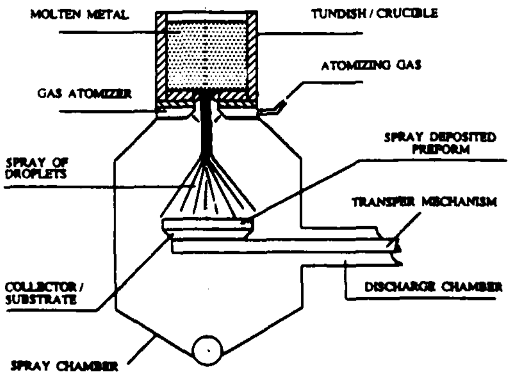

Fig. 1. Schematic of the Osprey™ process.

## 3. MODEL FORMULATION

The deposition process is depicted schematically in Fig. 3. There are two distinct stages of the process: one, where the droplets are in flight and interact with the atomizing gas, and the other where the droplets impact and interact with the substrate. In the first stage, the droplets generated by atomization are accelerated towards the substrate and cooled by the atomizing gas. Depending on size and hence cooling rate, the droplets are completely liquid, partially liquid, or completely solidified when they impact the substrate. In order to optimize the integrity of the

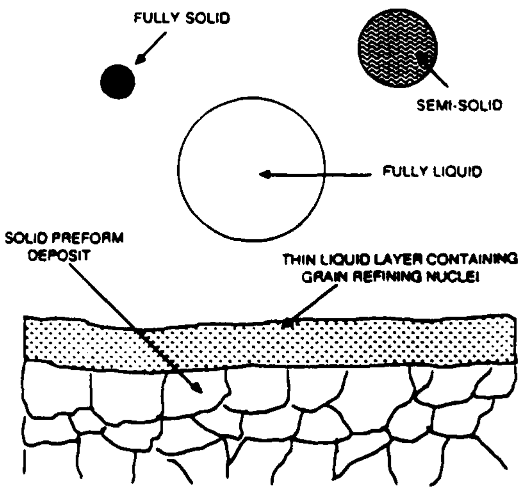

Fig. 3. Schematic of the spray deposition process.

deposit in terms of microstructure, it is necessary to determine the condition of the droplets prior to impingement, in terms of their heat content, size distribution and number density in the spray. Mathematical models are formulated which describe the droplet/gas interactions to predict the velocity and temperature profiles of the droplets in flight, and the progress of droplet solidification with flight distance.

In the second stage of the process, the droplets impinge, consolidate and solidify on the substrate to yield a deposit with an essentially homogeneous microstructure. Only the very first droplets make contact with the emplaced substrate while successive droplets impinge onto previously consolidated droplets. A heat transfer model is used to predict the temperature history experienced at any location within the deposit during its build-up. This is accomplished by taking account of the rate of heat and mass influx to the deposit from the spray of droplets, and the rate of external heat extraction. The predicted temperature profiles are subsequently used to determine the rate of advance of the solid–liquid interface, the local solidification time and the variation in microstructural features across the deposit thickness.

### *3.1. Droplet/gas interactions*

*3.1.1. Droplet velocity in flight.* The metal spray is comprised of droplets of differing diameter and the model considers a single droplet diameter at a given time in order to calculate velocity and temperature profiles along the droplet's flight trajectory. Similarly, this calculation is carried out for different droplet diameters. Individual droplets are treated as spheres and are assumed to follow a linear trajectory in flight. Each droplet will be accelerated to a point in flight where its velocity equals the instantaneous velocity of the atomizing gas, i.e. the relative velocity is zero. Beyond this flight distance, the droplet will travel faster than the gas and consequently it will be decelerated.

The velocity profile is determined from the momentum equation which relates the acceleration of a droplet to the velocity of the gas relative to the droplet. The total force ($F$) acting on a spherical droplet of diameter $d$ in a one-dimensional continuum gas flow is given by [9]

$$F = m\,(\mathrm{d}V_d/\mathrm{d}t) = (C_D \rho_g V_r^2 A/2) + \mathrm{mg} \tag{1}$$

droplet acceleration $= (\mathrm{d}V_d/\mathrm{d}t)$.

$$= \{3C_D\rho_g(V_g - V_d)|V_g - V_d|/4\mathrm{d}\rho_d\} + g. \tag{2}$$

Nomenclature of terms is given at the end of the paper and the values of specific parameters used in the model are listed in Appendix !I.

The drag coefficient, $C_D$, is related to the Reynold's number (Re) by [10]

$$C_D = 0.28 + [6/(\mathrm{Re})^{1/2}] + [21/\mathrm{Re}] \tag{3}$$

and

$$\mathrm{Re} = V_r d/v. \tag{4}$$

This equation is applicable over a wide range of Reynolds numbers ($0.1 < \mathrm{Re} < 4000$) with only a small deviation (±7%) from the standard drag curve.

The flight trajectory of the droplet is divided into short segments over which equation (2) is assumed to be valid. There is no analytical solution to equation (2); it is solved numerically at nodes separating the segments of flight [11].

*3.1.2. Droplet temperature and solidification in flight.* To model the temperature history and solidification of droplets, the schematic profile shown in Fig. 4 is adopted. For a given droplet, its initial temperature $T_i$ is determined by the degree of melt superheat. The droplet cools by losing heat to the surrounding gas by convection and radiation until the nucleation temperature $T_n$ is reached; this may be below the equilibrium liquidus temperature, as shown in Fig. 4. The operative heat balance is

$$Q_g = hS(T_d - T_g) + \sigma\epsilon S\,(T_d^4 - T_w^4) \tag{5}$$

where $Q_g$ is the rate of heat loss during flight and $h$ is the convective heat transfer coefficient. Heat loss from the droplet during flight can also be expressed as

$$Q_g = mC_d\,\Delta T/\Delta t. \tag{6}$$

The change in temperature $\Delta T$ over each time step $\Delta t$ can be calculated by combining equations (5) and (6). From the instantaneous droplet velocity, $\Delta T$ can be calculated over each segment of flight distance.

Heat transfer between the droplet and the surrounding gas is assumed to be interface controlled since the Biot number ($hd/K_d$) is $<0.1$. The convective heat transfer coefficient $h$ in equation (5) is then given by [12]

$$h = K_g(2 + 0.6\,\mathrm{Re}^{0.5}\,\mathrm{Pr}^{0.33})\,(C_{g(avg)}/C_g)^{0.26}/\mathrm{d}. \tag{7}$$

The specific heat ratio $C_{g(avg)}/C_g$ is included to account for the high temperature gradients in the gas immediately surrounding the droplet (13); where $C_{g(avg)}$ is the specific heat at an average temperature $(T_d + T_g)/2$.

In order to predict the droplet temperature profiles, it is necessary to know to what extent undercooling occurs. Two extreme conditions are considered: no undercooling (i.e. heterogeneous nucleation) and complete undercooling (i.e. homogeneous nucleation).

For homogeneous nucleation, the critical undercooling $\Delta T_c$ is given by [14]

$$(\Delta T_c/T_l)^2 = (16\pi\gamma^3)/[3\Delta H_f^2\,kT\ln(N)] \tag{8}$$

where $N$ is the number of atoms in the droplet and is therefore a function of droplet diameter. In terms of Fig. 4, $T_n = T_l$ if there is no undercooling, and $\Delta T_c = T_l - T_n$ for complete undercooling. If any undercooling exists in the droplets, the effect of recalescence must be included in the model. Nucleation at $T_n$ causes the temperature of the droplet to increase to a temperature $T_s$ due to release of latent heat, Fig. 4. Solidification is assumed to occur by the

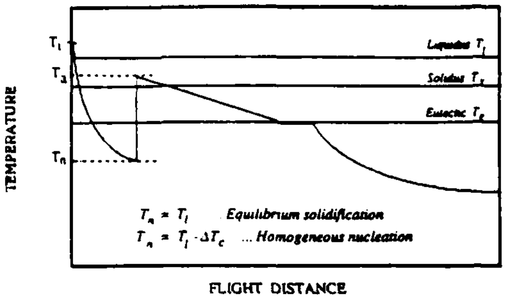

Fig. 4. Schematic temperature profile of a droplet in flight for an alloy composition with a mushy region.

growth of thermal dendrites into the supercooled melt. The problem is to determine the recalescence arrest temperature ($T_a$) and the fraction of the droplet that has solidified during recalescence ($f_s^r$).

The rise in temperature during recalescence is divided into short increments of temperature rise $\Delta T$, or increments of the fraction of the droplet that is solid, $\Delta f_s$. For progressively increasing values of temperature, the rate of heat release $Q_{re}$ from the solidifying droplet is given by

$$Q_{re} = \Delta H_f V_{dgv} A \rho_d. \tag{9}$$

The dendrite growth velocity $V_{dgv}$ is the only unknown in this equation; it can be determined from the Ivantsov equation for growth of paraboloid dendrites [15]

$$p \exp(p) E_1(p) = \Omega \tag{10}$$

where $p$ is the Peclet number given by Langer and Muller-Krumbhaar [16]

$$p = V_{dgv} r_{den}/2\alpha = (V_{dgv} d_0/2D\tau)^{0.5} \tag{11}$$

with the stability parameter $\tau = 0.025$.

$V_{dgv}$ decreases as recalescence proceeds. Consequently, $Q_{re}$ decreases during recalescence [equation (9)]. The limit in the increase of the droplet temperature (i.e. to the arrest temperature $T_a$) occurs when $Q_{re}$ is equal to $Q_g$ [as defined in equation (5)]. After recalescence is complete, further solidification of the droplet is dictated by the Scheil equation [17]. Transition from the recalescence stage to steady state Scheil conditions occurs via non-equilibrium partitioning of the solute, i.e. the partition coefficient is a function of the dendrite growth velocity [18, 19]. The final stage of cooling in Fig. 4 occurs totally in the solid state.

The actual undercooling of the droplets can be represented by the parameter $f\,(= \Delta T_{actual}/\Delta T_c)$, such that $f = 0$ with no undercooling and $f = 1$ for homogeneous nucleation. For given values of $f$ in the range $0 \leqslant f \leqslant 1$, the enthalpy of individual droplets at impact is predicted from the model of droplet temperature and solidification in flight described above. By the summation of the enthalpy of individual droplets, the average enthalpy of the spray at impact is determined as follows

$$H_{spray} = \Sigma H_p(d_i)\, d_i^3 f(d_i) / \Sigma d_i^3 f(d_i) \tag{12}$$

where $H_p(d_i)$ is the enthalpy of a droplet of diameter $d_i$ and $f(d_i)$ is the fraction of droplets of diameter $d_i$.

### 3.2. *Droplet/substrate interactions*

Microstructure across the deposit thickness is determined primarily by two competing parameters, namely deposition rate ($\dot{D}$) and the rate of solidification ($\dot{S}$). If the solidification rate is greater than the deposition rate, successive droplets impinge onto a solidified surface and a rapidly solidified microstructure is maintained throughout the deposit. If the deposition rate is greater than the rate of solidification, a liquid (or partially liquid) layer can form and grow. Solidification of this type, wherein the solid evolves from a liquid layer on the deposit surface, is termed "incremental solidification" [20].

To model the thermal profile of the deposit during spray deposition, values of the following parameters must be known:

(a) average heat content of the spray at the deposit surface ($H_{spray}$)

(b) deposition rate or increase in deposit thickness with time ($\dot{D}$)

(c) rate of heat removal by the substrate and the atomizing gas ($h_s$ and $h_g$ respectively)

(d) metal properties.

Factors (a) and (b) combine to yield the rate of heat input into the deposit, while (c) determines the rate at which heat is extracted from the deposit. A one dimensional heat balance is established in the direction of deposit growth to yield the change in enthalpy with time at any position within the deposit. This formulation uses factors (a), (b), (c) and (d) and accounts for the moving boundary at the deposit surface such that

$$\rho(\partial H/\partial t) = (1/L^2)[\partial/\partial\eta\,(K\partial T/\partial\eta)] + (\rho\eta/L)(\partial H/\partial\eta)(\mathrm{d}L/\mathrm{d}t) \tag{13}$$

where $L$ is the thickness of the deposit at any instant, $\eta = z/L$, $z$ is distance into the deposit measured from the substrate upwards, $H$ is the enthalpy at position $z$, $\mathrm{d}L/dt = \dot{D}$ is the rate of deposit build up (deposition rate) and $t$ is elapsed time from the start of deposition.

Enthalpy, rather than temperature, is considered in equation (13) to account for the latent heat released during solidification. The boundary condition at the deposit-substrate interface ($\eta = 0$) is

$$(K/L)/(\mathrm{d}T/\mathrm{d}\eta) = h_s(T_d - T_s) \tag{14}$$

where $h_s$ is the heat transfer coefficient at this interface.

The boundary condition at the top surface ($\eta = 1$) is

$$\rho\,(H_{spray} - H)(\mathrm{d}L/\mathrm{d}t) = K(\mathrm{d}T/\mathrm{d}\eta)/L + h_g(T_g - T_d) \tag{15}$$

where $h_g$ is convective heat transfer coefficient for gas cooling and $\rho\ H_{spray}\ (\mathrm{d}L\ \mathrm{d}t)$ is the heat flux input from incoming droplets.

Equation (13) is solved by an explicit finite difference numerical scheme [11] at grid points positioned along the deposit thickness. A finer grid is used in regions with high temperature gradients. While the total number of grid points is constant, the grid expands uniformly with time to account for the increase in deposit thickness during deposition. Grid point temperatures at time $t + \Delta t$ are calculated from the temperatures available at these locations at the previous time step, $t$. Therefore an initial estimate of the temperature profile along the deposit thickness is required at an infinitesimal time step after deposition begins. This information is provided by assuming a Newtonian heat transfer condition (i.e. no thermal gradients in the deposit) for the initial time step

$$\rho L(\mathrm{d}H/\mathrm{d}t) = h_g(T_g - T_d) + h_s(T_d - T_s) - \rho\,(H_{spray} - H)(\mathrm{d}L/\mathrm{d}t). \quad (16)$$

This asssumption of Newtonian heat transfer is justified for small $L$ when the Biot number $hL/K < 0.1$.

With a knowledge of the parameters $H_{spray}$, $\dot{D}$, $h_s$ and $h_g$, and the material properties, thermal profiles at any location in the deposit can be predicted as a function of time. The thermal profiles will differ from location to location due to a spatial variation in $H_{spray}$, $\dot{D}$, $h_s$ or $h_g$ within the spray cone.

An order of magnitude value for deposit-gas heat transfer coefficient ($h_g$) is obtained by an empirical formulation for cooling of flat plates by impinging gas jets [21]. This formulation relates $h_g$ to the velocity and thermal properties of the impinging gas by the following expression

$$(\mathrm{N}u/\mathrm{Pr}^{0.42}) = (W/R)((1 - 1.1\ W/R)/[1 + 0.1(\lambda/W - 6)W/R)]\,F(Re). \quad (17)$$

The function $F(\mathrm{Re})$ is defined as

$$F(\mathrm{Re}) = 2\,\mathrm{Re}^{0.5}(1 + \mathrm{Re}^{0.55}/200)^{0.5}. \quad (18)$$

## 4. EXPERIMENTAL

Experiments were conducted to provide data for the numerical models and to assess the model predictions. Experiments were carried out on the Osprey™ spray deposition facility at Drexel University. About 20 kg alloy charges were induction melted under a nitrogen cover, nitrogen was also used as the atomizing gas at a pressure of 0.85MPa (116 psi) [7]. Deposition was carried out on substrates positioned 400 mm below the atomization zone. Two alloys were spray deposited: Ni–20 wt% Cr and Fe–20 wt% Mn.

### *4.1. Experiments to determine model input parameters*

*4.1.1. Droplet size distribution.* The droplet size distribution is required in order to model the droplets in flight. For Ni–20 wt% Cr, the size distribution was determined by sieve analysis of the powders while patternation experiments were utilized to determine the size distribution of Fe–20 wt% Mn droplets.

In the patternation experiments, droplets were sampled at radial distances of 0, 26 and 50 mm from axis of the spray in concentrically placed copper tubes filled with water. A shutter mechanism was utilized to limit the sampling time to 5 s. Droplets collected at each of the three radial distances were filtered out and analyzed by digital image analysis of SEM micrographs of the particles, and by Laser Microtrac. Typically, over a thousand particles were examined to obtain the droplet size distribution at each radial distance. A population based distribution of droplet sizes was obtained; this was converted to a mass distribution by transforming the number of particles in each size range to an equivalent mass. The mass based size distribution was used to determine the fraction of droplets $f(d_i)$ of a given diameter $d_i$ in equation (12).

*4.1.2. Extent of droplet solidification with flight distance.* The extent of droplet solidification with flight distance was determined by intercepting droplets on glass slides at distances of 200, 275 and 350 mm from the point of atomization. The solidified droplets were examined by scanning electron microscopy to determine the largest solidified droplet ($d^*$) at each of the three flight distances. This variation of $d^*$ vs flight distance was used to determine the degree of undercooling of the droplets as described in 5.1.2.

A range of droplet sizes was observed on the glass slides. Small droplets were solid on impact with the slide; these have a spherical morphology with smooth surfaces. A fraction of the larger droplets was only partially solidified on impact with the glass collector plate and these fragmented along interdendritic regions. Droplets with larger amounts of liquid spread radially on the glass slide, and droplets that were completely liquid simply splatted on the glass collector plate.

*4.1.3. Deposition rate.* The deposition rate or spray density (number of droplets per unit area per unit time) is a maximum at the spray axis and decreases towards the periphery of the spray. In order to measure $\dot{D}$ as a function of $R$, the build up of deposits on stationary substrates was recorded with a video camera. The increment in deposit thickness with each time step yields the instantaneous value of $\dot{D}$. Although $\dot{D}$ varied with time, an average value over the complete deposition cycle was obtained as a function of the radial distance from the spray axis.

### *4.2. Experiments to assess model predictions*

*4.2.1. Droplet velocity.* The metal spray was examined by means of short exposure (0.00025 s) still photography over flight distances from 300 to 400 mm. The streak lengths recorded on the film were used to obtain the velocity of the droplets in the metal spray. Accurate measurement of droplet velocity by techniques such as laser doppler anemometry or holographic photography is difficult due to the high density of opaque droplets in the metal spray, a condition intrinsic to the geometry and normal operating condition of the Osprey unit.

*4.2.2. Thermal profiles within the consolidated material.* In order to measure the temperature profiles within the sprayed deposits, thermocouples were initially set at 0, 10, 20 and 40 mm above the stationary substrate surface at a radial distance of 12 mm from the spray axis. Type "*B*" (Pt.6%Rh–Pt.30%Rh) thermocouples were used and the bead (~1 mm dia.) was exposed in order to achieve minimal response times. Data from the thermocouples were recorded on a 12-bit data acquisition system at intervals of about 30 ms. A two color optical pyrometer was used to monitor the temperature of the top surface of the deposit.

## 5. PREDICTION AND ASSESSMENT OF MODELS

### *5.1. Droplet/gas interactions*

*5.1.1. Droplet velocity in flight.* The predicted variation in droplet velocity with flight distance is shown in Fig. 5, assuming droplets of sizes 20, 40, 80 and 130 $\mu$m dia. for Ni–20 wt% Cr alloy. Each droplet is accelerated from the point of atomization up to its peak velocity, which decreases with increasing droplet diameter. Peak velocity is attained at the flight distance at which the relative velocity $V_r$ is zero. The smaller the droplet diameter, the smaller is the flight distance at which peak velocity is attained. At any given flight distance, there is a range of droplet velocities which correspond to the spread of droplet sizes. The predicted range of droplet velocities at three representative flight distances is shown in Fig. 6. Measured values of droplet velocity are ≈ 100 m/s.

*5.1.2. Droplet temperature and solidification in flight.* For the condition of no undercooling ($T_n = T_l$, Fig. 4), projected temperature profiles for three droplet sizes are illustrated in Fig. 7. It is observed that, with increasing droplet size, the onset and completion of solidification are delayed to larger flight distances. More importantly, as the droplet size increases, the flight distance over which solidification occurs also increases; this increases the likelihood of mushy impact at a given flight distance.

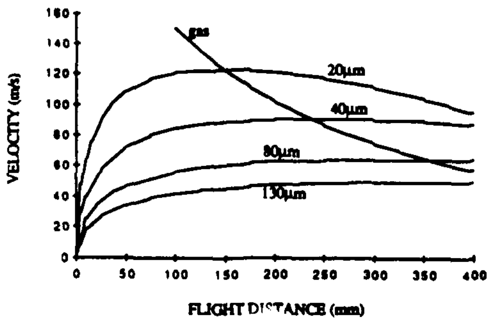

Fig. 5. Predicted variation of droplet velocity for Ni–20 wt% Cr droplets along the spray axis.

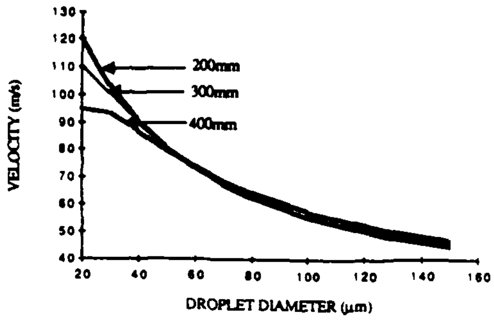

Fig. 6. Predicted droplet velocities as a function of droplet diameter and flight distance; Ni–20 wt%. Cr.

For homogeneous nucleation, the predicted dependence of droplet temperature on flight distance is shown in Fig. 8. Small droplets (40 $\mu$m dia.) undercool and recalesce. Larger droplets (80 and 130 $\mu$m dia.) experience lower cooling rates and the extent of undercooling is insufficient to give rise to homogeneous nucleation, at least for flight distances < 400 mm. Under a condition of homogeneous nucleation, undercooling is sufficiently large that $T_s$ is less than $T_e$, independent of droplet size. Thus, freezing is essentially instantaneous, and droplets are either completely solid (small droplets) or completely liquid (large droplets) at any selected flight distance; in

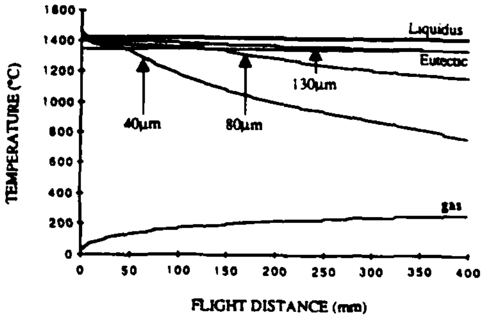

Fig. 7. Predicted variation of droplet temperature with flight distance for Ni–20 wt% Cr alloy; no undercooling.

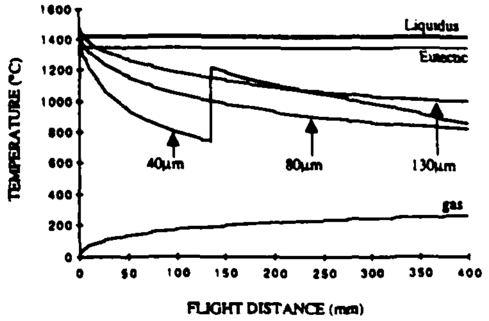

Fig. 8. Predicted variation of droplet temperature with flight distance for Ni–20 wt% Cr droplets; homogeneous nucleation.

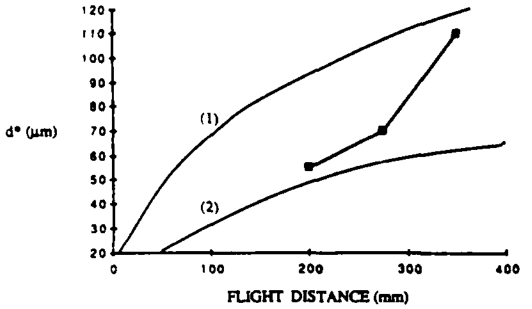

Fig. 9. Predicted variation of $d^*$ with flight distance for Ni–20 wt% Cr. Curves (1) and (2) are for heteroeneous and homogeneous nucleation, respectively. Experimental data (●) included for comparison.

contrast to the situation with heterogeneous nucleation.

From the calculated temperature profiles of droplets in the size range 20–150 $\mu$m, it is possible to predict the largest droplet size $d^*$ that will be solid at a given flight distance. The calculated dependence $d^*$ on flight distance is given by Curve 2 in Fig. 9 for the condition of homogeneous nucleation. For comparison, the corresponding relation between $d^*$ and flight distance for the condition of no undercooling is included as Curve 1 in Fig. 9. The measured values of $d^*$ are also included in the figure and lie between those two curves. This confirms that the predicted extremes regarding undercooling are valid. The trend in the experimental data suggests that nucleation occurs under nearly homogeneous conditions in small droplets, Fig. 9.

Using the experimentally measured variation of $d^*$ with flight distance for Ni–20 wt% Cr and Fe–20 wt% Mn (3 data points each), it was possible to back calculate the degree of undercooling of the droplets from the model of droplet temperature in flight. The calculation shows that $f$ decreases exponentially with droplet *volume*, Fig. 10. Knowing $f$, the enthalpy of individual droplets at impact, $H_p(d_i)$, is predicted as a function of their diameter, Fig. 11.

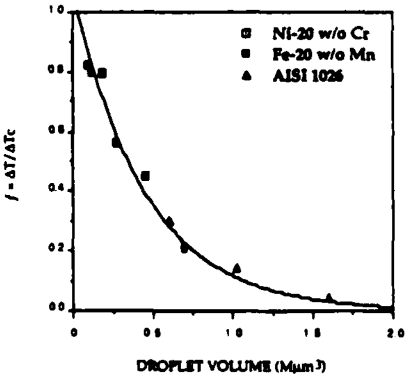

Fig. 10. Dependence of the degree of undercooling on droplet volume. $f = \Delta T_{actual}/\Delta T_c$ is the fraction of undercooling required for homogeneous nucleation.

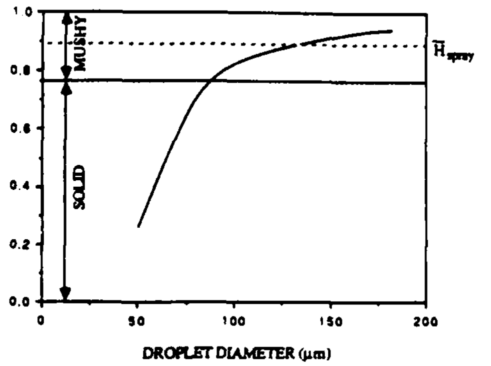

Fig. 11. Predicted enthalpy of Fe-20 wt% Mn droplets at impact as a function of their diameter. Average enthalpy of the spray $H_{spray}$ is also shown. Droplet trajectory is along the spray axis.

In order to calculate $H_{spray}$, use is made of the experimentally determined values of the droplet size distribution in the spray. For Fe–20 wt% Mn, representative log-normal size distributions by population and mass are shown in Fig. 12. Clearly, the population size distribution is bi-modal whereas the mass distribution is gaussian. A bi-modal population distribution indicates that the spray contains a large fraction of fine droplets; these are solidified on impact and become nuclei for the growth of fine, equiaxed grains in the deposit. The variation of mass-median droplet diameter with radial distance from the spray axis is derived from the size distributions; this is shown in Fig. 13. The log-normal standard deviation in all cases was approximately 1.75. Similar observations for Ni–20 wt% Cr show that the mass-median droplet diameter is 80 $\mu$m and the log-normal standard deviation is 1.80.

$H_{spray}$ was calculated by substituting $f(d_i)$ from Fig. 12 and $H_p(d_i)$ from Fig. 11 into equation (12). Summation was carried out from $d_i = 20\,\mu$m to $d_i = 200\,\mu$m in increments of 10 $\mu$m. It is convenient to represent $H_{spray}$ as the sum of two parts

$$H_{spray} = H_{solidus} + \phi\, H_{fr} \qquad (19)$$

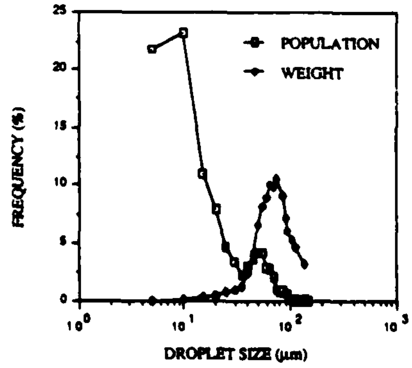

Fig. 12. Representative size distributions of Fe–20 wt% Mn droplets in the spray at a radial distance of 50 mm, flight distance = 400 mm.

where

$H_{solidus}$ is the enthalpy of the alloy at the solidus temperature

$H_{fr} = \Delta H_f + C\,\Delta T_f$ is the total amount of heat in the freezing range of the alloy, and

$\phi$ is a constant; $\phi = 0$ if the spray is totally solid and $\phi = 1$ if the spray is completely liquid.

The value of $\phi$ was determined as 0.28 under present deposition conditions; this implies that 72% of the heat in the freezing range is released during flight and the remaining 28% is carried into the deposit. $H_{spray}$ is converted to an average temperature of the spray, $T_{spray}$, which is calculated to be 1403°C for Fe–20 wt% Mn at a flight distance of 400 mm.

$H_{spray}$ decreases from the center of the spray ($R = 0$ mm, $\beta = 0°$) to its periphery ($R = 50$ mm, $\beta = 7°$) because droplets at the periphery travel greater flight distances before impact. Also, the smaller, colder droplets tend to be carried to the edge of the spray, whereas the larger, hotter droplets have greater inertia and remain at the center. By taking account of the variation in droplet sizes from the axis of the spray to its periphery (Fig. 12), the variation in $H_{spray}$ with $R$ at a flight distance of 400 mm was estimated to be <5%. Therefore this variation was neglected in subsequent computations and the heat content of impinging droplets is assumed to be nearly constant across the width of the spray.

### *5.2. Droplet/substrate interactions*

*5.2.1. Deposition rate.* Thickness profiles recorded during the build-up of a Fe–20 wt% Mn deposits are shown in Fig. 14(a). The dependence of $\dot{D}$ on $R$ is gaussian, and gives a good fit with the curve

$$\dot{D} = B \exp(-bR^2) \qquad (20)$$

where $B$ (maximum deposition rate) and $b$ (radial distribution coefficient) are determined as 5.25 mm/s and 0.0018 mm$^{-2}$ respectively, when $\dot{D}$ is expressed in mm/s and $R$ is in mm.

For deposition onto stationary substrates, a given location will have a fixed value of $\dot{D}$ corresponding to its distance $R$ from the spray axis. Movement of the substrate can be incorporated by changing the value of $R$, and therefore $\dot{D}$, with time depending upon the motion imparted.

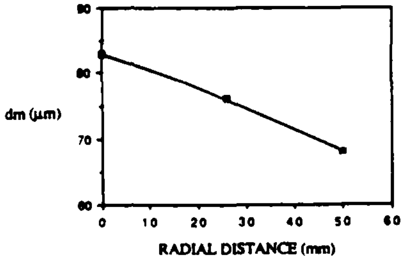

Fig. 13. Variation of mass-median droplet diameter with radial distance from the spray axis; Fe–20% Mn, flight distance = 400 mm.

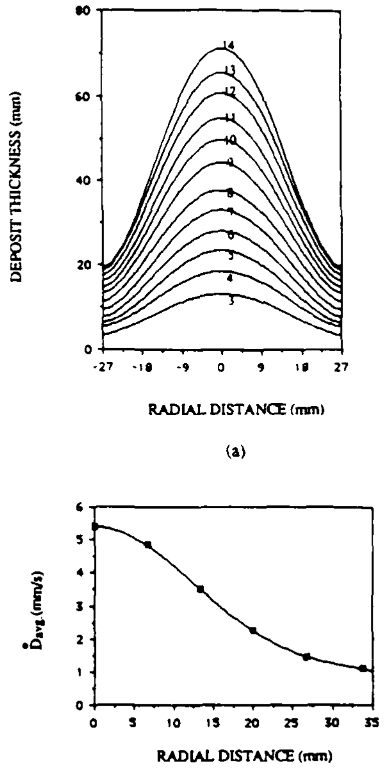

(b)

Fig. 14. (a) Thickness profiles at time intervals (sec.) from the start of deposition, and (b) dependence of time averaged deposition rate on distance from the spray axis.

*5.2.2. Heat transfer coefficients.* A value of $h_s = 10^3$ W/m²/K was used for the deposit/substrate heat transfer coefficient based on data available for similar solidification processes [22, 23]. Direct measurement of the heat extraction parameter will also be made when a suitable sensor becomes available; such a sensor is under development.

By substituting in values form Appendix I into equation (18), the deposit–gas heat transfer coefficient $h_g$ is approximately $2 \times 10^2$ W m² K.

*5.2.3. Thermal profiles in the deposit.* Temperature distribution across the deposit is calculated as a function of time from equations (13–15). Sample predictions are presented in Fig. 15 for the spray deposition of Fe–20 wt% Mn onto a stationary substrate positioned 400 mm below the atomization zone. The predictions supply to a location 12 mm from the spray axis where $\dot{D} = 4$ mm/s [Fig. 14(b)], $T_{spray} = 1403$°C, $h_s = 10^3$ W/m² K and $h_g = 2 \times 10^2$ W/m² K.

The thickness of the deposit increases linearly during deposition and remains constant thereafter, Fig. 15(a). Thermal profiles across the thickness of the deposit are obtained by drawing a vertical line at any instant of time. It is observed that the deposit comprises two "layers": (i) a bottom layer of solidified metal, and (ii) a partially liquid layer which

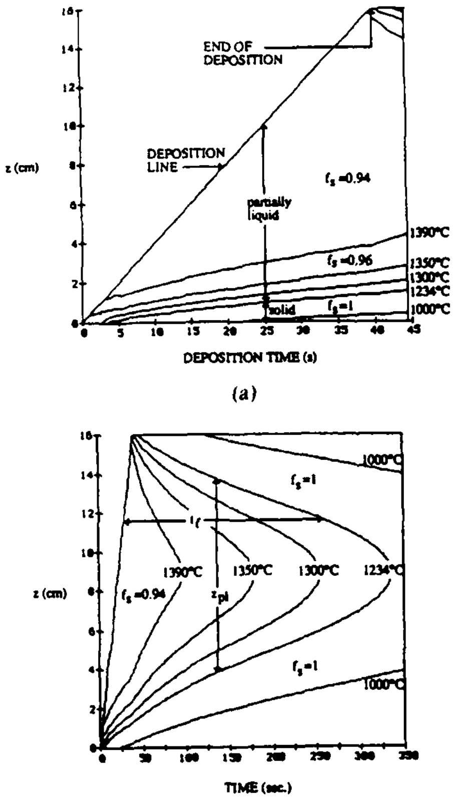

(a)

(b)

Fig. 15. (a) Predicted thermal contours across Fe-20 w/o Mn deposit during its build up; $\dot{D} = 4$ mm/s, $T_{spray} = 1403°C$, $h_s = 1000$ W m/K, $h_g = 200$ W/m/K, $R = 12$ mm (b) Predicted temperature profiles across Fe-20 wt% Mn deposit during and after deposition, showing, thickness of partially liquid layer $z_{pl}$, and local solidification time, $t_f$. Same conditions as in Fig. 15(a).

contains decreasing amounts of solid from bottom to top.

In the initial stages of deposition, the deposit cools rapidly due to quenching by the substrate. The solidification rate is greater than the deposition rate and therefore impinging droplets impact a solidified top surface of the deposit. This results in poor welding between successive droplets and leads to porosity within the deposit.

The rate of solidification or external heat extraction decreases with increase in deposit thickness. Consequently, the temperature of the top surface begins to rise and reaches a steady state value of about 1390°C ($f_s = 0.94$), Fig. 15(a). Thus, a partially liquid layer forms on the surface and increases with deposition time. This implies that the heat influx from incoming droplets exceeds the rate of heat removal by the substrate and the atomizing gas, i.e. the situation of $\dot{D} > \dot{S}$ is applicable. Clearly, this imbalance between heat influx and heat extraction must be controlled in order to maintain uniformity in structure throughout the deposit thickness. By the end of the spray deposition cycle only a tenth of the deposit is fully solidified; the remaining material is in a mushy state containing $0.94 < f_s < 1$.

Once deposition is completed, the heat influx is discontinued and the bulk of the deposit begins to solidify from this time, see Fig. 15(b). The liquid layer, $z_{pl}$, decreases in thickness from the top and bottom surfaces inwards due to heat extraction from these interfaces.

The variation of temperature with time at a specific height in the deposit above the substrate is obtained from Fig. 15 by moving along a horizontal line drawn at this height. Thermal histories at three different positions within the deposit (10, 40 and 80 mm above the substrate surface) are shown in Fig. 16. At the 80 mm location (i.e. the center of the deposit), for example, it takes 20 s for the deposit surface to build up to this height. Hence for the first 20 s from the start of deposition, the temperature remains at about 200°C. When the surface of the deposit reaches this location, the temperature increases rapidly to $T_{max}$; it remains constant at $T_{max}$ for about 50 s and then decreases. Solidification is completed when the temperature drops to 1234°C; the local solidification time at this height is ~300 s.

The interval between the deposition line and the $f_s = 1$ contour in Fig. 15(b) is a measure of the local solidification time, $t_f$. It is observed that $t_f$ increases rapidly over the initial thickness of the deposit, attains a maximum near the center, and then decreases due to gas cooling on the surface of the deposit.

Corresponding predictions of the model at a lower deposition rate of 2 mm/s [from $R = 23$ mm in Fig. 14(b)] are displayed in Fig. 17(a). Model predictions at a higher value of $T_{spray}$ ($T_{spray} = 1450°C$, $\dot{D} = 2$ mm/s) are shown in Fig. 17(b). $T_{spray}$ can be increased, for example, by decreasing the flight distance or by using argon as the atomizing gas. Increasing the deposition rate or the spray temperature [Figs 15(b), 17(a), and 17(b)]:

(a) increases the temperature of the top surface during deposition,

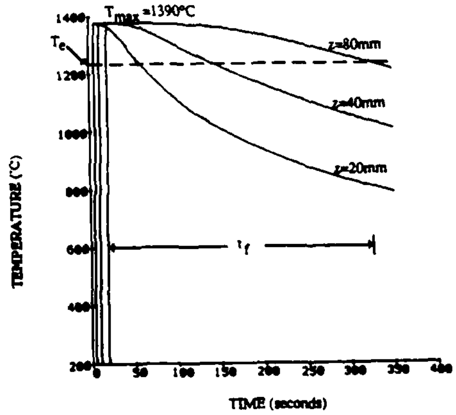

Fig. 16. Predicted temperature profiles at three heights ($z$) above the substrate surface; Fe-20 wt% Mn, from Fig. 15.

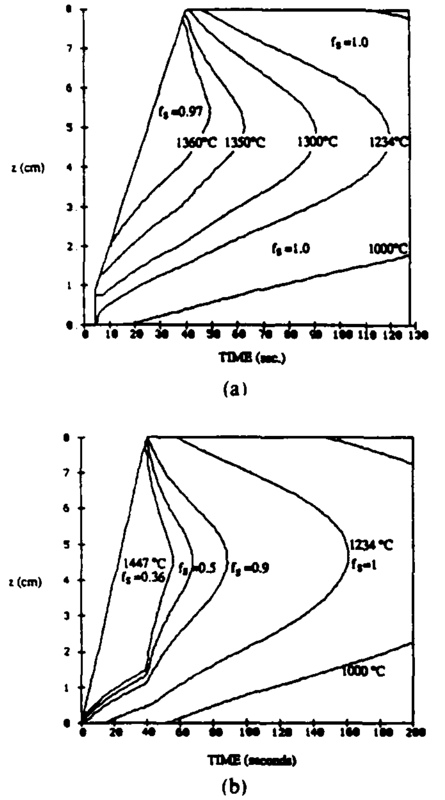

Fig. 17. (a) Predicted temperature profiles across Fe–20 wt% Mn deposit; $\dot{D} = 2$ mm/s, $T_{spray} = 1403$°C. (b) Predicted temperature profiles across Fe–20 wt% Mn deposit; $\dot{D} = 2$ mm/s, $T_{spray} = 1450$°C.

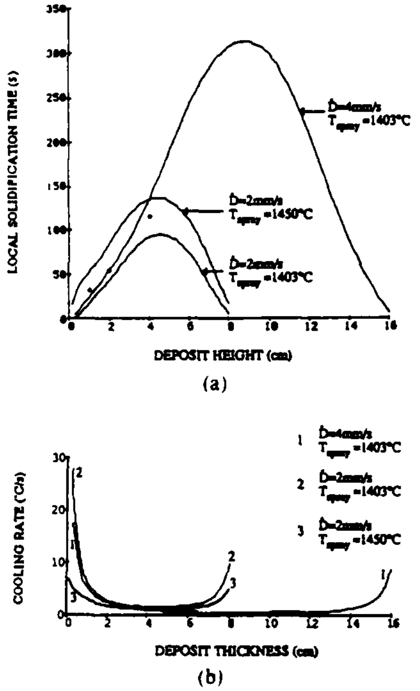

Fig. 18. (a) Predicted variation of local solidification time within the deposit with height above the substrate surface. Experimental data (●) included for comparison with the curve $\dot{D} = 4$ mm/s, $T_{spray} = 1403$°C. (b) Predicted cooling rates within Fe–20 wt% Mn deposit as a function of height above the substrate surface for three combinations of $\dot{D}$ and $T_{spray}$.

(b) increases the thickness of the partially liquid layer,

(c) decreases the fraction of solid in the liquid layer and results in a

(d) longer period of time for complete solidification.

An average cooling rate during solidification was calculated as follows

$$\dot{T} = \Delta T_f/t_f \tag{21}$$

where $\dot{T}$ is the cooling rate and $\Delta T_f$ is the temperature range over which soldification occurs. For example, $\Delta T_f = 1390–1234 = 156$°C for $\dot{D} = 4$ mm/s and $T_{spray} = 1403$°C. The predicted solidification times and average cooling rates are shown in Fig. 18 for the three combinations of $\dot{D}$ and $T_{spray}$ described above. Except in the initial zone $z_i$ which freezes rapidly ($\dot{S} > \dot{D}$), the deposit experiences nearly uniform cooling rates $<5$°C/s across its thickness.

The temperature profile recorded by one of the thermocouples set at $z = 20$ mm is displayed in Fig. 19. The initial rise in temperature (at $t = 0$) results from the start of the metal spray; droplets incident on the thermocouple tip consolidate to form a "bulb" around the exposed bead. At $t \approx 3$ s, the surface of the deposit reaches the bulb and a corresponding increase in temperature is observed. Due to bulb formation, the response time of the thermocouple is increased, and it takes a few seconds before the measured temperature reaches the actual temperature of the top surface. The local solidification time $t_f$ is measured as the interval between the second rise in temperature and the time at which the temperature decreases to 1234°C.

The experimental temperature profiles provide a direct comparison with model predictions displayed in Fig. 15 and 16 for $R = 12$ mm. The predicted

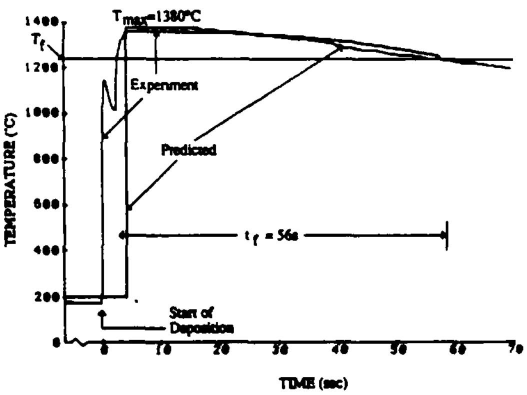

Fig. 19. Experimental and predicted temperature profiles within Fe–20 wt% Mn deposit at $z = 20$ mm above the substrate surface, $R = 12$ mm.

temperature profile at $z = 20$ mm is superimposed in Fig. 19 and shows good agreement with the experimental data. The local solidification time recorded by the thermocouples is in good agreement with model predictions in Fig. 19 and substantiates the validity of the model. The cooling rates are in agreement with previous measurements of the cooling rates in sprayed deposits using embedded thermocouples [24].

*5.2.4. Microstructure.* In order to relate thermal profiles to microstructure, deposits of Fe–20 wt% Mn were examined metallographically. Representative micrographs of samples taken 12 mm from the spray axis are shown in Fig. 20. The initial zone at the bottom surface has a fine martensitic structure consistent with rapid quenching by the substrate, Fig. 20(a). There is also evidence of prior particle boundaries that arise from insufficient welding between the liquid and presolidified droplets arriving at the substrate. Presolidified droplets result in a high level of porosity ($\sim 14\%$) in the deposit; the pores are irregularly shaped and are generally interconnected. The thickness of this porous zone is of the same order of magnitude as the thickness of the deposit $z_1$ which forms before the development of the partially liquid layer ($\approx 1$ mm). Therefore the lack of a partially liquid layer is associated with porosity and poor microstructural homogeneity within the deposit. With increasing radial distance from the spray axis, the deposition rate decreases and both, $z_1$ (predicted from the model) and the thickness of the porous zone (measured from the deposit), increase as shown in Fig. 21. At the periphery of the spray where the deposition rate is always smaller than the heat extraction rate, a high degree of porosity is maintained throughout the thickness of the deposit.

Above the initial zone $z_1$, the microstructure is homogeneous and comprises individual grains with no prior particle boundaries [Fig. 20(b)]. The density of the deposit is typically greater than 99% of theoretical density and the porosity is isolated and nearly spherical. The porosity can arise from solidification shrinkage, gas entrapment, insufficient liquid feeding or a combination of two or more of the above. The microstructure consists of austensite and

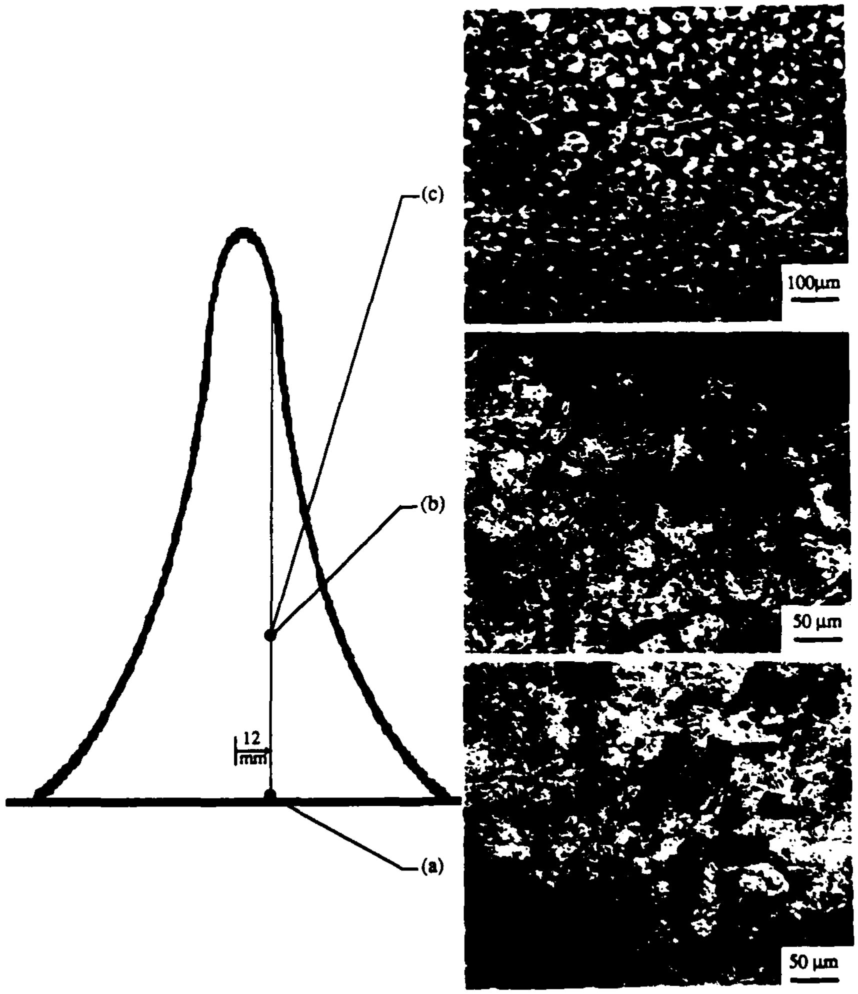

Fig. 20. Microstructure across the sprayed deposit of Fe–20 wt% Mn showing martensitic plates (in a and b) and solidification cells (in c).

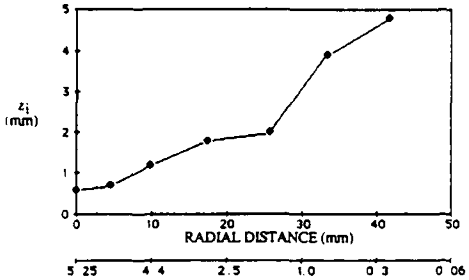

Fig. 21. Measured thickness of the initial porous zone in Fe–20 wt% Mn deposit as a function of radial distance and deposition rate.

hcp ε-martensite plates and is similar to conventionally solidified Fe–20 wt% Mn alloys [25, 26]. When the optical image is defocussed, the solidification cell size becomes discernible [Fig. 20(c)]; cell size was found to increase with deposit thickness, attain a maximum and then decrease towards the top of the deposit, Table 1. The segregate spacing within the deposits is the cell size, which is an order of magnitude larger than the dendrite arm spacing in overspray powders (Fig. 22).

The measured cell sizes were compared with segregate spacings predicted by the following empirical relationship for conventionally solidified Fe–20 wt% Mn [27]

$$DAS = 150\,(\dot{T})^{-0.25} \tag{22}$$

where $DAS$ is the dendrite arm spacing in $\mu$m and the cooling rate $\dot{T}$ is substituted from the model predictions. The experimentally measured and the computed values of the cell size are displayed in Table 1. Clearly, the measured values are significantly smaller than the cell sizes predicted by equation (22). This suggests that the nucleation density in sprayed deposits is greater than the nucleation density in conventionally solidified alloys. Nucleation during spray deposition can occur at two types of sites:

(a) solid particles from the spray, the number density of which can be estimated from the droplet size distribution and the model for droplet temperature profile in flight, and

(b) fragmented dendrite arms generated by the impact of mushy droplets. This is observed by microscopic examination of the top surface of the deposit, Fig. 23.

Based on the results of the theoretical and experimental studies described above, it is possible to describe the development of microstructure during spray deposition via the Osprey$^{TM}$ process. Except in the initial porous zone where $\dot{S} > \dot{D}$, the deposit undergoes a process of droplet remelting, grain nucleation and growth followed by solid state coarsening. The proposed sequence leading to the final microstructure of the deposit is summarized in Table 2.

Table 1. Comparison between predicted and measured cell sizes Fe–20 wt% Mn

| $z$ (mm) | $t_f$ (s) | Measured cell size ($\mu$m) | Predicted cell size ($\mu$m) [equation (22)] |
|---|---|---|---|
| 20 | 50 | 40 | 115 |
| 40 | 110 | 57 | 140 |
| 80 | 270 | 79 | 175 |
| 140 | 20 | 13 | 91 |

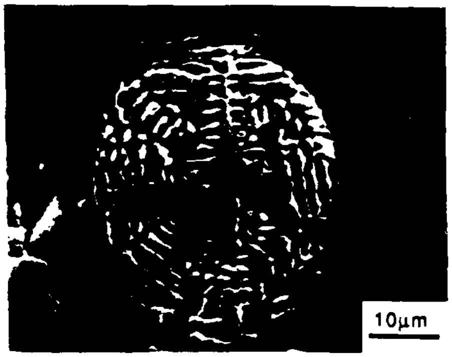

Fig. 22. Representative microstructure of Fe–20 wt% overspray powders; polished and etched.

## 6. CONCLUSIONS

From the model of droplets in flight in the Osprey$^{TM}$ spray deposition process, it is predicted that the velocity of Ni–20 wt% Cr droplets at impact is in the range 40–90 m s for droplet sizes from 20 to 150 $\mu$m.

In terms of temperature, the model predicts that the degree of undercooling $f$ decreases exponentially with increasing droplet volume.

The population-based distribution of droplet sizes in the metal spray is bi-modal whereas the mass-based size distribution is gaussian, on a log-normal plot. At a flight distance of 400 mm, the mass-median droplet diameter varied from 83 $\mu$m at the spray axis to 68 $\mu$m at the spray periphery. The log-normal standard deviation was approximately 1.75 in all cases.

By summation of the enthalpy of individual droplets at a flight distance of 400 mm, it was found that

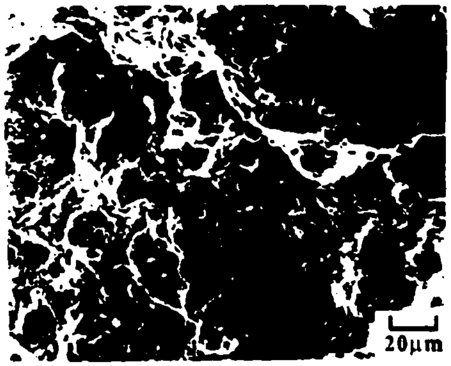

Fig. 23. Micrograph of a lightly polished and etched top surface of Fe–20 wt% Mn deposit showing presolidified droplets and fragmented particles.

Table 2

| *Microstructural Evolution* | *Evidence* |
|---|---|
| Input to deposit = solid, partially solid and liquid droplets of different $f_s$ and temperature | *Spray simulation model, glass slide experiments and patternation* |
| Droplets land onto hot, partially liquid surface of the deposit (with $f_s > 0.8$) | *Model of deposit heat transfer and optical pyrometer recordings* |
| Solid droplets ($< d^*$) retain shape and size on impact, partially frozen droplets shatter interdendritically and liquid droplets splat | *Observation from glass slide experiments and morphology of deposit top surface* |
| Liquid wets solid particles. Localized heat flow from liquid to solid particles, leading to:<br>(a) Interdendritic remelting<br>(b) Solid remelting<br>Remelting of solid continues until local temperature equilibrium is achieved. Remaining solid particles become nuclei for grain growth | *No prior particle boundaries in bulk of deposit*<br>*Difference between powder and deposit microstructure* |
| Growth of nuclei with attendant drop in local temperature, until $T_s$ is reached (end of $t_f$) | |
| Fine grain size due to high nucleation density from droplets remaining after remelting stage<br>Large $t_f$ or low solidification rate | *High density of broken dendrites on deposit surface + bimodal size distribution*<br>*Predicted vs measured cell sizes*<br>*Theoretical and experimental values* |
| Solid state coarsening of the solidification structure | *Extensive coarsening in pure metals vs limited coarsening in alloys with grain boundary precipitates* |
| No partially liquid layer initially. Grows rapidly during deposition until *majority* of the deposit is mushy (S + L) | *Structure changes rapidly in initial stages while layer forms, and then remains nearly constant due to large $t_f$* |
| Porosity is related to the formation of the partially liquid layer, i.e. to $\dot{D}$ | *Thickness of initial porous layer vs $\dot{D}$* |

the spray retains ~28% of the enthalpy in the freezing range of the alloy.

The dependence of deposition rate on radial distance from the spray axis is gaussian. The maximum deposition rate and radial distribution coefficient were determined to be 5.25 mm/s and 0.0018 $\text{mm}^{-2}$ at a flight distance of 400 mm.

From the predicted thermal profiles across the deposit, and from temperature measurements within the sprayed deposits, it is concluded that the cooling rates during solidification of the bulk of the deposits are $< 5^\circ\text{C/s}$.

Except in the initial zone $z_c$, the deposit solidifies from a partially liquid layer that forms on the surface during deposition. The layer grows rapidly until a majority of the deposit is mushy by the end of deposition ($0.9 < f_s < 1.0$). Inspite of the slow cooling rates, the deposits exhibit a fine grained, equiaxed microstructure; measured cell sizes are smaller than those predicted for conventionally solidified alloys. This suggests that the solidification process in spray deposits involves a higher density of nucleating sites.

The model predictions provide a base to describe the evolution of microstructure in spray deposits and to quantify the effects of various process parameters on the resulting structure. The model can be applied to simulate the build up of different shapes by incorporating substrate motion and or motion of the metal spray.

*Acknowledgements*—The authors wish to acknowledge the valuable help of Dr Gerry Gillen, Dr Dan Wei, Suresh Annavarapu and Professor Roger Doherty during the course of this research, and thank the Office of Naval Research for sponsoring the research project (Contract N 00014-84-K-0472; NR 650-025).

## REFERENCES

1. P. W. Wright, *Mater. Design* **8**, 3, (1987).
2. *Net Shape Technology in Aerospace Structures*, I-IV, National Academy Press, Washington, D.C. (1986).

3. D. Apelian, *Innovations in Materials Processing* (edited by G. A. Bruggeman and V. Weiss). Plenum Press, New York (1983).
4. M. M. Welch, *Precision Metal* **44**, 3 (1986).
5. A. Lawley, *Advanced Manfng Proc.* **1**, 3 & 4 (1986).
6. A. G. Leatham, R. G. Brooks and M. Yaman, *Modern Developments in Powder Metallurgy*, (edited by E. N. Aqua and C. I. Whitman), Vol. 15. Metal Powder Ind. Fedn. Princeton, N.J. (1985).
7. A. G. Gillen, P. C. Mathur, D. Apelian and A. Lawley, *Progress in Powder Metallurgy* (edited by E. A. Carlson and G. Gaines), Vol. 42. Metal Powder Ind. Fedn. Princeton, N.J. (1986).
8. M. R. Jackson, J. R. Rairden, J. S. Smith and R. W. Smith, *J. Metals* **33**, 11 (1981).
9. A. A. Ranger and J. A. Nicholls, *A.I.A.A.J.* **7**, (1969).
10. R. Clift, J. R. Grace and M. E. Weber, *Bubbles, Drops and Particles*. Academic Press, New York (1978).
11. G. Dahlquist, A. Bjorck and N. Anderson, *Numerical Methods*. Prentice Hall, N.J. (1974).
12. W. E. Ranz and W. R. Marshall, *Chem. Engng Prog.* **48**, (1952).
13. I. Kimura and A. Kanzawa, *A.I.A.A.J.* **3**, (1965).
14. P. Haasen, *Physical Metallurgy*. Cambridge Univ. Press (1978).
15. G. P. Ivanotsov, *Growth of Crystals*. Consultants Bureau Inc., New York (1958).
16. J. S. Langer and H. Muller-Krumbhaar, *Acta metall.* **26**, 11 (1978).
17. M. C. Flemings, *Solidification Processing*. McGraw Hill, New York (1974).
18. M. J. Aziz, *J. appl. Phys.* **53**, 1158 (1982).
19. W. J. Boettinger, S. R. Coriell and R. F. Sekerka, *Mater. Sci. Engng* **65**, 1 (1984).
20. A. R. E. Singer and R. W. Evans, *Metals Tech.* **10**, (1983).
21. H. Martin, *Advances in Heat Transfer* (edited by J. P. Harnett and T. F. Irvine), Vol. 13, Academic Press, New York (1977).
22. L. J. D. Sully, *A.F.S. Trans.* **84**, (1976).
23. R. Mehrabian, *Rapid Solidification Processing: Principles and Technologies* (edited by R. Mehrabian *et al.*), Claitor's, Baton Rouge, La (1978).
24. B. P. Bewlay and B. Cantor, *Rapidly Solidified Materials* (edited by P. W. Lee and R. S. Carbonara), p. 97. Am. Soc. Metals, Metals Park, Ohio (1986).
25. Y. Tomota, M. Strum and J. W. Morris, *Metall. Trans.* **17A**, (1986).
26. Y. Tomota, M. Strum and J. W. Morris, *Metall. Trans.* **18A**, (1987).
27. H. Jones, *Rapid Solidification Processing: Principles and Technologies* (edited by R. Mehrabian R. *et al.*). Claitor's, Baton Rouge, La (1978).
28. *Thermophysical Properties of Matter*. TPRC Data Series, Purdue Univ. Plenum Press, New York (1977).
29. R. D. Pehlke *et al. Summary of Thermal Properties for Casting Alloys and Mold Materials*. National Science Found., NSF/MEA-82028 (1982).

## APPENDIX I

### *Nomenclature*

$A$ = droplet cross sectional area
$b$ = radial distribution coefficient; equation (20)
$B$ = maximum deposition rate; equation (20)
$C$ = specific heat
$C_D$ = drag coefficient
$d$ = droplet diameter
$d_0$ = capillary length [16]
$d^*$ = largest solidified droplet
$D$ = solute diffusion coefficient
$\dot{D}$ = deposition rate
DAS = dendrite arm spacing
$E_i$ = integral-exponential function
$f(d_i)$ = fraction of droplets of diameter $d_i$
$f_s$ = fraction solid
$f_s'$ = fraction solid during recalescence
$f$ = dimensionless undercooling = $\Delta T/\Delta T_c$
$F$ = force
$g$ = acceleration due to gravity
$h$ = heat transfer coefficient
$H$ = enthalpy
$\Delta H_f$ = latent heat of fusion
$k$ = Boltzman constant
$K$ = thermal conductivity
$L$ = deposit thickness
$m$ = mass of droplet
$N$ = number of atoms
Nu = Nusselt number = $hd/K$
$N_v$ = nucleation density
$p$ = Peclet number = $V_{dgv} r_{den}/2D$
Pr = Prandtl number = $\upsilon/\alpha$
$Q$ = heat flux
$r$ = radius
$R$ = radial distance from spray axis
Re = Reynolds number = $Vd/\upsilon$
$S$ = droplet surface area
$\dot{S}$ = solidification rate
$t$ = time
$T$ = temperature
$\dot{T}$ = cooling rate
$\Delta T$ = undercooling, change in temperature
$\Delta T_c$ = undercooling for homogeneous nucleation
$\Delta T_f$ = freezing range of alloy
$V$ = velocity
$W$ = width of gas jet at nozzles
$z$ = growth axis, thickness
$\alpha$ = thermal diffusivity
$\beta$ = angle between the spray axis and droplet trajectory
$\epsilon$ = emissivity
$\gamma$ = surface energy
$\lambda$ = distance between gas nozzles and substrate
$\eta$ = dimensionless thickness = $z/L$
$\nu$ = kinematic viscosity of gas
$\Omega$ = thermal supersaturation = $(T_l - T)/\Delta T_c$
$\rho$ = density
$\tau$ = stability parameter = 0.025 [16]
$\sigma$ = Stefan–Boltzman constant
$\phi$ = fraction of heat in the freezing range, equation (19)

*Subscripts*

a = arrest
c = convective
d = droplet
den = dendrite
dgv = dendrite growth velocity
e = eutectic
f = freezing
g = gas
i = initial
l = liquidus
n = nucleation
P = particle
pl = partially liquid
r = relative
re = recalescence
s = substrate
w = walls of the spray chamber

## APPENDIX II

### *Values of Specific Parameters used in the Model*

Physical and thermal properties of Ni–Cr, Fe–Mn and nitrogen gas were taken from [28] and [29]. The values of other parameters are listed below:

$d_i$ = 20–200 μm
$T_g$ initial = 25°C
$T_i - T_l$ = 50°C (superheat)
$T_w$ = 50°C
$V_g$ initial = 320 m/s
$V_d$ initial = 0–10 m/s (no significant effect on velocity profile)
$\beta$ = 0°–7°
$\epsilon$ = 0.4
$T_s$ = 100°C
$T_g$ = 200°C (at substrate)
$h_s = 10^3$ W/m²/K

*Equation (17)*

$\lambda$ = 400 mm
$W$ = 20 mm
$R$ = 2.5*W
Re = 8554

# Process Control, Modeling and Applications of Spray Casting

P. Mathur, S. Annavarapu, D. Apelian and A. Lawley

*Spray casting involves sequential atomization and droplet consolidation at deposition rates above 0.25 kg/s, and at least eight independent process parameters must be optimized to achieve the desired preform shape, microstructure and yield. Because effective utilization of spray casting requires control of the preform shape with metallurgical integrity, there is a compelling need to quantify the influence of process parameters on shape, microstructure and overall yield. Coupling this knowledge base with appropriate sensor and control technology establishes a means for process control.*

## INTRODUCTION

Spray casting via the Osprey™ process is emerging as an attractive technology to produce near-net-shape components of a variety of alloys.[1-4] The process involves the sequential stages of gas atomization and droplet consolidation on a substrate, as shown schematically in Figure 1. The alloy charge is melted in a crucible located on top of the spray chamber and exits through a nozzle in the bottom of the crucible. In the atomizing zone, the stream of molten metal is comminuted into a spray of droplets using nitrogen or argon gas. Droplets are cooled by the gas and accelerated towards the substrate, which is positioned below the atomization zone. The droplets impinge and consolidate on the substrate to form a bulk-net or near-net shape.

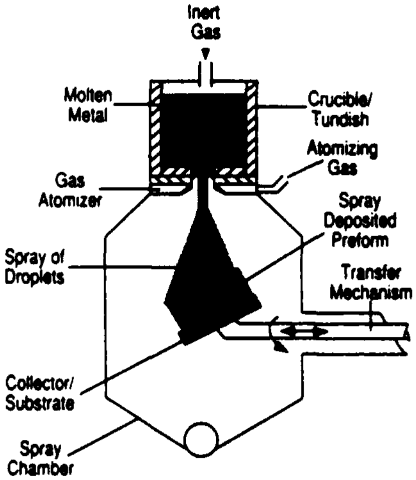
Inert Gas
Molten Metal
Crucible/ Tundish
Atomizing Gas
Gas Atomizer
Spray Deposited Preform
Spray of Droplets
Transfer Mechanism
Collector/ Substrate
Spray Chamber

Figure 1. A schematic diagram of the Osprey™ process.

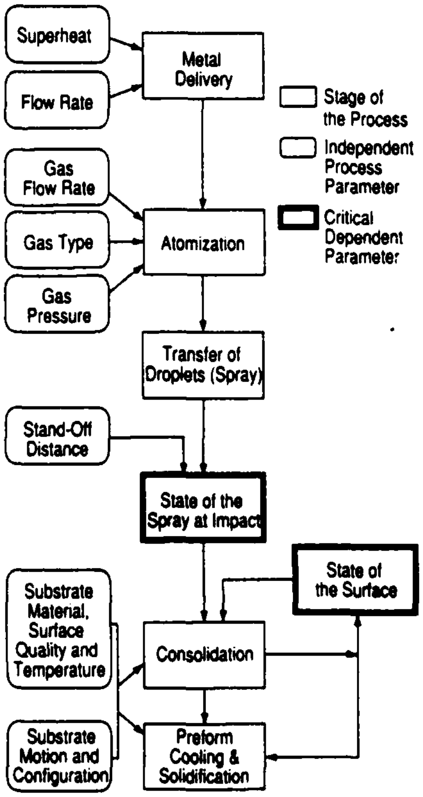
Superheat
Flow Rate
Metal Delivery
Stage of the Process
Independent Process Parameter
Critical Dependent Parameter
Gas Flow Rate
Gas Type
Atomization
Gas Pressure
Transfer of Droplets (Spray)
Stand-Off Distance
State of the Spray at Impact
State of the Surface
Substrate Material, Surface Quality and Temperature
Consolidation
Substrate Motion and Configuration
Preform Cooling & Solidification

Figure 2. Flow chart depicting the independent process parameters at each intermediate stage in spray casting.

A variety of preform shapes can be produced by maneuvering the substrate beneath the spray. Billets or disks of 100–250 mm in diameter are manufactured by spraying onto a rotating disk which is inclined to the spray axis and translated back and forth under the spray. Disk preforms are being evaluated by Osprey Metals Ltd.,[2-7] Alcan (for aluminum-matrix composites),[2,4-7] Howmet and General Electric (for superalloy aerospace applications),[8,9] Alusuisse and Pechiney (for aluminum alloys) and others.[10-14] Spray deposition onto a roller or an endless belt allows strip or sheet to be produced in a semi-continuous fashion.[2,6,15,16] Mannesmann-Demag Hüettentechnik can spray strip from 10–20 mm thick, up to 1 m in width and several meters in length.[2,17] Sandvik Steel is producing stainless steel tubing 100–440 mm diameter up to 8 m in length by spraying onto a rotating, preheated mandrel.[2-4,6,17] Sumitomo Heavy Industries is utilizing the Osprey process in the manufacture of large diameter rolls.[2,6]

The major advantage of spray casting is that a near-net-shape product can be fabricated in a single operation directly from the melt at deposition rates in the range of 0.25–2.5 kg/s. Metallurgically, the product is characterized by a uniform distribution of equiaxed grains (20–200 μm), no macroscopic segregation of alloying elements, a uniform distribution of second phases, low oxide content and the absence of particle boundaries.[2-6,8-15] Spray casting can also be used to produce composite materials by injecting particulates into the spray of molten droplets,[2,4-6] or dispersion-strengthened alloys by selective chemical reaction of the droplets during flight.[18]

Successful operation of the Osprey process mandates a knowledge of the effect of each process parameter on preform shape, microstructure, properties and yield. This knowledge base, coupled with appropriate sensor and control technology, provides a means to optimize and control spray casting.

## PROCESS CONTROL

At least eight independent process parameters (IPPs) must be optimized in the Osprey process. These IPPs, and their regimes of influence, are shown in Figure 2. Each of the IPPs can be directly controlled during the process and each affects a number of dependent process parameters (Figure 3). The relationship between an IPP and preform quality can be simplified by identifying two critical dependent parameters ($\text{CDP}_1$ and $\text{CDP}_2$) which also are shown in Figure 2. $\text{CDP}_1$, the state of the spray just prior to consolidation, is characterized in terms of the percent liquid in the spray, the fraction and size distribution of solidified vs. liquid droplets, and the spatial distribution of droplet mass across the spray. $\text{CDP}_2$, the physical and thermal state of the surface onto which the droplets impact, includes the fraction of solid and the surface roughness of the deposit.

Optimal values of the two dependent parameters must be established in order to maintain conditions of incremental solidification,[3,4,19] such that the thickness and fraction of solid in the partially liquid layer on the surface of the deposit are kept constant during the deposition process. For example, if the spray (and/or the top surface of the deposit) contains a high volume fraction of solid ($f_s \rightarrow 1$), a majority of the droplets will be solidified and no coherent deposit will be formed; the process then resembles powder production. On the other hand, spray casting is analogous to conventional casting if the spray/deposit contains a high fraction of liquid ($f_s \rightarrow 0$). The "ideal" amount of liquid lies between these extremes, and the liquid must flow and fill the interstices between presolidified droplets. The impinging droplets must also "stick" to the surface of the growing deposit and maximize deposit yield.

Two types of process models may be employed to describe spray casting. In high-resolution models, the effect of each parameter (independent and/or dependent) on other dependent parameters is accounted for by applying fundamental scientific theories at each stage of the process. Accuracy of the results depends upon the degree of detail with which the physical and thermal phenomena are described. In contrast, low-resolution models employ statistical averages of the high-resolution data, empirical rules and sets of logical and/or descriptive statements to formulate the causal relationships between process parameters and preform quality. In this way, it is possible to neglect a large number of the dependent parameters and to simplify these relationships.

## PREFORM SHAPE

The shape of the preform is determined by the spatial distribution of droplet mass in the spray, the sticking efficiency of the droplets on arrival at the substrate, and the motion of the substrate and/or the spray.

The flux of droplets (i.e., the deposition profile) is a maximum at the axis of the spray and decreases towards its periphery; the growth rate of the deposit ($\dot{Z} = dZ/dt$) varies in a similar manner. The variation of $\dot{Z}$ with radial distance (r) from the spray axis was found to follow a normal Gaussian curve:[20-22]

$$\dot{Z}(r) = \exp \dot{Z}_0(-\beta r^2) \qquad (1)$$

where $\dot{Z}_0$ is the maximum growth rate (at the spray axis, r = 0) and β is the radial distribution coefficient that governs the spread of the spray. For the Osprey atomizer, $\dot{Z}_0$ and β were determined as ~5.25 mm/s and 0.0005 mm$^{-2}$, respectively, at a distance of 400 mm below the gas nozzles.

For the production of billets or disk preforms, it is beneficial to have a narrow, focused spray to increase the yield on the collector area. On the other hand, an elliptical deposition profile is preferred in strip casting to increase strip width and uniformity in strip thickness. This can be achieved by employing a "linear" atomizer wherein the metal delivery nozzle and the surrounding gas jets have a rectangular cross section.[23] It is also possible to tailor the spray to any desired shape/deposition profile by the utilization of tertiary gas jets[24] and/or magnetohydrodynamic forces (MHD).

Only a portion of the droplets in the spray reach the substrate/target; this fraction is defined as the target efficiency of the spray ($\Pi_t$). Furthermore, only a fraction of the droplets arriving at the substrate stick and contribute to deposit growth; the remaining droplets bounce off. The fraction which adheres is termed the sticking efficiency ($\Pi_s$). Deposit yield and deposition rate are determined by the product of these two efficiencies:

$$\%\text{Yield} = (\Pi_t \cdot \Pi_s) \cdot 100 \qquad (2)$$

The target efficiency depends upon the size of the substrate, the shape of the spray, the stand-off distance, the distribution of droplets within the spray and the substrate motion. Similarly, sticking efficiency is governed by the state of the spray at impact ($CDP_1$), the state of the top surface ($CDP_2$), and the substrate configuration and motion.

Since the deposition profile (Equation 1) is predetermined by the design of the atomizer, the substrate and/or the spray must be moved to achieve the desired preform shape. Optimum values of parameters for substrate motion

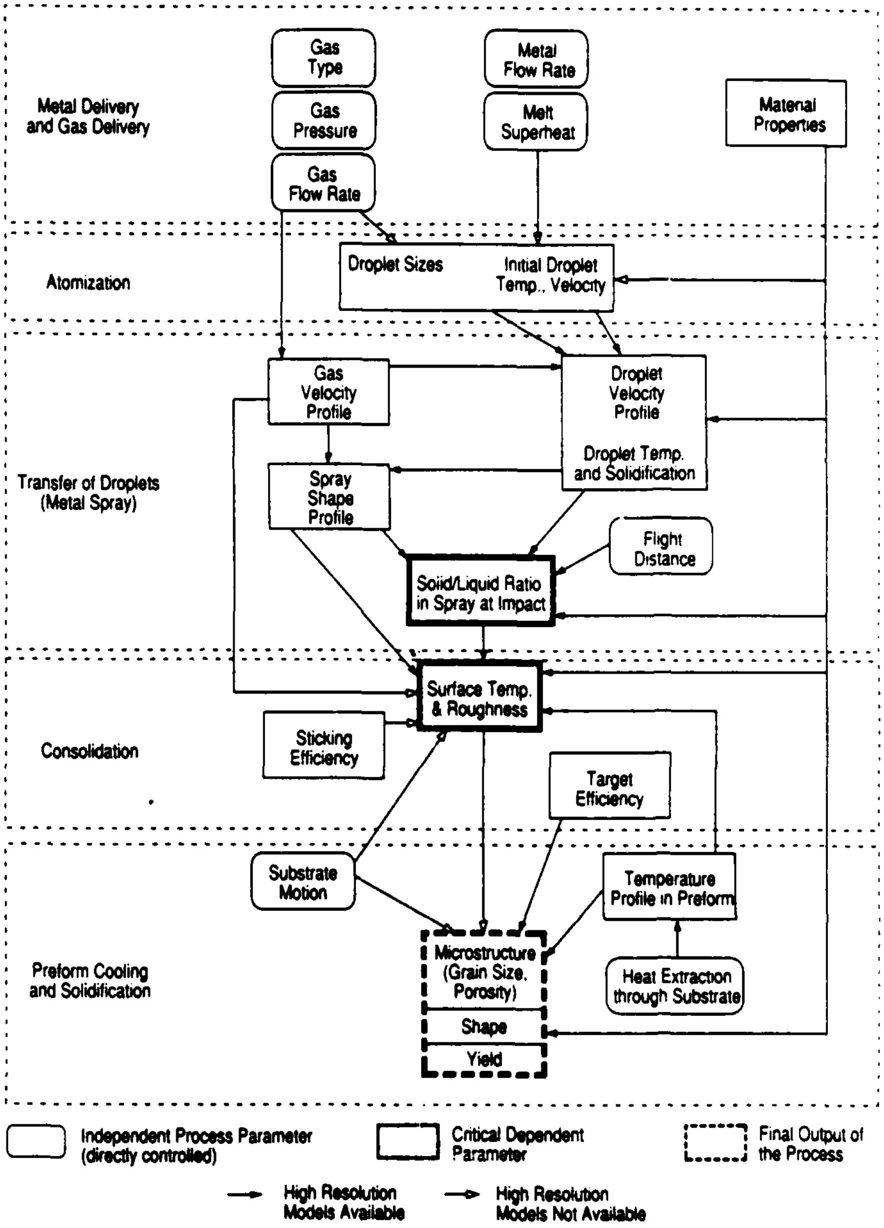
Metal Delivery and Gas Delivery
Gas Type
Gas Pressure
Gas Flow Rate
Metal Flow Rate
Melt Superheat
Material Properties
Atomization
Droplet Sizes
Initial Droplet Temp., Velocity
Transfer of Droplets (Metal Spray)
Gas Velocity Profile
Droplet Velocity Profile
Droplet Temp. and Solidification
Spray Shape Profile
Flight Distance
Solid/Liquid Ratio in Spray at Impact
Consolidation
Surface Temp. & Roughness
Sticking Efficiency
Target Efficiency
Preform Cooling and Solidification
Substrate Motion
Temperature Profile in Preform
Microstructure (Grain Size, Porosity)
Shape
Yield
Heat Extraction through Substrate
Independent Process Parameter (directly controlled)
Critical Dependent Parameter
Final Output of the Process
High Resolution Models Available
High Resolution Models Not Available

Figure 3. Flow chart depicting the interlinking of independent and dependent process parameters at five stages of the process.

(e.g., rotation speed, translation speed, limits of translation, etc.) can be determined *a priori* by a mathematical model in which the state of the spray at consolidation is coupled with a model for substrate motion.[10,21,22] For a given substrate (i.e., a disk collector, a tubular mandrel or a roller), this model selects a location P(x,y) on its surface and computes thickness during deposition. The calculations are then repeated for different locations which are defined by a grid on the substrate surface. The magnitude of the increment of thickness ($\Delta Z$) during each time step at any substrate location P(x,y) is governed by the radial distance (r) between P(x,y) and the axis of the spray (Equation 1). If the substrate is stationary, the value of r is constant during the entire deposition cycle. If the substrate is non-stationary, r changes with time depending upon the motion imparted, (i.e., on the locus of P with respect to the spray axis). Models to predict preform shape are now utilized for spray-cast disks, tubes, billets and/or strip.[22,25-27]

## PREFORM MICROSTRUCTURE

Grain size is a primary index of microstructure in spray-cast material. Prior research[20,21] suggests that grain size and segregate spacing in spray-cast preforms are determined by the condition of the spray at impact, the spatial distribution of solid particles after impact, and the time required for complete solidification of the preform. In addition, the level and distribution of porosity is a sensitive measure of processing conditions.

### Condition of Spray at Impact

The state of the spray is described by the velocity and extent of solidification of droplets prior to impact. Due to the microscopic size of the droplets and the time scale of events occurring during droplet flight, mathematical modeling has been employed to predict the variation of droplet velocity, temperature and extent of solidification with flight distance.[20-22,26,28,29] Sample results of the models[20-22,28] are provided in Figure 4. Droplet velocities at consolidation are predicted to be in the range of 10–100 m/s, depending primarily upon droplet mass. Limited experimental measurements[21,30,31] have shown that the predicted velocity profiles are correct, at least within an order of magnitude. With the current state of the art, however, it is not possible to precisely measure the velocity of a single droplet since both velocity and diameter of the droplet must be measured simultaneously along the flight trajectory.

Droplets cool during flight by losing heat to the surrounding gas via forced convection and radiation. The predicted extent of solidification of droplets at a flight distance of 400 mm is plotted in Figure 4a for droplets of Al, Al-4.5Cu, Cu, Ni and Fe. The juxtaposition of the curves indicates that alloys with high melting points (e.g., iron) solidify faster than those with low melting points (e.g., Al-4.5Cu) due to a greater difference in temperature between the metal and atomizing gas.

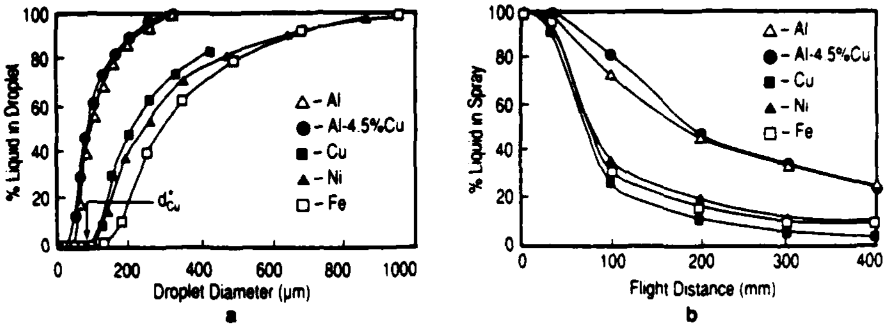

Figure 4. (a) Extent of droplet solidification vs. diameter for five alloys, using nitrogen gas for atomization. (b) Predicted variation of the percentage of liquid in the spray with flight distance showing effect of material properties, using nitrogen gas for atomization.

From the figure, the condition of droplets arriving at the deposition surface ($CDP_1$) can be characterized. Droplets of a diameter less than the critical value d* are completely solidified upon impact [the percent liquid in the droplet ($\%L_d$) = 0]. Typically, d* is predicted to be in the size range of 30–125 μm, and it increases with the increasing melting point of the alloy. This corresponds to a large fraction of presolidified droplets due to the bimodal population distribution.[20] Droplets with diameters greater than d* impact the deposition surface in a "mushy" condition with varying fraction of liquid. These droplets comprise a solidified dendritic skeleton, as observed from interception of droplets in flight on glass slides.[21] Droplets greater than about 300 μm in diameter for aluminum and 900 μm in diameter for the other metals arrive at the deposition surface in a completely liquid state.

In low-resolution models, it is advantageous to combine the condition of individual droplets and, at the expense of resolution, derive average values which represent the state of the spray at a macroscopic level. For example:

$$\%L_{spray}(X) = \sum_{i=1}^{n} [1 - f_s(d_i, X)] \cdot P(d_i) \cdot 100 \quad (3)$$

where $\%L_{spray}$ is the percentage of liquid in the spray at flight distance X, $f_s$ is the fraction solid in a droplet of diameter $d_i$, and $P(d_i)$ is the weight fraction of droplets in the size range $d_i$ to $d_{i+1}$. The predicted variation of $\%L_{spray}$ with X is plotted in Figure 4b for the five alloys under a fixed set of parameters in order to compare the effect of material properties. The shallow slope of the curves in the initial stage of flight ($0 < X < 25$ mm) is due to the release of superheat and to undercooling of the droplets prior to solidification. Thereafter, the solidification rate reaches a maximum beyond a distance of about 50 mm, then decreases monotonically with flight distance. Of the material parameters, the melting point ($T_m$) and the value of $H_{FR}$ [$H_{FR}$ = heat in the freezing range of the alloy = latent heat ($H_f$) + specific heat ($C_p \Delta T_f$)] have the most significant effect on the thermal condition of the spray. This is evidenced by copper, which solidifies most rapidly since it has the smallest value of $H_{FR}$ (Figure 4b). Aluminum and Al-4.5Cu possess high values of $H_{FR}$ and a low $T_m$, and solidification is significantly slower than in the other materials.

During deposit build up, the effective spray height decreases with time and this results in a corresponding increase in the enthalpy or amount of liquid carried into the deposit (Figure 4b). Therefore, to maintain uniformity in deposition conditions, it is necessary to continuously increase the distance between the substrate and the point of atomization (at a rate of $\dot{Z}$) to maintain a constant spray height at the deposition surface.

### Spatial Distribution

The spatial distribution of solid particles after impingement is strongly dependent upon their spatial distribution in the spray prior to impact, and upon secondary effects such as droplet fragmentation and bounce off. While quantitative data on these phenomena are currently lacking, glass slide experiments have provided evidence that the mode of deformation of the droplets upon impact depends primarily upon the extent of their solidification.[21] Small, fully solidified droplets undergo minimal deformation upon impact and have a spherical morphology with smooth surfaces. Larger droplets which are only partially solidified fragment along interdendritic regions, while droplets which are fully liquid spread radially and splat[32] on the glass collector plate.

### Preform Solidification and Cooling

In order to effect complete solidification, a total amount of heat, $H_S (H_S = C_p \Delta T_s + H_{FR})$ must be removed from the metal, where $C_p$ is the specific heat, $\Delta T_s$ is the melt superheat at atomization and $H_{FR}$ is the heat contained in the freezing range of the alloy (Figure 5). The amount of heat which must be removed *after* deposition in order to complete the solidification is given by $H_{rem}$:

$$H_{rem}(X) = (C_p \Delta T_s + H_{FR}) - H_{gas}(X) \qquad (4)$$

where X is flight distance and $H_{gas}$ represents the amount of heat removed by the gas during flight (Figure 5).

*Continuum Models*

Two approaches have been adopted to calculate the solidification time ($t_f$) required to remove $H_{rem}$ from the preform. In the continuum model approach,[20–22,26,33] $t_f$ is computed by a macroscopic energy balance between the heat influx from the spray ($H_{rem}$), the mass influx (Z), the heat extracted by the substrate ($Q_s$), and the heat extracted by the atomizing gas ($Q_g$). This is shown schematically in Figure 6a. A moving boundary transient heat conduction equation is solved numerically to obtain the enthalpy, temperature and fraction of solid within the volume elements as a function of time.[20–22] Measured values of the heat transfer coefficient at the deposit substrate interface are at their maximum of ~$10^5$ W/(m²·K) at the start of deposition and decrease to ~500 W/(m²·K) within a few seconds.[21] This decrease is attributed to the formation of an "air gap" between the deposit and the substrate due to contractional stresses upon solidification. Similarly, the heat transfer coefficient for the gas cooling at the top surface of the deposit is estimated to be about 200 W/(m²·K).

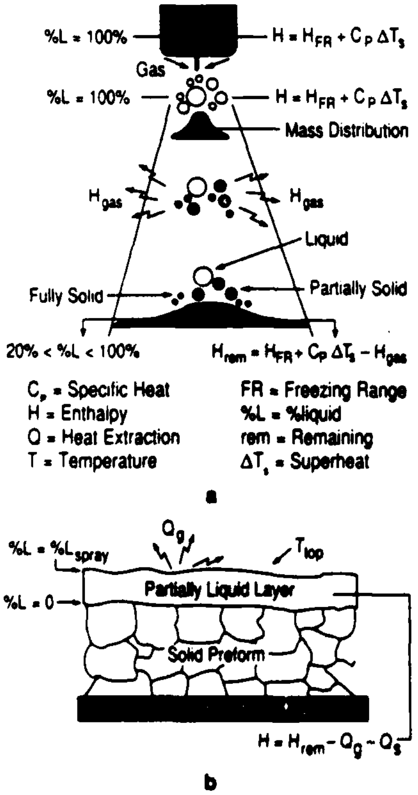

Figure 5. Schematic representation of spray casting showing the physical and thermal states of (a) the spray and (b) the deposit.

Sample predictions of the continuum model are shown in Figure 7 for the spray deposition of an Al-4.5Cu disk. Deposition was carried out using a water-cooled, circular substrate which was simultaneously rotated and translated under the spray to achieve a cylindrical preform. The "deposition line" in Figure 7a is the predicted growth of thickness at the center of the circular substrate. This variation of thickness with time depends upon the locus of the disk under the spray and was derived from the model to predict preform shape. The disk grows to a height of ~70 mm during 40 s of deposition and remains at a constant height thereafter.

The isothermal lines in Figure 7a provide the variation of temperature and volume fraction of solid ($f_s$) in the disk along its height as a function of time. During deposition (i.e., the first 40 s), the top surface of the disk is hotter and contains a smaller fraction of solid than the bottom due to the influx of heat and mass from the spray. Once deposition is completed, the top surface begins to cool and solidify rapidly due to gas cooling at the top surface, and the last liquid to freeze is at a height of ~45 mm above the substrate surface. The interval between the deposition line and the $f_s = 1$ contour is a measure of the local solidification time ($t_f$). The bulk of the disk preform solidifies over a period of 70–100s and cools at more than 20°C/s. Thus, the solidification process in spray casting occurs in two stages: a majority of the solidification occurs in flight under conditions of rapid solidification and the fraction of the liquid (10–40%) which is carried into the deposit undergoes relatively slow cooling. Therefore it is desirable to maximize heat removal during flight to the extent that the amount of liquid carried into the deposit is just sufficient to consolidate the presolidified droplets. The partially liquid layer ($f_s$ < 1.0) on the surface of the preform is considered beneficial to the microstructure of the spray-cast preform, because the resultant increase in local solidification time allows fluid to flow into the interstices between presolidified droplets. However, the thickness of the layer must be controlled to maintain conditions of incremental solidification.[19]

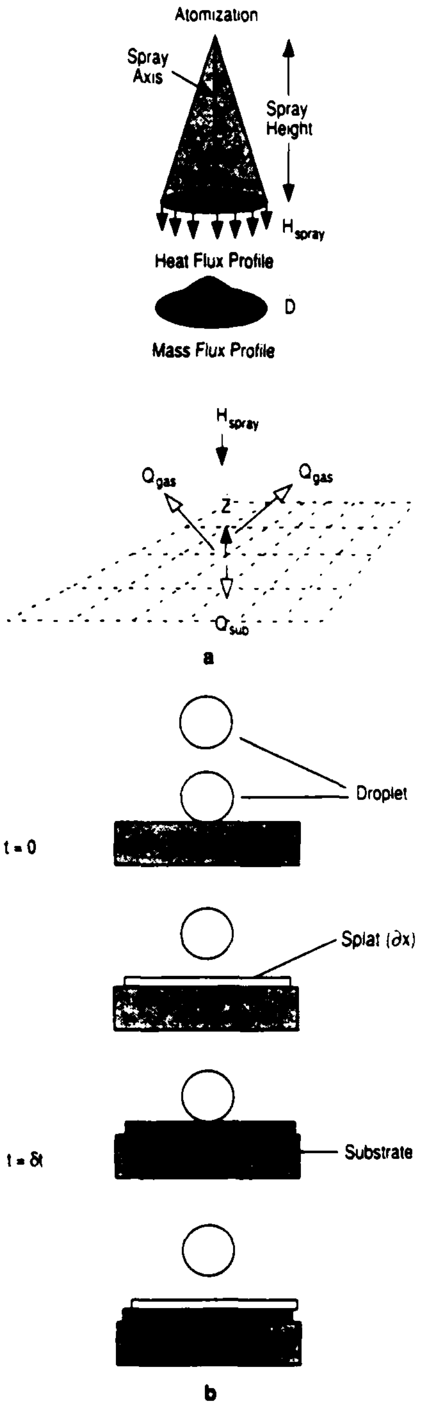

Figure 6. Schematic diagrams showing the (a) continuum and (b) discrete-event approaches to the modeling of preform growth and solidification.

Grain size and segregate spacing in the preform are larger than those in atomized powder but smaller than the values based on empirical correlations of dendrite arm spacing and cooling rates predicted by the continuum model:[20,34–36]

$$d = d_0 \exp(t_f)^m = d_1 \exp(\dot{T})^n \quad (5)$$

where coefficients $d_0$ and $d_1$, and the exponents m and n, are dependent on the material. Although the predicted

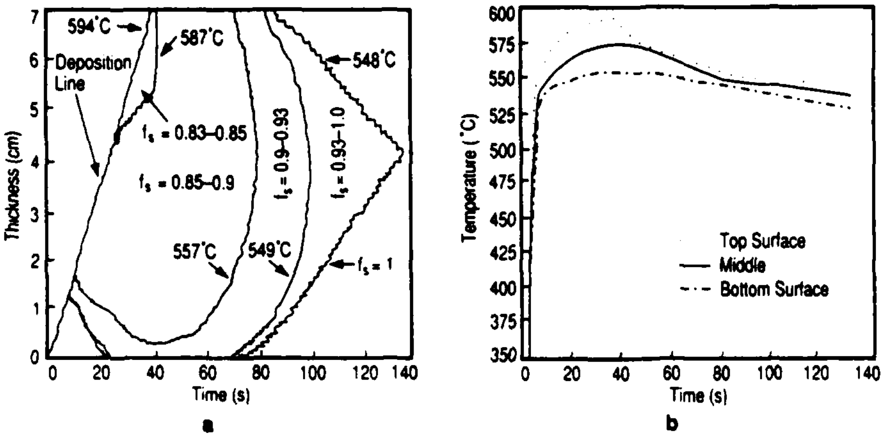

Figure 7. Predictions of the continuum model for an Al-4.5Cu disk, 120 mm in diameter. The substrate, rotating at 200 rpm, was water-cooled to maintain a temperature of 25°C, and the spray temperature was 600°C. The translation speed was 20 mm/s; deposition lasted 40 s. (a) Thermal profiles in a disk preform. (b) Variation of temperature at the top, middle and bottom locations in the disk during spray deposition.

grain size follows the same trend as the experimental data,[20,33,36] it is higher in magnitude by a factor >2. This overestimate of the grain size and/or segregate spacing from such equations may be due to the two-stage solidification process in spray casting, retarded coarsening of the dendrite arms at a high volume fraction of solid,[37] and nucleation by presolidified droplets from the spray. Thus, from a knowledge of temperature alone it is not possible to predict the grain size in the preform.

### *Discrete-Event Models*

The non-continuum modeling approach to preform solidification is a more recent development.[25,36] Unlike the continuum models, the non-continuum, discrete-event models assume deposit growth occurs in discrete steps by the addition of splats (Figure 6b). Individual droplets impact on the preexisting surface and spread to form a splat in microseconds.[32,37,38] The splat then cools and solidifies via conduction through the bottom surface and convection at the top surface. This continues until the next droplet arrives after a time interval $\delta t$ between successive impacts. Drawbacks of the discrete-event model are that it is computationally intensive and that there is uncertainty in the values of input parameters (e.g., splat thickness and interval between splats).

A direct comparison of the predictions of the two formulations (discrete-event and continuum) for the top surface temperature under identical conditions is shown in Figure 8. Both models predict the formation of a partially liquid layer after a short time interval of the same order, and the predictions appear to converge within about 0.5 s. Implications are that the predictions of the continuum approach are reasonable and valid after a time corresponding to the formation of the partially liquid layer.

### Degree of Porosity

The predicted values of $\%L_{spray}$ upon deposition are in the range of 10–40%. This suggests that only a small fraction of liquid is required to consolidate the presolidified droplets during deposition, and that the mechanism of droplet consolidation in spray deposition resembles liquid-phase sintering.[39,40] Therefore, the level of porosity in the preforms is determined primarily by a balance between the solid/liquid ratio being deposited and by the packing efficiency of the solid particles.

The effect of physical and thermal properties of the substrate on preform characteristics is a strong function of the degree of contact between the two. If the surface is smooth and the degree of contact is poor, the thermal properties of the substrate have minimal effect on preform solidification. Metallic substrates (e.g., copper or steel) produce a high rate of heat extraction in the initial stages of deposition due to good thermal contact; this results in the formation of a pronounced initial chill layer approximately 1 mm thick, with attendant porosity of roughly 10–15%. Heat extraction decreases after 1–2 s due to the formation of an air gap between the deposit and the substrate. A refractory substrate decreases the level of basal porosity due to its lower thermal conductivity. The heat transfer coefficient at the interface may be controlled by coating the substrate surface with a non-conductive material (e.g., boron nitride). The heat flux into the substrate can be decreased by preheating the substrate; this approach is being utilized in the manufacture of strip and tube.

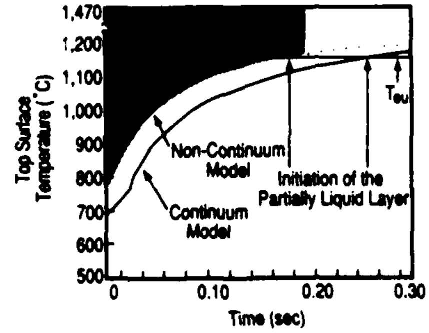

Figure 8. Comparison of continuum and discrete-event model predictions under identical processing conditions for plain carbon steel. Deposit surface temperature is plotted as a function of time. $T_{eu}$ is the eutectic temperature, and the spray temperature was 1,470°C.

## APPLICATIONS

### Strip Casting

The trend in steelmaking is to move away from a capital-intensive structure towards flexible manufacturing processes to obtain higher added value. Droplet consolidation processes are unique since, in principle, they eliminate casting as an independent step in the process. Savings via spray casting fall between the extremes of thin slab and strip casting and are $30–40 per tonne because of the elimination, in part, of the hot rolling step. In addition, the manufacture of thin sections of laminates and of particulate-reinforced strip is possible.

Initial studies[41–43] were based on the pioneering spray rolling efforts at the University of Swansea by Leatham and Singer on Al-Zn, copper and steel alloys with a rudimentary spray forming unit. At Drexel University, the effects of processing parameters on the structure and integrity of spray-cast steel strip are being investigated.[15,16,25] For a standard atomizer geometry, the strip exhibits non-uniformity in transverse thickness because of the Gaussian mass flux within the spray. The as-spray-cast steel strip exhibits equiaxed grains with an average size of 100–200 µm; the primary reason for the coarseness of the as-cast structure is the absence of second phase particles to curtail grain growth and coarsening during solidification. Hot consolidation (at small reductions) and concurrent recrystallization yield a refined, equiaxed, ferrite-pearlite structure.[23] Compared to the dendritic structures obtained via thin-slab and thin-strip casting, the microstructure of the spray-cast strip is decidedly superior.

Under license, Mannesmann Demag is working on a commercial-scale pilot plant study of steel strip. The restriction on strip width with standard atomizers, and the limitation of non-uniformity of strip thickness, have been overcome via development and implementation of a "scanning" atomizer (Figure 9). In a parallel development,

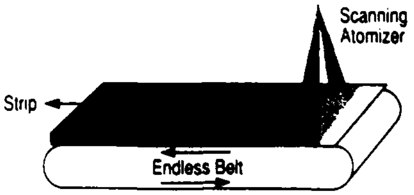

Figure 9. Schematic diagram of a scanning atomizer developed to cast strip steel.

Singer assessed spray rolling for the manufacture of steel strip and a company has been set up to investigate this approach.[44] Notable among others involved in the development of this technology is NKK Corporation, which is investigating spray rolling using tertiary gas jets to obtain a uniform mass flux profile.[24] Olin[45] recently acquired a license from Osprey Metals to manufacture copper strip.

The principal obstacles to commercialization of the spray casting route are the inferior quality of the top surface of the strip, the occurrence of surface-connected basal porosity and the low yields derived from overspray and low casting rates. The substrate must be preheated to >700°C in order to significantly reduce the amount of basal porosity in steel strip. Presently, it is necessary to hot roll the strip about 40% to achieve full density; this may be minimized by on-line control of the process parameters.

### Disk, Billet and Tube Manufacture

Disks and billets produced via the Osprey process can be subsequently forged or extruded to the final shape. The uniform distribution of fine grains in the preforms, the absence of macrosegregation and the minimal porosity (<1%) enhance hot workability. Several companies in North America, Europe and Japan are investigating the feasibility of using the process to manufacture superalloy disks for aircraft applications and ceramic-particulate-reinforced aluminum-alloy composites for the automotive industry. There is also interest from the producers of high-grade raw materials to utilize the process in the production of large diameter (>300 mm) billets longer than 1 m. Due to limitations on the diameter of the spray, it may be necessary to simultaneously spray via multiple nozzles to achieve the desired billet diameter and production rates.

In order to control the shape and integrity of the disk, it is necessary to coordinate substrate motion with the shape and mass distribution in the spray. Small imbalances in these parameters result in non-uniform edges, and hot tearing may be encountered at the center of the disk if the parameters of translation are improperly set relative to the spray. There is often a bottom layer (~1 mm thick) comprising a high degree of interconnected porosity (10–15%) which must be removed prior to subsequent operations.

### Composites

Composite materials can be manufactured via spray deposition either by injecting second phase particulates into the spray of metal,[2,4,6,10] or by selectively reacting the droplets during flight using appropriate gaseous media.[18] Alcan and Osprey Metals are producing aluminum-based composite materials reinforced with injected SiC particulates (10–50 μm).

Oxide dispersion strengthened near-net-shape composites can be produced by spray casting. The process offers in-situ, continuous control over alloy composition via chemical reaction between the gas and metal droplets during flight. Examples are the carburization of steel by methane, and the formation of in-situ dispersoids such as $Al_2O_3$, $ThO_2$ or $Y_2O_3$. The mechanism of oxidation of a droplet in flight is divided into five steps: mass transfer in the gas phase, chemical reaction at the gas/oxide interface, mass transfer through the oxide film, dissolution of the oxide at the oxide/metal interface, and mass transfer in the metal. Predictions suggest that oxidation in ferrous alloys may be limited by mass transfer in the gas phase and/or chemical reaction at the gas/oxide interface.[18]

## ACKNOWLEDGMENTS

*The authors acknowledge support of the work on spray casting from the Office of Naval Research (contract 00014-84 K-0472) and the National Science Foundation (grant no. MSM-8519047)*

## ABOUT THE AUTHORS

**Pravin Mathur** received his Ph.D. in materials engineering from Drexel University in 1988. He is currently a research assistant professor at Drexel University. Dr. Mathur is also a member of TMS.

**Suresh Annavarapu** received his Ph.D. in materials engineering from Drexel University in 1989. He is currently a research associate at Drexel University.

**Diran Apelian** received his Sc.D. in metallurgy and materials science from Massachusetts Institute of Technology in 1972. He is currently Howmet Professor of Materials Engineering at Drexel University. Dr. Apelian is also a member of TMS.

**Alan Lawley** received his Ph.D. in metallurgy from the University of Birmingham, England, in 1958. He is currently a professor of materials engineering at Drexel University. Dr. Lawley is also a member of TMS.

**If you want more information on this subject, please circle reader service card number 54.**

### References

1 Osprey Metals Ltd., U.K. patent no. 147239
2 A.G. Leatham, W. Reichelt and O.H. Metelmann, in *Near Net Shape Manufacturing Processes*, ed. P.W. Lee and B.L. Ferguson (Metals Park, OH: ASM, 1988), p. 259.
3 R.W. Evans, A.G. Leatham and R.G. Brooks, in *Powder Metallurgy*, vol. 28, 1 (1985), p. 13.
4 D. Apelian, G. Gillen and A.G. Leatham, in *Processing of Structural Metals by Rapid Solidification*, ed. F.H. Froes and S.J. Savage (Metals Park, OH: ASM, 1987), p. 107.
5 D. Apelian, B.H. Kear and H.W. Schadler, in *Rapidly Solidified Crystalline Alloys*, ed. S.K. Das, B.H. Kear and C.M. Adam (Warrendale, PA: TMS, 1985), p. 93.
6 A.G. Leatham, A.J.W. Ogilvy, P.F. Chesney and O.H. Metelmann, in *Modern Developments in Powder Metallurgy*, vol. 19, compiled by P.U. Gummeson and D.A. Gustafson (Princeton, NJ: MPIF, 1988), p. 475.
7 Osprey Metals Ltd., private communication, R.G. Brooks (1988)
8 R.H. Bricknell, *Metall. Trans.*, 17A (4) (1986), p. 583.
9 H.C. Fiedler, T.F. Sawyer and T.F. Kopp, "Spray Forming—An Evaluation Using IN718," General Electric Technical Information Series, 86CRD113, May (1986).
10 D. Apelian, A. Lawley, P. Mathur and X. Luo, op. cit. 6, p. 397
11 A. Moran and W.A. Palko, in *Progress in Powder Metallurgy*, vol. 43, ed. C.L. Freeby and H. Hjort (Princeton, NJ: MPIF, 1987), p. 43.
12 R.P. Singh and A. Lawley, op. cit. 6, p. 489
13 J. Duszczyk et al., op. cit. 6, p. 441.
14 J.F. Faure and L. Ackermann, op. cit. 6, p. 425
15 S. Annavarapu, A. Lawley and D. Apelian, *Metall Trans*, 19A (12) (1988), p. 3077
16 A. Lawley and D. Apelian, "A Fundamental Study of Thin Strip Casting of Plain Carbon Steel by Spray Deposition," NSF Report MSM-8519047 (Washington, D.C.: NSF, 1988).
17. Mannesmann Demag, W. Germany, private communication, W. Reichelt (1989).
18. Y. Unigame, "An Analysis of Oxide Dispersion Strengthening of Ferrous Alloys during Spray Casting," M.S. thesis, Drexel University (1989).
19. A.R.E. Singer and R.W. Evans, *Met. Tech.*, 10 (1983), p.61.
20. P. Mathur, D. Apelian and A. Lawley, *Acta Metall.*, 37 (2) (1989), p. 429.
21. P.C. Mathur, "Analysis of the Spray Deposition Process," Ph.D. thesis, Drexel University (1988).
22. P. Mathur, D. Wei and D. Apelian, in *Modeling and Control of Casting and Welding Processes IV*, ed. A.F. Giamei and G.G. Abbaschian (Warrendale, PA: TMS, 1988), p. 275.
23. N.J. Grant, in *Casting of Near Net Shape Products*, ed. Y. Sahai, J.E. Battles, R.S. Carbonara and C.E. Mobley (Warrendale, PA: TMS, 1988), p. 203.
24. NKK Corp., Kawasaki 210, Japan, private communication, S. Tomita (1989).
25. S. Annavarapu, "Spray Casting of Steel Strip: Modeling and Experimental Studies," Ph.D. thesis, Drexel University (1989).
26. L.H. Kallien, P.N. Hansen and P.R. Sahm, op. cit. 22, p. 543.
27. Drexel University, Spray Casting Laboratory, current research (1989).
28. J. Liu et al., *Mat. Sci. Eng.*, 98 (1988), p. 43.
29. E.J. Lavernia, E.M. Gutierrez, J. Szekely and N.J. Grant, op. cit. 11, p. 683.
30. B. Bewley and B. Cantor, op. cit. 22, p. 931
31. K. Bauckhage et al., "Simultaneous Size and Velocity Measurements in Multiphase Flow Systems/Some Extentions of the Phase Doppler Method," Proc. 3rd Intl. Symp on Laser Anemometry, ASME Winter Mtg., Boston, Massachusetts (1987).
32. E. Garrity, "A Phenomenological Investigation of Droplet Spreading in Spray Deposition Processes," Ph.D. thesis, Drexel University (1989).
33. H. Jones, in *Rapid Solidification Processing: Principles and Technologies*, ed. R. Mehrabian, B.H. Kear and M. Cohen (Baton Rouge, LA: Claitor's Publishers, 1978).
34. M.C. Flemings, in *Solidification Processing*, (New York: McGraw Hill, 1974).
35. E. Gutierrez-Miraveta, G.M. Trapaga and J. Szekely, op. cit. 23, p. 133.
36. R.D. Doherty, *Met. Sci.*, 6 (1982), p. 1
37. H. Jones, in *Rapid Solidification of Metals and Alloys* (London, U.K.: the Institution of Metallurgy, 1982), p. 43.
38. J. Madjeski, *Int. J. of Heat and Mass Transfer*, 19 (1976), p. 1009.
39. R.M. German, *Liquid Phase Sintering*, (New York: Plenum Press, 1985).
40. P.E. Zovas, R.M. German, K.S. Hwang and C.J. Li, *J. Metals*, 35 (1) (1983), p. 28.
41. A.R.E. Singer, *J. Inst. Metals*, 100 (1972), p. 185
42. A.R.E. Singer, *Metals and Materials*, 4 (1970), p. 246
43. A.R.E. Singer, op. cit. 23, p. 245
44. A.R.E. Singer and N. Jenkins, in *Steelmaking Proceedings*, 69 (1986), p. 877.
45 Olin Corp., Connecticut, private communication, E. Shapiro (1989)

# SPRAY CASTING :
# A REVIEW OF TECHNOLOGICAL AND SCIENTIFIC ASPECTS

---

**Pravin Mathur**† **and Diran Apelian**§
† Research Professor, Department of Materials Engineering
§ Howmet Professor of Materials Engineering; Associate Dean, College of Engineering
**Drexel University, Philadelphia, PA 19104, USA**

**June 1989**

---

**Paper to be published in:**

**Book Series on Powder Metallurgy**
**Volume 3 - Current Status of P/M Technology**

**Editors : I. Jenkins and J. V. Wood**
**Institute of Metals, UK**
**1990**

# SPRAY CASTING :
# A REVIEW OF TECHNOLOGICAL AND SCIENTIFIC ASPECTS

**Pravin Mathur**[†] **and Diran Apelian**[§]
[†] Research Professor, Department of Materials Engineering
[§] Howmet Professor of Materials Engineering; Associate Dean, College of Engineering
Drexel University, Philadelphia, PA 19104, U.S.A

## ABSTRACT

Spray casting (e.g. the Osprey™ process) is emerging as an attractive technology to produce net or near-net-shaped components of a variety of materials. The process involves sequential atomization and droplet consolidation at deposition rates in excess of 0.25kg/s. In this way, it is possible to directly fabricate disks, billets, tubes and strips/sheets by suitable maneuvering of the substrate under the spray of droplets. This paper is a review of technological and scientific aspects governing the shape, microstructure and yield of the preforms produced via spray casting. It addresses phenomena during droplet atomization, transfer of droplets in the spray, droplet consolidation at the substrate, solidification of the consolidated material, and shape/geometry of the preform produced. The knowledge base evolving from this analysis, in conjunction with appropriate sensor and control technology, provides a means to optimize and control the Osprey process.

## 1. INTRODUCTION

In response to increasing global competition, major changes in manufacturing philosophy are taking place within the materials processing industries. The traditional strategy of utilizing high plant capacity and mass production is now being replaced or complemented by flexible manufacturing methods. This new climate has resulted in a strong interest in net- or near-net shape manufacturing (NNSM) processes which are materials and energy efficient. Experts predict that NNSM practices will increase yields, improve efficiency, enhance product quality and generate higher profits [1-3]. The primary incentive is cost reduction, achieved by circumventing intermediate steps in the production process.

Spray casting is emerging as an attractive technology to produce net or near-net-shaped components of a variety of alloys. In principle, spray casting consists of sequential atomization and droplet consolidation. Currently there are two approaches to spray casting: the Osprey™ Process [**4-6**] and Liquid Dynamic Compaction (LDC) [**7-9**]. The primary difference between the two processes is in the mode of atomization; LDC utilizes high velocity pulsed gas jets from an ultrasonic gas atomizer (USGA), while the Osprey process uses a patented gas atomizer of conventional design. Low pressure plasma spraying/deposition (LPPD) [**10**] is another technique of droplet consolidation, wherein the starting material is in the form of solid powder particles. Upon injection into the hot plasma, the particles melt and impact a substrate to form a deposit. The rate of metal deposition in LPPD (0.2-0.5 kg/min. in R. F. plasma and 0.5-1.0 kg/min. in D.C. plasma) is significantly lower than in spray casting processes (10-150 kg/min).

### 1.1 The Osprey™ Process

Since the pioneering work of Singer in the early '70s on spray casting [**11-13**], the first (and only) viable process for bulk fabrication of spray cast preforms was developed by Osprey Metals Ltd. [**4-6,14,15**]. Initial efforts were targeted towards the production of preforms suitable for subsequent hot forging into finished shapes. Today, the Osprey process is being investigated to fabricate disks, billets, tubes and strips/sheets on a commercial scale.

The Osprey spray casting process is shown schematically in Fig. 1. Specific designs of the Osprey unit may vary depending on the size and geometry of preform being fabricated, however, the essential components of any Osprey unit include: (i) a melting and dispensing unit, (ii) a gas atomizer, (iii) a spray chamber, (iv) a substrate mechanism, (v) control panels for the atomization and substrate motion, and (vi) a gas distribution system [**4,5,15**]. Typically, the alloy charge is melted in a crucible located on top of the spray chamber, Fig. 1. During melting, the chamber is purged with inert gas and an over pressure of gas is also fed into the sealed crucible to prevent oxidation of the melt. When molten, the alloy exits through a refractory nozzle in the bottom of the crucible at a superheat in the range 50-150°C. In the atomizing zone below the crucible, the stream of molten metal is comminuted into a spray of droplets by the atomizing gas; either nitrogen or argon is used for atomization at a pressure of 0.6 to 1.0 MPa. In the metal spray, the droplets are cooled by the atomizing gas and accelerated towards the substrate (collector) which is positioned at a suitable distance ($\geq$ 400mm) below the atomization zone. The droplets impinge and consolidate on the substrate to form a near-net shaped preform.

A variety of preform shapes can be produced by appropriate maneuvering of the substrate beneath the spray [4,5,15], Fig. 1. For example, Sandvik Steel in Sweden is producing stainless steel tubing of 100-440mm dia. and up to 8m in length by spraying onto a rotating, preheated mandrel [15,16]. Similarly, Sumitomo Heavy Industries in Japan is utilizing the Osprey process to manufacture large diameter rolls. Billets/disks of 100-250mm dia. are produced by spraying onto a rotating disk collector which is inclined to the spray axis and translated back and forth under the spray. Disk preforms are being evaluated by Osprey Metals Ltd. [4-6,14,15], by Alcan, Pechiney and Alusuisse for aluminum alloys [15,16], and by Howmet and General Electric Corporation for Ni-base superalloys [17,18]. Spray deposition onto a roller and/or an endless belt allows strip to be produced in a semi-continuous fashion [19,20,4]. A majority of the current production and development of strip and sheet products is being conducted by Mannesmann-Demag Hüettentechnik who have spray deposited strip in the thickness range 10-20mm, up to 1m in width and several meters in length [4,15,21]. Numerous other investigations have assessed the viability of spray casting as an alternative to currently employed material processing routes; however only a limited number of results have been published [22-26].

The major advantage of spray casting is that a fine grained, near-net shaped product can be fabricated in a single operation directly from the melt at deposition rates in the range 0.25-2.5 kg/s. Metallurgically, the product is characterized by a uniform distribution of fine, equiaxed grains ($20\mu m$-$200\mu m$), no macroscopic segregation of alloying elements, uniform distribution of second phases, low oxide content and the absence of particle boundaries [4-6,14-18,22-26]. The preforms can be thermo-mechanically treated and their mechanical properties are isotropic and at least comparable to products of conventional processes. Spray casting can also be used to fabricate composite materials by injecting particulates into the spray of molten droplets [4,6,14-16], or to fabricate dispersion-strengthened alloys by selectively reacting the droplets during flight [27].

## 2. TECHNOLOGICAL ASPECTS

Despite the apparent attractiveness of spray casting as a NNSM process, the materials processing industry has been slow to implement it on a commercial scale. Economic viability dictates that the process will compete in the manufacture of high technology materials where the components must not only have the final shape needed, but they must also meet stringent property requirements. Reproducibility and reliability of the final component mandates adequate knowledge of the effect of each process parameter on the shape, microstructure and yield of the preform produced. To date, these variables have been optimized on the basis of trial and error from which empirical relationships have been derived; this approach is labor and/or cost intensive and must be repeated for different materials being sprayed.

At least eight *independent process parameters* (IPPs) must be optimized under the current mode of operation of the Osprey process to achieve the desired preform shape with accompanying metallurgical integrity. These IPPs, and their regimes of influence in the Osprey process, are shown in Fig. 2. The relationship between any IPP and resultant preform quality can be simplified by identifying two *critical dependent parameters* (CDPs) which are shown schematically in Figs. 2 and 3 :

$CDP_1$ : The state of the spray just prior to consolidation. It is characterized in terms of %liquid in the spray (%L), the fraction and size distribution of solidified vs liquid droplets, and the distribution of droplet mass in the spray.

$CDP_2$ : The physical and thermal state of the surface onto which the droplets impact; this includes the fraction of solid and the surface roughness of the deposit.

*It is envisaged that $IPP_1$ through $IPP_6$ in Fig. 2 combine and entirely determine $CDP_1$.* Similarly, the parameter $CDP_2$ is entirely determined by $CDP_1$, $IPP_7$ and $IPP_8$. Knowledge of the optimal values of CDPs 1 and 2 will simplify the control scheme, and their values will depend upon the specific application. For example, the primary criteria for strip production are uniformity in thickness across the width of the strip (<2% variation in thickness) and minimization of surface-connected porosity. Hence the shape of the spray and parameters of substrate motion/temperature are most important. Manufacture of bulk preforms such as disk or billet necessitates close control over the top surface temperature and thickness of the partially liquid layer in order to maintain conditions of *incremental solidification* [28,5]. Thus the amount of liquid in the spray at impact must be carefully controlled (Fig. 3) : if the spray contains a high fraction of solid upon impact (%L->0), a majority of the droplets will be solidified and no coherent deposit will be formed; the process will then resemble powder production. On the other hand, spray casting will be analogous to conventional casting if the spray contains a high fraction of liquid at impact (%L->100). The "ideal" fraction of liquid is a value in between the two extremes cited above and must contain sufficient liquid to flow and fill the interstices between presolidified droplets. In addition, this ideal fraction of liquid must ensure that the impinging droplets "stick" to the surface of the growing deposit and maximize deposit yield.

Preform *yield* is dictated by the product of two efficiencies : (i) target efficiency, $\Pi_t$, which represents the fraction of droplets arriving at the substrate surface, and (ii) sticking efficiency, $\Pi_s$, which represents the fraction of droplets which adhere to the surface and contribute to preform growth. These factors are addressed in §3.3.1. The *shape* or geometry of the preform is determined by the combined effects of (i) the spatial distribution of droplet mass in the spray, (ii) the sticking efficiency of the droplets on arrival at the substrate, and (iii) motion of the substrate and/or spray. This is discussed in § 3.3.2. Finally, the *microstructure* in spray cast preforms is determined by (i) the condition of the spray at impact, (ii) the spatial distribution of solid particles after impact, and (iii) the time required for complete solidification of the preform. Preform yield, shape and microstructure must be controlled during the spray casting operation, however, the difficulty of process control is magnified by :

(i) the complex interdependencies between independent process parameters (e.g. melt superheat, atomizing gas pressure, .... ) and the dependent variables (e.g. droplet size distribution, droplet temperature profiles, preform density and microstructure, .... ), and

(ii) the need for sophisticated, non-invasive sensors due to the microscopic size of the droplets and the time scale of events which occur during the process.

## 3. SCIENTIFIC ASPECTS

In this section, the intermediate stages of the process are analyzed and a scheme is developed to relate the IPPs to the CDPs and subsequently to preform integrity in terms of yield, shape and microstructure. A "standard" set of independent process parameters is selected for the analysis based upon current operating conditions of the Osprey process on a pilot scale; this set is listed in Table I and it is utilized as a benchmark for all comparisons.

### 3.1 Atomization

The size distribution of atomized droplets is an important dependent parameter in spray casting since it governs the remainder of the deposition process. Typically, the mass-median droplet diameter is in the range 40–120μm depending upon the material and process parameters used, and the log-normal standard deviation is in the range 1.75–2.25.

Prior attempts to predict the size distribution of atomized droplets have met with limited success due to the complexity of the disintegration process [29-33]. Furthermore, the mean droplet sizes predicted by a fundamental analysis such as Bradley's [32] are not in satisfactory agreement with experimentally measured values. Therefore, it is convenient to determine the size distribution experimentally by collecting solidified droplets from the spray (by removing the substrate) and subjecting them to a size analysis [34,16,35]. Data on droplet sizes can then be correlated to the material and processing parameters during atomization by Lubanska's empirical relationship [33]:

$$d_m = K_L\, D\, [\, (1+1/GMR)\, (\upsilon_m / \upsilon_g)\, (1/We)\, ]^{m_L} \approx 13\cdot\sigma^3 \qquad \text{.... (1a)}$$

$$We = \rho_m\, V^2\, D / \gamma_{LV} \qquad \text{.... (1b)}$$

where $d_m$ is the mass-median droplet diameter, $\sigma$ is the standard deviation of the log-normal droplet size distribution, $K_L$ and $m_L$ are constants specific to atomizer design, D is the diameter of the metal stream, GMR is the ratio of gas : metal mass flow rates, $\upsilon$ is the kinematic viscosity, We is the Weber number, V is the gas velocity and $\gamma_{LV}$ is the surface tension of liquid metal. The atomizer-specific parameters $K_L$ and m in Eq. (1) were found to be ~ 100 and 0.5, respectively, for the Osprey atomizer. This correlation facilitates computation of $d_m$ and $\sigma$ under different processing conditions when experimental data is unavailable. $d_m$ can be decreased by increasing the melt superheat or gas:metal ratio, while substitution of argon in place of nitrogen as the atomizing gas is found to produce no significant effect on the droplet size distribution. Knowing $d_m$ and $\sigma$, the probability of finding a given droplet size, $P(d_i)$, for a log-normal distribution is given by [36]:

$$P(d_i) = 1/(\sqrt{2\pi}.\sigma).\ \mathbf{exp}\ \{\, (-1/2\sigma^2)\cdot \mathbf{log}(d_i/d_m)\, \} \qquad \text{.... (2)}$$

### 3.2 Transfer of Droplets (Metal Spray)

The metal spray comprises hot metal droplets surrounded by a high velocity gas jet. The gas accelerates and simultaneously cools/solidifies the droplets during their flight towards the substrate, Fig. 3. The shape of the spray can be approximated by a cone whose apex is at the point of atomization and its base is a circular area over which the droplets are deposited.

**3.2.1 Droplet Velocity:** Upon atomization, each droplet is accelerated towards the substrate by the surrounding high velocity atomizing gas. Therefore, the velocity of each droplet increases with flight distance until a point in flight when the droplet velocity equals the velocity of the decaying gas jet. Beyond this flight distance, the droplet will travel faster than the gas and consequently it will be decelerated.

The velocity profile of droplets in flight has been modeled by several investigators [37,38,9,13,39-41]. Most of these models are based on the expression by Ranger and Nicholls [42] derived from the momentum equation for the acceleration of water droplets in air:

$$F = m\frac{dV_d}{dt} = \frac{1}{2} C_D\, \rho_g\, V_r^2 \cdot A_c + mg \qquad \text{.... (3)}$$

where F is the force on the droplet, m is its mass, $V_d$ is droplet velocity, $C_D$ is the drag coefficient, $\rho_g$ is the density of the gas, $V_r = |V_g - V_d|$ is the relative velocity between the gas and the droplet, A is the droplet's cross sectional area, and g is the acceleration due to gravity. Data for the gas flow field is available in Refs. **[43-45,40,46]** and the expression for the drag coefficient is adopted from Ref. **[47]**.

Droplet velocities just prior to consolidation at a flight distance of 400mm are displayed in Fig. 4 for droplets of Al, Al-4.5%Cu, Cu, Ni and Fe; these were calculated from the model described in **[37,38,35]**. Depending primarily upon droplet mass, the velocities at consolidation are in the range 10-100m/s. The curves are bell-shaped because droplets smaller than a critical diameter ($\hat{d}$) have reached their peak velocity and are being decelerated by the gas, while droplets with dia. > $\hat{d}$ are accelerating in flight. The value of $\hat{d}$ increases with increasing flight distance and is a function of droplet mass (hence the curve is shifted to the right for Al).

Limited experimental measurements to date **[46,48,49]** have shown that the predicted velocity profiles are correct at least to an order of magnitude. However, with the current state-of-the-art, it is not possible to precisely measure the velocity of a single droplet since both velocity and diameter of the droplet must be measured simultaneously along the flight trajectory.

**3.2.2 Droplet Temperature/Extent of Solidification:** The variation of a droplet's temperature with flight distance can be divided into four stages, as shown schematically in Fig. 5(a). Upon atomization at flight distance X=0, the liquid droplet is at a temperature $T_i$ ($= T_L + \Delta T_s$), where $T_L$ is the liquidus temperature and $\Delta T_s$ is the melt superheat. In Stage I, the droplet cools primarily by losing heat to the surrounding gas via forced convection. Therefore the cooling rate is governed by the convective heat transfer coefficient, $h_g$, which in turn is a strong function of the difference in velocity between the droplet and the gas **[50]**:

$$h_g = K_g(2+0.6Re^{0.5}Pr^{0.33})(C_{g(avg)}/C_g)^{0.26}/d \qquad \text{.... (4a)}$$

$$Re = d\, V_r / \nu \qquad \text{.... (4b)}$$

where $K_g$ is the thermal conductivity of the gas, Re the Reynold's number, Pr the Prandlt number, $C_g$ is the specific heat of the gas, d is the droplet diameter, $V_r$ is the relative velocity and $\nu$ is the kinematic viscosity of the gas. Knowing $V_r$ from the droplet's velocity profile, the value of h is computed from Eq. (4) and it is employed in a simple heat balance to predict the variation of droplet temperature with flight distance **[37,38,9,5,39]** :

$$dT_d/dt = GMR \cdot h_g A_s (T_d - T_g) / C_P \qquad \text{.... (4c)}$$

where T is the temperature, t is time, GMR is the ratio of gas:metal mass flow rate, $A_s$ is the droplet's cross-sectional area, $C_P$ is the specific heat of the droplet and the subscripts d and g refer to the droplet and gas, respectively.

The liquid droplet continues to cool in Stage I until the nucleation temperature $T_n$ ($= T_L - \Delta T_n$) is reached, where $\Delta T_n$ is the degree of undercooling. Droplet undercooling and solidification must be included in these models in order to provide a realistic description of the droplet temperature profile in flight [37,35,9,39]. The dependence of the degree of undercooling on droplet size is given in [37,35]; it is found that the degree of undercooling decreases exponentially with increasing droplet volume.

Following nucleation at $T_n$, the droplet begins to solidify rapidly (Stage II - solidification during recalescence). Models for droplet solidification assume that nucleation occurs on the droplet's surface and a hemispherical solid-liquid interface advances across its volume as a function of time [51-53], Fig. 5(a). The temperature *increases* during solidification (i.e. the droplet "recalesces") since the release of latent heat is faster than the rate of heat extraction by the surrounding gas. Recalescence continues until an arrest temperature is reached close to the liquidus temperature. Subsequent solidification (Stage III - "normal" solidification) occurs with attendant drop in temperature and is governed by the rate of heat extraction by the gas. The cooling rate in Stage III may be derived from Eq. 4(c) by introducing an additional term to account for the latent heat of fusion. Solidification is terminated at the solidus temperature (or at eutectic temperature for non-equilibrium solidification according to the Scheil equation). In the final stage of cooling (Stage IV), the droplet cools in the solid state by forced convection and Eq. 4(c) is applicable.

The predicted variation of temperature with flight distance is shown in Fig. 5(b) for three droplets of Al-4.5%Cu alloy of diameters: $d_m$=59μm, $d_m/\sigma$=37μm and $d_m \cdot \sigma$=95μm. Similarly, the degree of solidification of each droplet (i.e. % liquid in droplet) is plotted in Fig. 6(a). It is observed that the distance required for complete solidification increases with increasing droplet diameter. Similar profiles of temperature and solidification are computed for a number of droplets with diameters in the range $d_m/3\sigma$ to $d_m.3\sigma$. The extent of solidification of each droplet at X=400mm (i.e. just prior to consolidation) was selected from these results and is plotted in Fig. 6(b). The juxtaposition of the curves indicates that *droplets of high melting materials* (e.g. Fe) *will cool faster than those of low melting materials* (e.g. Al-4.5%Cu) due to a greater difference in temperature between the metal and atomizing gas. From the figure, *the condition of droplets arriving at deposition (400mm below the gas nozzles)* can be summarized as follows:

(i) droplets of diameter less than a critical value d* are completely solidified upon impact ($\%L_d = 0$). Typically d* is predicted to be in the size range 30μm-125μm for the alloys described, and increases with increasing melting point of the alloy. This corresponds to a significantly large fraction of presolidified droplets due to the bi-modal population distribution [37].

(ii) droplets of diameter greater than d* impact the deposition surface in a "mushy" condition with varying fraction of liquid. These droplets comprise a solidified dendritic skeleton, as observed from glass slides [51,35,49].

(iii) only droplets greater than about 300µm for Al and 900µm for the other metals arrive at the deposition surface in a completely liquid state.

**3.2.3 State of the Spray ($CDP_1$):** The models desc ibed above retain the identity of each droplet and describe the spray on a microscopic scale, i.e. at a high level of resolution. *For purposes of process control*, it is advantageous to combine characteristics of individual droplets and, at the expense of resolution, derive average values which represent the state of the spray at a macroscopic level. For example, the fraction of liquid in individual droplets may be averaged to determine the ratio of solid : liquid in the spray ($\%L_{spray}$ in Fig. 3). The value of $\%L_{spray}$ at deposition is a critical parameter in spray casting ($CDP_1$). Similar averaging may be carried out with droplet enthalpy and mass, as discussed below.

**(a)** % Liquid in Spray and Spray Enthalpy: The fraction of liquid in the spray at any flight distance is the weighted average of the fraction of liquid in the individual droplets:

$$\%L_{spray}(X) = \sum_{i=1}^{n} [1-f_s(d_i,X)]\cdot P(d_i)\cdot 100 \qquad \text{.... (5a)}$$

where $\%L_{spray}$ is the percentage of liquid in the spray at flight distance X, $f_s$ is the fraction solid in a droplet of diameter $d_i$, and $P(d_i)$ is the weight fraction of droplets in the size range $d_i$ to $d_{i+1}$ (Eq. 1). Summation is carried out from $d_i = d_m/3\sigma$ to $d_m\cdot 3\sigma$ in order to cover 99% of the range of droplet diameters produced during atomization. Similarly, spray enthalpy $H_{spray}$ is computed by averaging the enthalpy of individual droplets:

$$H_{spray} = \Sigma\, H_d(d_i, X)\cdot P(d_i) \qquad \text{.... (5b)}$$

where $H_d$ is the enthalpy of a given droplet of diameter $d_i$ at flight distance X.

The variation of $\%L_{spray}$ with X is plotted in Fig. 7(a) for five alloys under a fixed set of parameters in order to compare the effect of material properties. The shallow slope of the curves in the initial stages of flight ($0<X<25$mm) is due to the release of superheat and undercooling of the droplets prior to solidification. Thereafter the solidification rate reaches its highest level after a distance of ~50mm and decreases monotonically with flight distance. Among the *material* parameters, *the melting point,* $T_m$*, and the value of* $H_{FR}$[**] *have the most significant effect on the thermal condition of the spray.* This is evidenced by copper which solidifies most rapidly since it has the smallest value of $H_{FR}$. On the other hand, aluminum and Al-4.5%Cu possess high values of $H_{FR}$ and a low $T_m$; hence their solidification is significantly slower than the other materials. The influence of *process parameters* (IPPs), such as the type of atomizing gas and the gas:metal ratio, is illustrated in Fig. 7(b) for the spray deposition of Al-4.5%Cu alloy. It is predicted that even a four fold increase in the flow rate of argon is not as effective as nitrogen in cooling the spray due to its lower thermal diffusivity/conductivity.

*The substrate must be positioned at a suitable distance below the gas nozzles (depending upon the material and process parameters) so that the spray contains the "desired" percentage of liquid at impact.* During deposit build up, the effective spray height decreases with time and results in a corresponding increase in the amount of liquid carried into the deposit, Fig. 7. The change in $\%L_{spray}$ with deposit build up becomes significant at operative distances less than about 300mm for the aluminum alloys under these conditions. This effect is compounded by the increase in deposition rate with decreasing flight distance. Therefore, in order to maintain uniformity in deposition conditions, it is necessary to continuously increase the distance between the emplaced substrate and the point of atomization in order to maintain a constant spray height at the deposition surface.

**(b)** Droplet Mass Distribution within the Spray: The flux of droplets in the spray is a maximum at the axis of the spray and decreases towards its periphery. This variation, i.e. the *deposition profile,* is governed by $IPP_1$ to $IPP_6$ and is independent of substrate configuration and motion. Since it is difficult to measure the droplet flux directly, the flux may be estimated indirectly by measuring its effect, i.e. the rate of deposit growth, $\dot{Z}$ (mm/s). $\dot{Z}$ is defined as the thickness of a deposit that would build up per unit time on a flat, stationary substrate positioned normal to the spray axis. For example, the traces from a video recording of deposit growth are shown in Fig. 8 at different time intervals from the start of deposition [37,35,38]. The dependence of $\dot{Z}$ on the radial distance from the spray axis, r, is derived from this figure and is found to follow a normal 'Gaussian' curve:

$$\dot{Z}(r) = dZ/dt = \dot{Z}_0 \exp(-\beta r^2) \qquad \text{.... (6)}$$

where Z is the thickness of the deposit measured parallel to the spray axis (z direction), $\dot{Z}_0$ is the maximum growth rate (at the spray axis, r=0) and β is the radial distribution coefficient that governs the spread of the spray. $\dot{Z}_0$ and $\beta$ were measured to be ~ 5.25mm/s and 0.0005 $mm^{-2}$, respectively, at a distance of 400mm below the gas nozzles.

---

[**] $H_{FR}$ = heat in the freezing range of the alloy = latent heat ($H_f$) + specific heat ($C_P \Delta T_f$)

During the production of billets/disk preforms via the Osprey process, it is beneficial to have a narrow, focussed spray in order to increase the yield on a small collector area. Therefore, the coefficient '$\beta$' in Eq. (6) must be kept at a minimum value. On the other hand, it is desirable to transform the deposition profile into an ellipse during strip casting in order to increase the width and uniformity in thickness of the strip produced. This can be achieved by employing a "*linear*" atomizer wherein the metal delivery nozzle and the surrounding gas jets have a rectangular cross section [54]. The resulting deposition profile across an elliptical spray can be described by the following (general) form of Eq (6): $\dot{Z} = \dot{Z}_{max} [\ \beta_1 x^2 + \beta_2 y^2\ ]$. It is also possible to tailor the spray to any desired shape (and deposition profile) by the utilization of *tertiary gas jets* [55] and/or magneto-hydrodynamic forces (MHD).

## 3.3 Formation of the Preform

**3.3.1 Droplet Consolidation:** When a substrate (i.e. target) is introduced into the spray of droplets, the droplets impinge and consolidate on the substrate to form a deposit. Only a portion of the droplets reach the target; this fraction is defined as the *target efficiency* of the spray, $\Pi_t$. Furthermore, only a fraction of the droplets arriving at the substrate will "stick" and contribute to deposit growth; the remaining droplets will "bounce-off". The fraction which adheres is termed the *sticking efficiency*, $\Pi_s$. Deposit yield is determined by the product of these two efficiencies:

$$\textbf{Yield \%} = (\Pi_t \, . \, \Pi_s) \cdot 100 \qquad .... (7)$$

$\Pi_t$ depends upon the size of the substrate, the shape of the spray, the stand-off distance, the distribution of droplets within the spray and the substrate motion. $\Pi_s$ is a metallurgical parameter which is governed by the state of the spray at impact ($CDP_1$), the state of the top surface ($CDP_2$), and by the substrate configuration/motion. Estimation of $CDP_1$ was described in §3.2.3 and the determination of the latter two parameters will be addressed in the following sections. A flow chart depicting the procedure adopted is provided in Fig. 9.

**3.3.2 Preform Shape:** The shape of the preform is governed by the mass distribution in the spray at impact, the sticking efficiency and the parameters of substrate motion (e.g. rotation speed, translation speed, limits of translation, etc.). Optimum values of the variables of substrate motion can be determined *a priori* by a mathematical model in which the state of the spray at consolidation (i.e. Eq. 6) is coupled with a model for substrate motion [22,35,38]. For a given substrate (i.e. a disk collector, a tubular mandrel, or a roller), this model selects a location P(x,y) on its surface and computes the growth of thickness during deposition. The calculations are then repeated for different locations which are defined by a grid on the substrate surface.

The magnitude of thickness increments during each time step at any location P(x,y) is governed by the radial distance $R_{(x,y)}$ between P(x,y) and the axis of the spray (Eq. 6). If the substrate is stationary, the value of $R_{(x,y)}$ is constant during the entire deposition cycle. If the substrate is non-stationary, $R_{(x,y)}$ changes with time depending upon the motion imparted, i.e on the locus of P with respect to the spray axis. Summation of the thickness increments over the deposition cycle yields the final thickness at each location on the substrate. Shape or geometry of the preform is defined by a bounding surface which connects all points (x,y,Z) where Z is the calculated thickness at the grid point (x,y) on the substrate surface.

A three-dimensional representation of the final deposit shape after 40s of spraying onto a horizontal stationary substrate is shown in Fig. 10(a). Similarly, the build up of a deposit on a stationary substrate inclined at an angle of 35° to the horizontal is shown in Fig. 10(b); inclination of the substrate facilitates the build up of deposits with edges nearly perpendicular to the substrate surface.

The predicted geometry of an axisymmetric disk preform, produced by spraying for 40s on a 120mm dia. collector, is represented in Fig. 10(c). The collector was rotated at $\omega$ = 200 rpm and simultaneously translated back and forth under the spray such that the spray axis reciprocated between the limits $x_1$=-60mm and $x_2$=-35mm (i.e. stroke length $x_s$=25mm). The speed of reciprocation was set at $V_x$ = 20 mm/s, such that the spray traversed approximately one stroke length for every four rotations of the collector. From the volume of metal deposited, the *target efficiency was calculated as ~72%.*

This model to predict preform shape is also being utilized to predict the geometry of tubes, billets and/or strip [20,56,22] produced via spray casting. In order to produce wide strip (~1m in width), a "scanner atomizer" is used to oscillate the spray at a frequency of 3-7 Hz, Fig. 1.

**3.3.3 Preform Microstructure:** Grain size and porosity are the primary indices of microstructure. Prior research [37,35,22] suggests that grain size in spray cast preforms is determined by (i) the size distribution of solidified particles arriving from the spray, (ii) the spatial distribution of these particles after impact, and (iii) the time required for complete solidification, $t_f$. At a given spray height, the size distribution of solid particles is obtained from the size distribution of droplets in the spray and the diameter of the largest solidified droplet (d*) at that flight distance. Predicted values of d* at X=400mm can be obtained from Fig. 6(b). The spatial distribution of solid particles after impingement is strongly dependent upon their spatial distribution in the spray and upon secondary effects such as droplet fragmentation, bouncing-off, etc. which are difficult to quantify.

*Preform Solidification and Cooling (CDP$_2$):* In order to effect complete solidification, a total amount of heat, $H_S$ ($H_S = C_P \cdot \Delta T_s + H_{FR}$) must be removed from the metal, where $C_P$ is the specific heat, $\Delta T_s$ is the melt superheat at atomization and $H_{FR}$ is the heat contained in the freezing range of the alloy. Let $H_{gas}$ represent the amount of heat removed by the gas during flight, as shown schematically in Fig. 3. Thus, the amount of heat which must be removed *after* deposition in order to complete the solidification is given by $H_{rem}$, Fig. 3 :

$$H_{rem}\,(X) = (C_P \cdot \Delta T_s + H_{FR}) - H_{gas}(X) \qquad \text{.... (8)}$$

where X is spray height.

*Continuum Models :* Two approaches have been adopted to calculate the solidification time, $t_f$, required to remove the heat $H_{rem}$ from the preform. In the *continuum* approach **[37,38,9,57]**, $t_f$ is computed by a macroscopic energy balance between the heat influx from the spray $H_{rem}$, the mass influx $\dot{Z}$, heat extracted by the substrate $Q_s$, and heat extracted by the atomizing gas $Q_g$. This is shown schematically in Fig. 11(a). Since solidification time varies with location within the preform, the thickness of the preform at any substrate location P(x,y) is divided into small volume elements arranged along the growth direction. A moving boundary transient heat conduction equation is solved numerically to obtain the enthalpy, temperature and fraction solid within the volume elements as a function of time [37,38,35]:

$$\rho\,(dH/dt) = (1/Z^2)\cdot(d/d\eta\;(K\;dT/d\eta)) + (\rho\eta/Z)\cdot(dH/d\eta)\cdot\dot{Z} \qquad \text{.... (9)}$$

boundary conditions:

$$\text{bottom surface : } (K/Z)\;(dT/d\eta) = Q_s = h_s\;(T_b - T_s) \qquad \text{.... (9a)}$$

$$\text{top surface : } \rho\;(H_{spray} - H)\;(dZ/dt) = (K/Z)\;(dT/d\eta) + Q_g \qquad \text{.... (9b)}$$

where $\rho$ is the density, H is the enthalpy, Z is the thickness of the deposit at any instant, $\eta = z/Z$, z is distance into the deposit measured from the substrate upwards, $\dot{Z}$ is the deposit growth rate and t is elapsed time from the start of deposition. Solidification is completed when the amount of heat removed from each volume element is equal to $H_{rem}$.

Heat flux from the deposit to the substrate has been measured with a heat flux sensor embedded in the substrate [35]; measured values of the heat transfer coefficient are a maximum of ~$10^5$ W/m$^2$/K at the start of deposition and decrease rapidly to ~ 500 W/m$^2$/K within a few seconds. This decrease is attributed to the formation of an "air gap" between the deposit and the substrate due to contractional stresses upon solidification. Similarly, the heat transfer coefficient for the gas cooling at the top surface of the deposit is estimated to be ~200 W/m$^2$/K.

Sample predictions of the continuum model are shown in Fig. 12 for the spray deposition of the Al-4.5%Cu disk whose shape is shown in Fig. 10(c). Deposition was carried out onto a water-cooled, circular substrate which was simultaneously rotated and translated under the spray to achieve a cylindrically shaped preform, as shown in Figs. 1 and 10(c). The "deposition line" in Fig. 12(a) is the predicted growth of thickness at the *center* of the circular substrate. This growth of thickness with time depends upon the locus of the disk under the spray, and it was derived from the model to predict preform shape. It is observed that the disk grows to a height of ~ 7cms during 40s of deposition and remains at a constant height thereafter.

The isothermal lines in Fig. 12(a) provide the variation of temperature and volume fraction of solid ($f_s$) in the disk along its height as a function of time. During deposition (i.e. the first 40s), it is observed that the top surface of the disk is hotter than the bottom due to the influx of heat and mass from the spray. With continued deposition, the fraction of solid at the top surface decreases to a minimum value of ~ 83%; this is marginally greater than the 80% solid in the spray, due to gas cooling at the top surface. Once deposition is completed, the top surface begins to cool/solidify rapidly due to gas cooling at the top surface, and the last liquid to freeze is at a height of ~ 4.5 cms above the substrate surface. The interval between the deposition line and the $f_s$=1 contour provides the local solidification time, $t_f$. It is observed that the disk preform solidifies over a period of 70-100s and experiences a cooling rate < 20°C/s. However, it must be emphasized that the solidification process is not entirely "slow" but occurs in two stages : a majority of the solidification occurs in flight under conditions of rapid solidification and only a small fraction of the liquid (10-40%) which is carried into the deposit undergoes relatively slow cooling. Therefore it is desirable to maximize the heat removal during flight to the extent that the amount of liquid carried into the deposit is just sufficient to consolidate the presolidified droplets.

The partially liquid layer ($f_s$<1.0) forms on the surface of the preform during deposition due to a slight imbalance between the deposition rate and the rate of heat extraction, Fig. 12(a). This is considered beneficial to the microstructure of spray cast preforms since the resultant increase in local solidification time allows time for fluid flow into interstices between presolidified droplets. However, the thickness of the layer must be controlled in order to maintain conditions of "incremental solidification" [28] and hence achieve uniformity in structure throughout the thickness of the deposit. The fraction of solid in the layer is estimated to be >60%; liquid fractions greater than ~0.4 may not be feasible since the apparent fluid viscosity declines sharply beyond this value [58] and a mold will be required to contain the flow. In addition, a second constraint is placed on the minimum viscosity of the fluid by the high velocity of the gas and centrifugal force imposed by rotation of the substrate.

The predicted variation of temperature with time at the top, middle and bottom of the disk are shown in Fig. 12(b). Similar results have been obtained experimentally by measuring the temperature in the preforms with thermocouples at selected heights above the substrate surface [35,46]. It is observed that the temperature of the top surface of the disk preform oscillates in a cyclic manner corresponding to each pass under the spray. The frequency of these oscillations is governed by the reciprocation/rotation speed and the limits of reciprocation (i.e. stroke length), while the temperature range over which the oscillations occur depends upon the deposit-gas heat transfer coefficient and the thermal properties of the alloy. Oscillations in temperature are undesirable, particularly if they occur over a temperature range over which the surface temperature decreases below the solidus. Under these conditions, the surface will completely solidify in the interval between two successive passes under the spray; this results in poor bonding between the "layers" thus produced.

Grain size and segregate spacing in the preform are larger than those in atomized powders but *smaller* than the values based on empirical correlations of dendrite arm spacing and cooling rates predicted by the continuum model [37,57,59]:

$$d_s = d_0 \exp (t_f)^m = d_1 \exp (\dot{T})^n \qquad \text{.... (10)}$$

where *coefficients* $d_0$ *and* $d_1$, *and the exponents* $m$ *and* $n$, *are dependent on the material.* Although the predicted grain size is found to follow the same trend as the experimental data [37,57,9], it is higher in magnitude by a factor >2. Overestimation of the grain size and/or segregate spacing from such equations may be due to (i) the two-stage solidification process in spray casting, (ii) retarded coarsening of the dendrite arms at a high volume fraction of solid [60], and (iii) nucleation by presolidified droplets from the spray. Therefore knowledge of the temperature / cooling rate in the preform is not sufficient to predict the grain size.

*Discrete Event Models :* The second, *non-continuum* approach to model preform solidification has been developed recently [56,57]. Unlike the continuum model in which deposit growth is assumed to occur continuously, the non-continuum / discrete-event models are more realistic in the sense that deposit growth is assumed to occur in discrete steps by the addition of splats, Fig. 11(b). Individual droplets impact on the pre-existing surface and spread to form a splat in microseconds [61-63]. The splat then undergoes cooling and solidification via conduction through the bottom surface and via convection at the top surface. This continues until the next droplet arrives after a time interval $\delta t$ between successive impacts. This sequence of events continues for every new splat arriving at the top surface, Fig. 10(b).

While conceptually more accurate than the continuum approach, the drawbacks of the discrete-event model are that it is computationally intensive and there is uncertainty in the values of input parameters required to facilitate the computations (e.g. splat thickness, interval between splats, ...). Values of splat thickness $\delta x$ are estimated writing $d_{splat} = \xi d_m$, where $\xi$ typically has a value between 3 and 6, assuming a random distribution of spherical droplets of average diameter, $d_m$ [56,61]. A mean droplet diameter, $d_m$ of 100μm yields splat thicknesses in the range 7.5-15μm and a splat thickness of 10μm is used. The calculation for $\delta t$ is made incorporating the measured log-normal droplet size distribution. For the observed droplet size distributions, estimates of $\delta t$ lie in the range 0.8-4ms and an order of magnitude value of 1ms of $\delta t$ is utilized.

The discrete-event model predicts cooling rates of the order of $10^3$°C/s during the initial stages of deposition, which are higher than the predictions of the continuum models. However, both continuum and discrete-event models predict the formation of a partially liquid layer after a short time interval (~0.5s) and their predictions appear to converge after this period. Implications are that the predictions of the continuum approach are reasonable and valid after the time corresponding to the formation of the partially liquid layer.

**(d) Degree of Porosity in the Preform :** The predicted values of $\%L_{spray}$ upon deposition are at the low end of the range, i.e 10%–40%. This suggests that only a small fraction of liquid is required to consolidate the presolidified droplets during deposition, and that the mechanism of droplet consolidation in spray deposition resembles liquid phase sintering [63,64]. Therefore, the level of porosity in the preforms is determined primarily by a balance between the solid:liquid ratio being deposited and by the efficiency of packing of the solid particles. Given a packing efficiency $\Pi_p$, the desired amount of liquid is the minimum quantity which will flow and fill the interstices between solid particles; any quantity less than this value will result in an amount of porosity given by:

$$\%P = [\,(100-\Pi_p) - \%L_{spray}\,(1-\beta_s)\,]\cdot 100 \qquad \text{....(11)}$$

where $\beta_s$ is the solidification shrinkage for the alloy and $\Pi_p$ is governed by the state of the spray.

*Effect of Substrate Characteristics:* The effect of physical and thermal properties of the substrate on preform characteristics is predominant only during the initial stages of deposit growth, and it is a strong function of the degree of contact at the interface. Smoothness of the substrate surface determines the degree of mechanical interlocking/adhesion between the deposit and the substrate; if the degree of contact is poor, thermal properties of the substrate exert *minimal influence* on preform solidification. For example, a metallic substrate (e.g. copper or steel) produces a high rate of heat extraction in the initial stages of deposition due to a good contact. This results in the formation of a pronounced initial chill layer (~1mm thick) with attendant porosity (~10-15%). However, the heat extraction decreases after 1-2 s due to the formation of an air gap between the deposit and the substrate. A refractory substrate (e.g. alumina) has been found to decrease the level of porosity in the initial stages; this effect is due to the lower thermal conductivity of the refractory. It is also possible to coat the surface of the substrate with non-conducting coatings (e.g. boron nitride) to control the heat transfer coefficient at the interface.

Heat flux into the substrate can be decreased by increasing the substrate temperature. Ideally, a high substrate temperature ($>0.8\ T_m$) is desirable during the initial period of deposition (~2s) in order to reduce the level of porosity at the bottom surface of the deposit. Subsequently, the temperature should be maintained at or near room temperature (e.g. by water cooling) in order to sustain the heat flux and decrease the time required for deposit solidification. Preheating of the substrate is expected to promote bonding between the substrate and the deposit due to reduction in the cooling rate; this approach is being utilized in the manufacture of tubes on emplaced mandrels.

## 4. SUMMARY

- Successful utilization of spray casting requires optimization of at least eight independent process parameters to achieve desired preform shape, microstructure and yield. The basis of the optimization is to achieve desired values of two critical dependent parameters of the process, namely the physical and thermal state of (i) the spray just prior to consolidation, and (ii) the state of the surface onto which the droplets impact.

- Velocity of droplets during flight is primarily a function of their mass. Droplet velocities predicted from fluid flow analyses are in the range 10-100 m/s under standard operating conditions of the Opsrey process. Experimental determination of droplet size and velocity are currently limited due to the microscopic size of the droplets and the time scale of droplet flight (a few milliseconds).

- Density, melting point and heat contained within the freezing range of the alloy are the three significant material parameters which affect the state of the droplets/spray at impact. The diameter of the largest solidified droplet at X=400mm ranges from 30μm-125μm for the alloys investigated and increases with increasing melting point. The percentage of liquid in the spray at X=400mm ranges from ~5% for Cu to ~35% for aluminum and its alloys under identical spraying conditions.

- Both melt superheat and gas:metal ratio affect $\%L_{spray}$ to a similar extent (~10%) when their value is changed by 50%; however increase in the melt superheat increases $\%L_{spray}$ while a higher value of GMR produces a colder/more solidified spray at any flight distance. Changing the atomizing gas to argon (from nitrogen) does not significantly alter the droplet size distribution, however, even a four fold increase in the flow rate of argon is not as effective as nitrogen in cooling the spray.

- Preform yield can be represented by the product of target and consolidation efficiencies. Target efficiency for the production of a 120mm dia. disk preform was calculated as ~72% from the model to simulate preform shape/geometry. This model can be employed to predict the build up of thickness/shape of disks, billets, tubes and/or strip via spray deposition.

- Measured values of heat flux across the deposit-substrate interface indicate that the heat transfer coefficient is a maximum of ~$10^5$ W/m/K in the initial second but decreases to ~500 W/m/K during the bulk of the deposition period.

- Grain size in the preforms is determined by the spatial distribution of solid particles from the spray and cooling rates after deposition. The solidification process is two stage : a majority of the solidification ($\approx 100-\%L_{spray}$) occurs in flight at cooling rates in the range $10^3-10^4$ K/s while the remainder of the solidification occurs at <10°C/s.

## REFERENCES

1. W.A. Tony: Iron & Steelmaker, p.11, December 1987

2. Wright, P.W., Materials and Design, 8, 3, May/June (1987)

3. Net Shape Technology in Aerospace Structures, I-IV, National Academy Press,Washington, D.C., (1986)

4. Leatham, A.G., Reichelt, W. and Metelmann, "Near Net Shape Manufacturing Processes", eds. Lee, P. W. and Ferguson, B. L., ASM International, p. 259 (1988)

5. Evans, R.W., Leatham, A.G. and Brooks, R.G., Powder Metallurgy, 28, 1, p.13 (1985)

6. Apelian, D., Gillen, G. and Leatham, A., "Processing of Structural Metals by Rapid Solidification", eds. Froes, F.H. and Savage, S.J., Amer. Soc. for Metals International, p.107 (1987)

7. Lavernia, E.J., Rai, G. and Grant, N.J., Int. J. Powder Metallurgy, 22, 1, p.9 (1986)

8. Lavernia, E.J. and Grant, N.J., Metal Powder Rep., 4, p.255 (1986)

9. E. Gutierrez-Miravete, E.J. Lavernia, G.M. Trapaga, J. Szekely and N. J. Grant: Metall. Trans., 20A, 1, p.71, January 1989

10. Apelian, D., Paliwal, M., Smith, R.W. and Schilling, W.F., Int. Metals Rev., 28, 5, p.271 (1983)

11. Singer, A.R.E., J. Inst. Metals, 100, p.185 (1972)

12. Singer, A.R.E., Metals and Materials., 4, p.246-257 (1970)

13. Singer, A.R.E., in proc. of "High Density P/M Consolidation Processes", P/M 84, Toronto, June (1984)

14. Apelian, D., Kear, B.H. and Schadler, H.W., in "Rapidly Solidified Crystalline Alloys", ed. Das, S.K., Kear, B.H. and Adam, C.M., The Metallurgical Society, Warrendale, PA, p.93 (1985)

15. Leatham, A.G., Ogilvy, A.J.W., Chesney, P.F. and Metelmann, O., Modern Developments in Powder Metallurgy, eds.: P. U. Gummeson and D. A. Gustafson, Metal Powder Industries Federation, Princeton, NJ, Vol. 18-21, In Press (1988)

16. Osprey Metals Ltd., private communication with R. G. Brooks and A.G. Leatham (1988)

17. Bricknell, R.H., Met. Trans., 17A, 4, p.583 (1986)

18. Fiedler, H.C., Sawyer, T.F and Kopp, R.W., "Spray Forming-An Evaluation Using IN718", General Electric Technical Information Series, 86CRD113, May (1986)

19. Annavarapu, S, Lawley, A. and Apelian, D., Met. Trans, 19A, 12, p.3077 (1988)

20. Lawley, A. and Apelian, D., "A Fundamental Study of Thin Strip Casting of Plain Carbon Steel by Spray Deposition", NSF Report MSM-8519047, National Science Foundation, Washington D.C. (1988)

21. Mannesman Demag, W.Germany, private communication with Reichelt,W. (1989)

22. D. Apelian, A. Lawley, P. Mathur and X. Luo, Modern Developments in Powder Metallurgy, eds.: P. U. Gummeson and D. A. Gustafson, Metal Powder Industries Federation, Princeton, NJ, Vol. 19, p.397(1988)

23. Moran, A. and Palko, W. A., in "Progress in Powder Metallurgy", eds. Freeby, C.L. and Hjort, H., Metal Powder Industries Federation, Princeton, NJ, 43 (1987)

24. R.P.Singh and A. Lawley, Modern Developments in Powder Metallurgy, eds.: P. U. Gummeson and D. A. Gustafson, Metal Powder Industries Federation, Princeton, NJ, Vol. 19, p.489 (1988)

25. Duszczyk, J., Estrada, J.L., Korevarr, B.M., deHaan, T.L.J., Bialo, D., Leatham, A.G. and Ogilvy, A.J.W., Modern Developments in Powder Metallurgy, eds.: P. U. Gummeson and D. A. Gustafson, Metal Powder Industries Federation, Princeton, NJ, Vol. 19, p.441 (1988)

26. Faure, J.F. and Ackermann,L.;, Modern Developments in Powder Metallurgy, eds.: P. U. Gummeson and D. A. Gustafson, Metal Powder Industries Federation, Princeton, NJ, Vol. 19, p.425 (1988)

27. Y. Unigame : "An Analysis of Oxide Dispersion Strengthening of Ferrous Alloys during Spray Casting", M.S. Thesis, Drexel University, Philadelphia (1989)

28. A.R.E. Singer and R.W. Evans : *Met. Tech.*, Vol. 10, p.61 (1983)

29. Lawley, A., J. Metals, 33, 1, p.13 (1981)

30. A. Unal: Metall. Trans., 20B, 2, 1989

31. Lawley, A and Doherty, R.D., in "Rapidly Solidified Crystalline Alloys", ed. Das, S.K., Kear, B.H. and Adam, C.M., The Metallurgical Society, Warrendale, PA, p.93 (1985)

32. Bradley, D., J. Phys. D., 6, p.1724 (1973)

33. Lubanska, H., J. Met., 22, 2, p.45 (1970)

34. R Dunstan, Leatham, A.G., Negm, M.I. and Moore, C., Opsrey Metals Ltd., presented at National P/M Conference, Philadelphia, May 3-6, (1981)

35. Mathur, P.C., "Analysis of the Spray Deposition Process", Ph.D. Thesis, Drexel University, Philadelphia (1988)

36. German, R.M., "*Powder Metallurgy Science*", Metal Powder Institute Federation, Princeton, NJ (1984)

37. Mathur, P., Apelian, D. and Lawley, A., Acta Metall., 37,2, p.429, (1989)

38. Mathur, P., Wei, D. and Apelian,D.; Modeling and Control of Casting and Welding Processes IV, eds. A. F. Giamei and G. G. Abbaschian, The Minerals, Metals and Materials Soc., Warrendale, PA, p.275 (1988)

39. Kallien, L.H., Hansen, P.N. and Sahm, P.R.; Modeling and Control of Casting and Welding Processes IV, eds. A. F. Giamei and G. G. Abbaschian, The Minerals, Metals and Materials Soc., Warrendale, PA, p.543 (1988)

40 Liu, J., Arnberg,L., Backstrom,N., Klang, H. and Savage, S.; Mat. Sci, Eng., 98, p. 43 (1988)

41. Lavernia, E.J., Gutirrez,E.M., Szekely, J. and Grant, N.J., "Progress in Powder Metallurgy 1987", Metal Powder Industries Fed., Princeton, NJ, 43, p.683 (1987)

42. Ranger, A.A. and Nicholls, J.A., AIAA Journal, 7 (1969)

43. Connelly, S., Coombs, J.S. and Medwell, J.O., Metal Powder Report, 41, 9, p.653-661 (1986)

44. Anderson, A.R. and Johns, F.R., A.S.M.E., 21, p.13 (1955)

45. Elghobashi, S., Abou-Arab, T., Rizk, M. and Mostafa, A., Int. J. Multi-phase Flow, 10, 6, p.697 (1984)

46. Bewley, B. and Cantor, B., in Int. Conf. on Rapidly Solidified Materials, eds. Lee, P. and Carbonara, R., Amer. Soc. for Metals, Ohio, p.15 (1986)

47. Kurten, et. al., "Bubbles, Drops and Particles", ed. Clift, R., Grace, J.R.,and Weber, M.E., Academic Press, N.Y. (1978)

48. Bauckhage,K., Flogel,H., Fritsching,U., Hiller,U. and Schone,F.; "Simultaneous Size and Velocity Measurements in Multiphase Flow Systems / Some Extentions of the Phase Doppler Method", Proc. 3rd Intl. Symp. on Laser Anemometry, Amer. Soc. Mech. Eng., Winter Mtg., Boston, Mass. U.S.A (1987)

49. Mathur, P.C., "A Study of DropletFlight during Spray Forming", M S. Thesis, Drexel University, Philadelphia (1986)

50. Ranz, W.E. and Marshall, W.R., Chemical Engineering Progress, 48 (1952)

51. Apelian, D., Lawley, A., Gillen, G. and Mathur, P., "Spray Deposition: A Fundamental Study of Droplet Impingement, Spreading and Consolidation", ONR Technical Report 4, NR 650-025, Contract N 00014-84-K-0472, Office of Naval Research, Arlington, VA (1988)

52. Levi, C.G. and Mehrabian,R., Met. Trans., 13A, p.221 (1982)

53. Boettinger, W.J., Coriell, S.R. and Sekerka, R.F., Mat. Sci. Eng., 65, 1, p.27 (1984)

54. Grant, N.J., Casting of Near Net Shape Products, eds. Y. Sahai, J.E. Battles, R.S. Carbonara and C.E. Mobley, TMS, p.203, 1988

55. Nippon Steel Corp., Japan - private communication with Y.Tomita (1989)

56. Annavarapu, S., Ph.D. Thesis, Drexel University, Philadelphia (1989)

57. E. Gutierrez-Miravete, G.M. Trapaga and J. Szekely: Casting of Near Net Shape Products, eds. Y. Sahai, J.E. Battles, R.S. Carbonara and C.E. Mobley, TMS, p.133, 1988

58. Spencer, D., Mehrabian, R. and Flemings, M.C., Met. Trans., 3A, p.1925 (1972)

59. H. Jones : "Rapid Solidification Processing : Principles and Technologies", eds. R. Mehrabian, B.H. Kear and M. Cohen, Claitor's Publishers, Baton Rouge, LA (1978)

60. R.D. Doherty : *Met. Sci.*, Vol. 16, p.1. (1982)

61. J. Madjeski: Int. J. of Heat and Mass Transfer, 19, p.1009 (1976)

62. H. Jones: Rapid Solidification of Metals and Alloys, The Institution of Metallurgists, p.43, 1982

63. Garrity, E., Ph.D. Thesis, Drexel University, Philadelphia (1989)

63. German, R.M., "Liquid Phase Sintering", Plenum Press, NY (1985)

64. Zovas, P.E., German, R.M., Hwang, K.S. and Li, C.J., J. Metals, 35, 1, p.28 (1983)

## ACKNOWLEDGEMENTS

The authors wish to acknowledge discussions with and assistance from Dr. Alan Lawley, Dr. Dan Wei and Dr. Suresh Annavarapu.

## Glossary of Terms

| | |
|---|---|
| $A_c$ | cross-sectional area |
| $A_s$ | surface area |
| $C_g$ | specific heat of gas |
| $C_p$ | specific heat of metal |
| $C_D$ | drag coefficient |
| CDP | critical dependent parameter |
| $d$ | droplet diameter |
| $d_s$ | dendrite arm spacing, grain size |
| $d_m$ | mean droplet diameter |
| $d_0, d_1$ | constants in Eq. (10) |
| $d^*$ | diameter of largest solidified droplet at any X |
| $D$ | diameter of metal stream |
| $\dot{D}$ | deposition rate |
| $f_s$ | fraction solid |
| $F$ | force |
| $g$ | acceleration due to gravity |
| GMR | ratio of gas:metal mass flow rates |
| $h_g$ | convective heat transfer coefficient (gas) |
| $H$ | enthalpy |
| $H_f$ | latent heat of fusion |
| $H_{FR}$ | heat in the freezing range of the alloy = $H_f + C_P \Delta T_f$ |
| $H_{gas}$ | heat extracted by the gas |
| $H_{rem}$ | heat to be removed from the metal after deposition |
| $H_{spray}$ | enthalpy of the spray |
| IPP | independent process parameter (directly controlled) |
| $K$ | thermal conductivity |
| $K_L$ | constant in Lubanska's Equation, Eq. (1) |
| %L | volume % of liquid |
| $m$ | mass of droplet |
| $m_L$ | exponent in Lubanska equation, Eq. (1) |
| $P(d_i)$ | fraction of droplets of diameter $d_i$ |
| Pr | Prandtl number = $v/\alpha$ |
| $Q$ | heat flux |
| $r$ | radial distance |
| Re | Reynolds number = $Vd/v$ |
| $t$ | time |
| $t_f$ | local solidification time |
| $T$ | temperature |
| $\dot{T}$ | cooling rate |
| $\Delta T_f$ | freezing range of alloy = $(T_L - T_s)$ |
| $\Delta T_n$ | degree of undercooling |
| $\Delta T_s$ | degree of superheat |
| $V$ | velocity |

| | |
|---|---|
| We | Weber number |
| $x$ | distance along axis perpendicular to spray axis |
| $\partial x$ | splat thickness |
| $X$ | flight distance |
| $z$ | growth axis, thickness |
| $Z$ | deposit thickness |
| $\dot{Z}$ | deposit growth rate = $dZ/dt$ |
| $\dot{Z}_0$ | deposit growth rate at spray axis, $r=0$ |
| $\alpha$ | thermal diffusivity |
| $\beta$ | radial distribution coefficient; Eq. (6) |
| $\beta_s$ | solidification shrinkage |
| $\gamma$ | surface energy |
| $\eta$ | dimensionless thickness = $z/L$ |
| $\mu$ | viscocity |
| $\nu$ | kinematic viscosity |
| $\Pi_p$ | packing efficiency |
| $\Pi_s$ | sticking efficiency |
| $\Pi_t$ | target efficiency |
| $\rho$ | density |
| $\sigma$ | standard deviation of droplet size distribution |
| $\sigma$ | Stefan-Boltzman constant |
| $\omega$ | rotation speed |

Subscripts

| | |
|---|---|
| b | bottom surface of deposit |
| d | droplet |
| e | eutectic |
| g | gas |
| i | initial |
| L | liquidus |
| m | metal |
| n | nucleation |
| P | particle |
| r | relative |
| s | substrate |
| spray | in the spray |

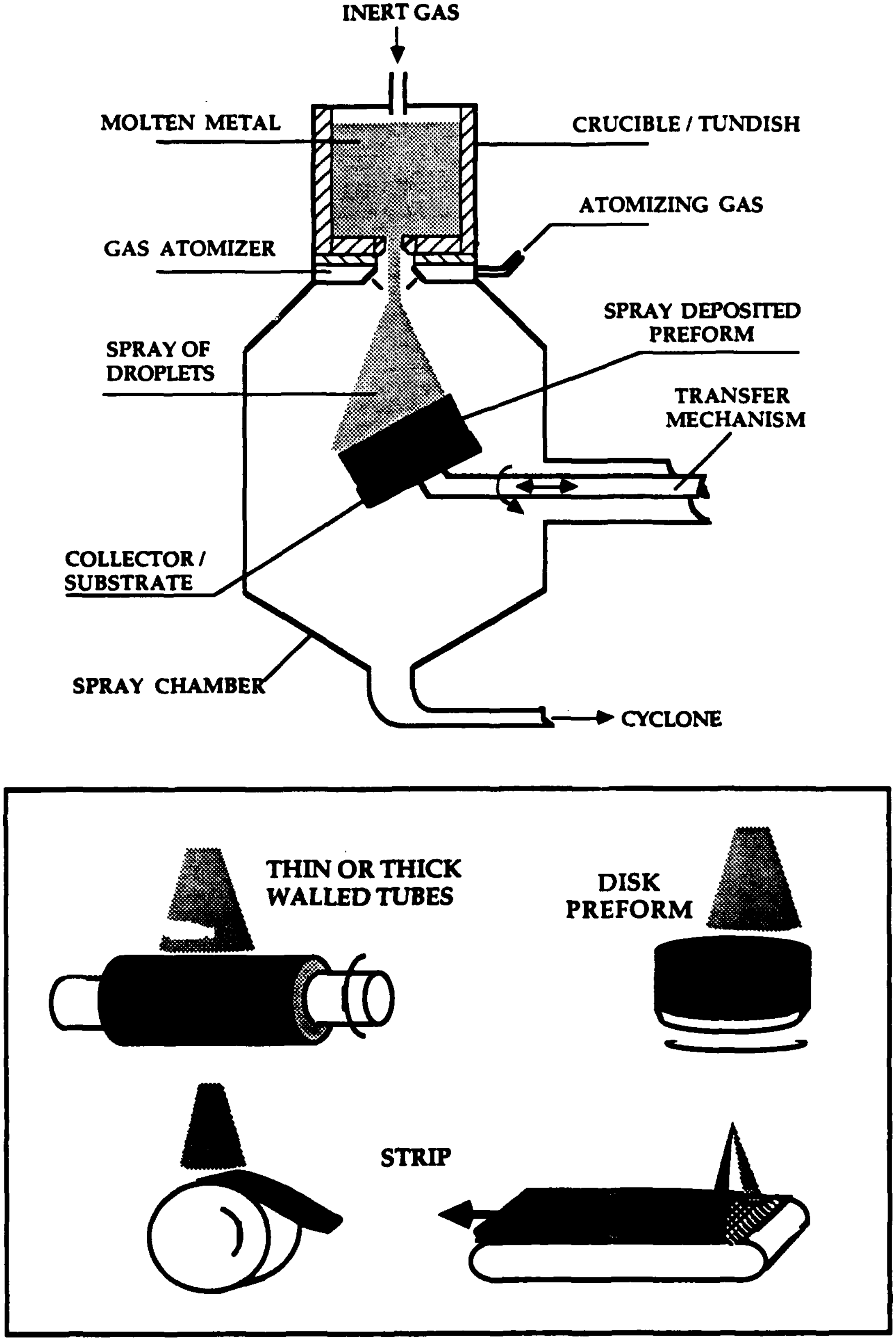
INERT GAS
MOLTEN METAL
CRUCIBLE / TUNDISH
ATOMIZING GAS
GAS ATOMIZER
SPRAY DEPOSITED PREFORM
SPRAY OF DROPLETS
TRANSFER MECHANISM
COLLECTOR / SUBSTRATE
SPRAY CHAMBER
CYCLONE
THIN OR THICK WALLED TUBES
DISK PREFORM
STRIP

Fig. 1 Schematic of the Osprey process and various preform shapes produced by different substrate configurations and motion

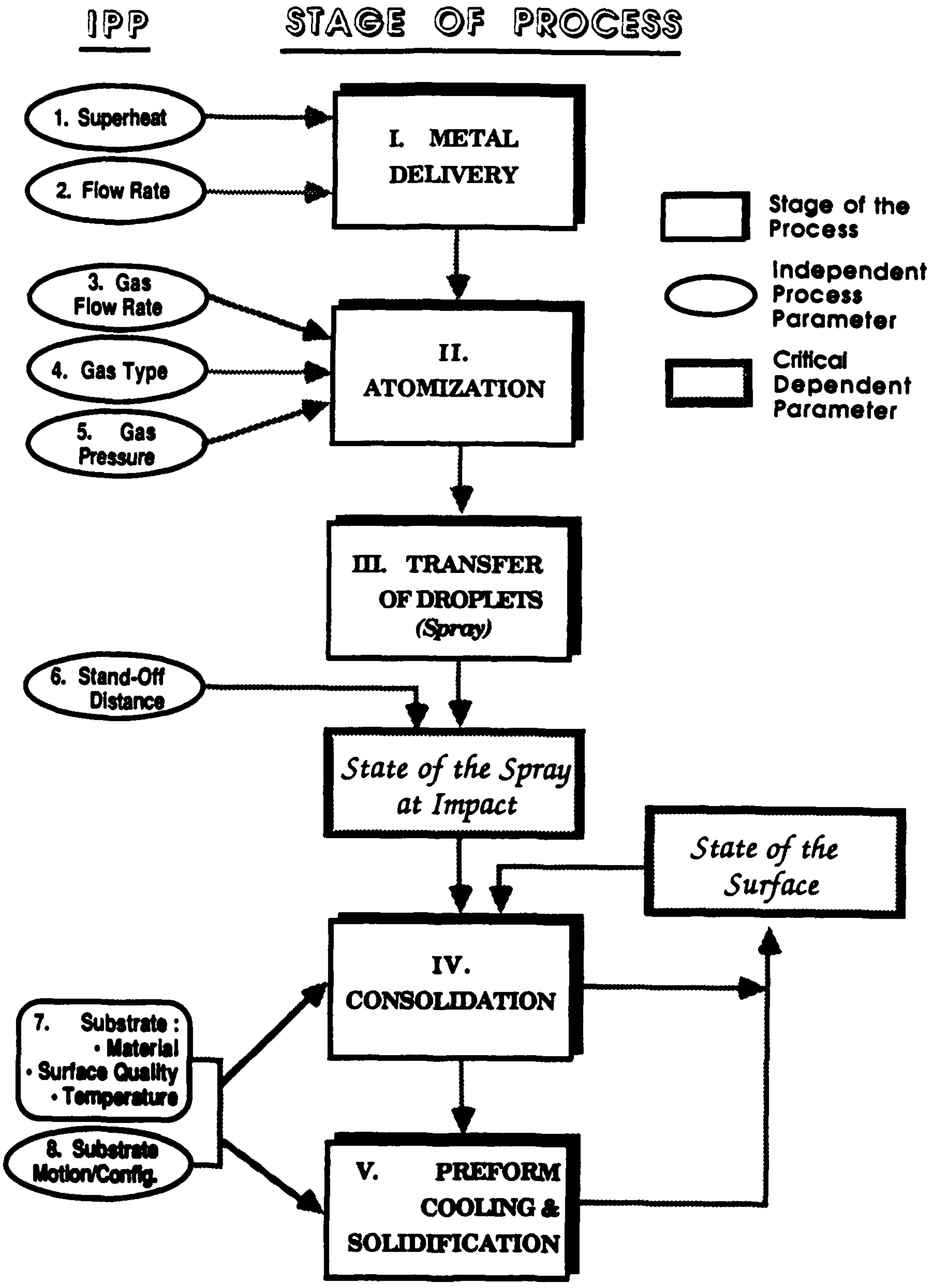
IPP
STAGE OF PROCESS
1. Superheat
2. Flow Rate
I. METAL DELIVERY
3. Gas Flow Rate
4. Gas Type
5. Gas Pressure
II. ATOMIZATION
III. TRANSFER OF DROPLETS (Spray)
6. Stand-Off Distance
State of the Spray at Impact
State of the Surface
IV. CONSOLIDATION
7. Substrate : • Material • Surface Quality • Temperature
8. Substrate Motion/Config.
V. PREFORM COOLING & SOLIDIFICATION
Stage of the Process
Independent Process Parameter
Critical Dependent Parameter

Fig. 2 Flow chart depicting independent process parameters at each intermediate stage in spray casting

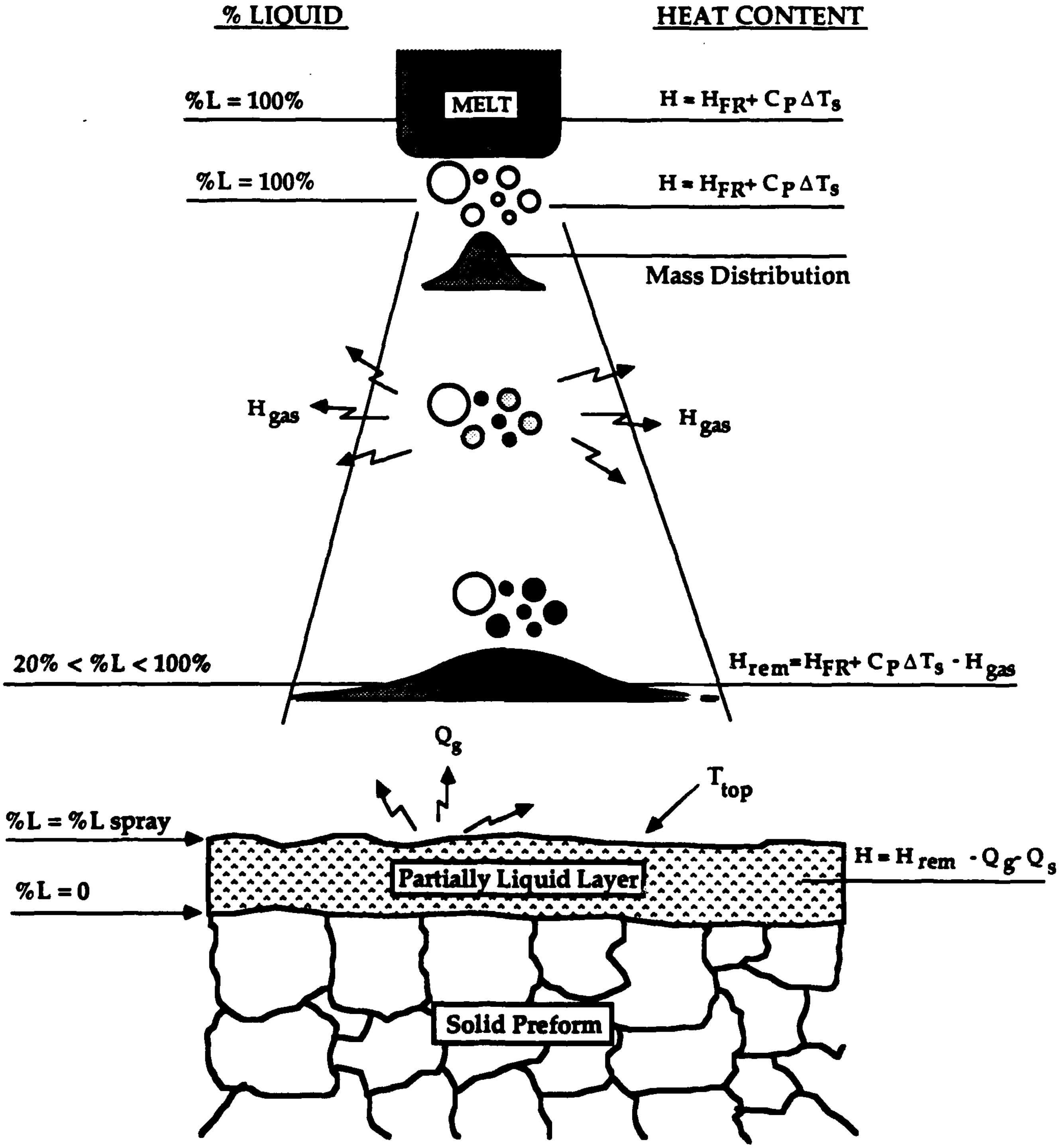
% LIQUID
HEAT CONTENT
%L = 100%
MELT
$H = H_{FR} + C_p \Delta T_s$
%L = 100%
$H = H_{FR} + C_p \Delta T_s$
Mass Distribution
$H_{gas}$
$H_{gas}$
20% < %L < 100%
$H_{rem} = H_{FR} + C_p \Delta T_s - H_{gas}$
$Q_g$
$T_{top}$
%L = %L spray
%L = 0
Partially Liquid Layer
$H = H_{rem} - Q_g - Q_s$
Solid Preform

Fig. 3 Schematic representation of spray casting showing the physical and thermal states of the spray and of the deposit

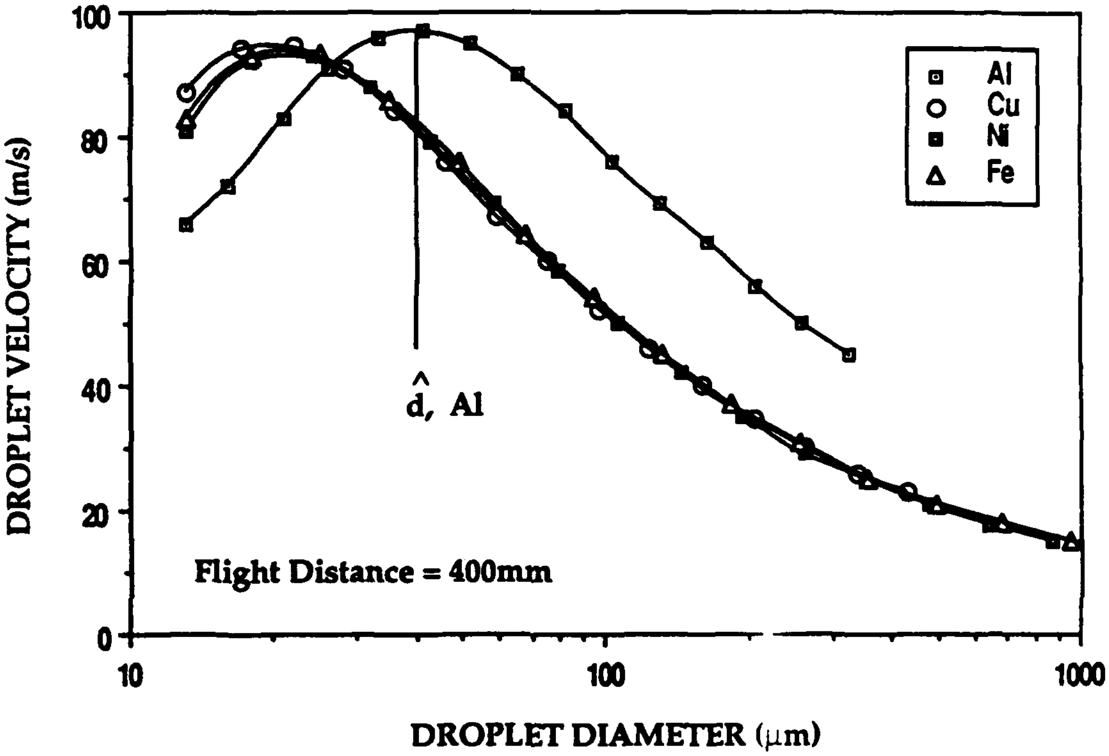

Fig. 4 : Predicted velocity of droplets prior to impact at X=400m

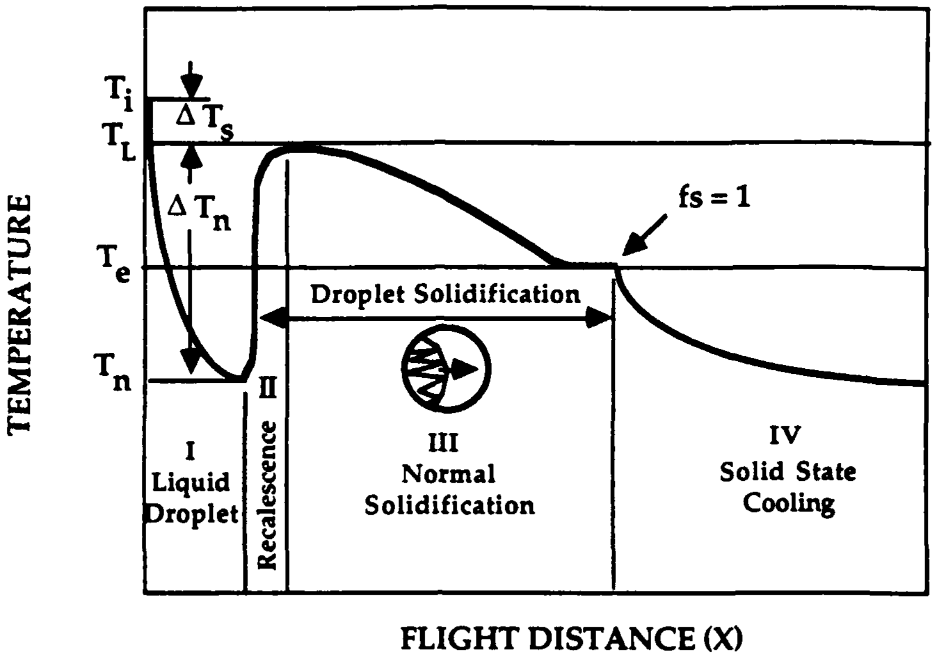
TEMPERATURE
$T_i$
$\Delta T_s$
$T_L$
$\Delta T_n$
$T_e$
$T_n$
fs = 1
Droplet Solidification
I
Liquid
Droplet
II
Recalescence
III
Normal
Solidification
IV
Solid State
Cooling
FLIGHT DISTANCE (X)

(a)

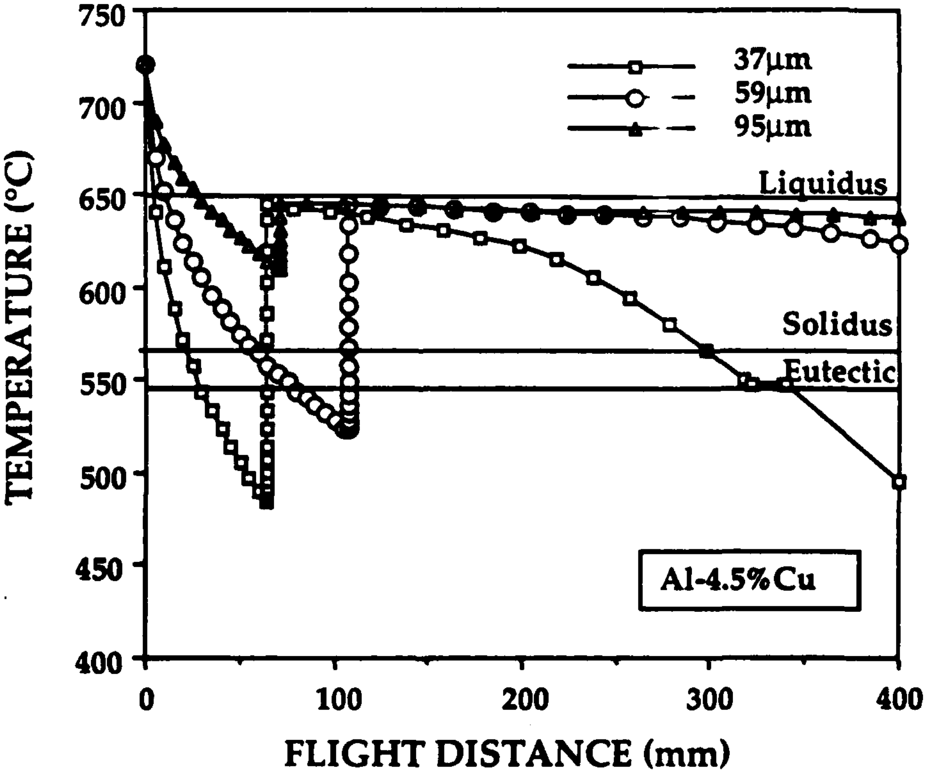

(b)

Fig. 5 (a) Schematic of droplet temperature and solidification in flight
(b) Predicted droplet temperature profile for three droplet diameters

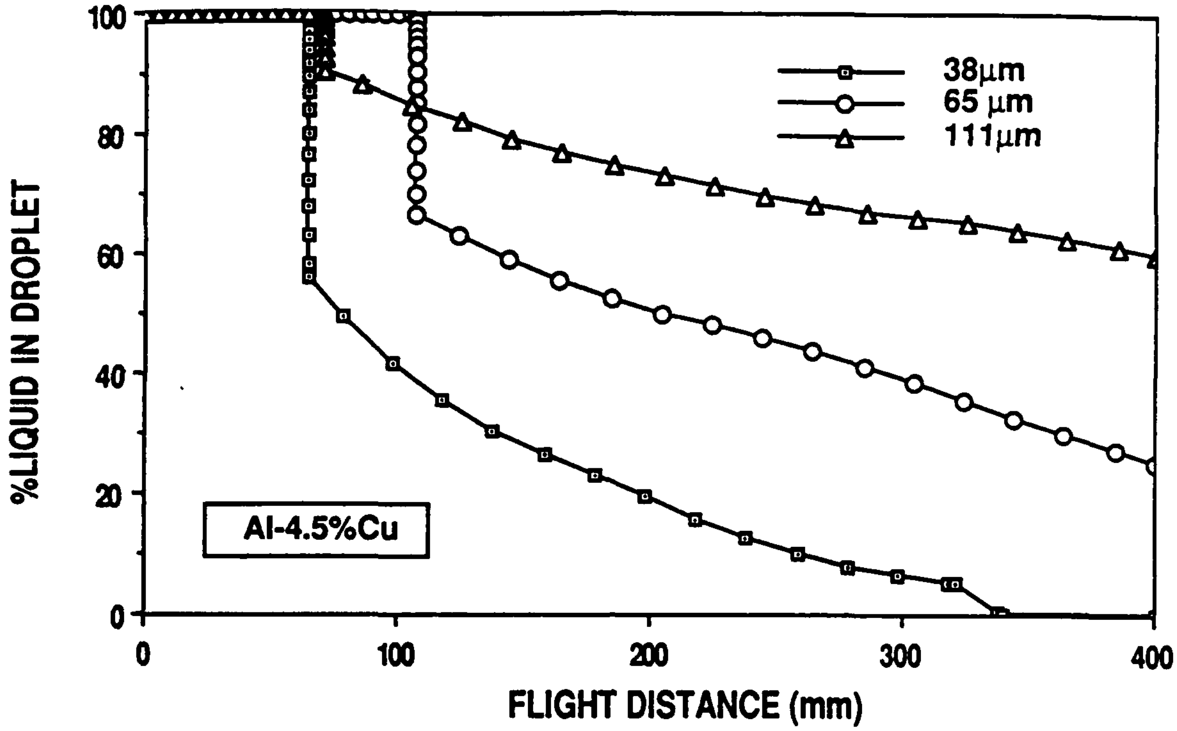

Fig. 6(a) Predicted solidification of Al-4.5%Cu droplets during flight

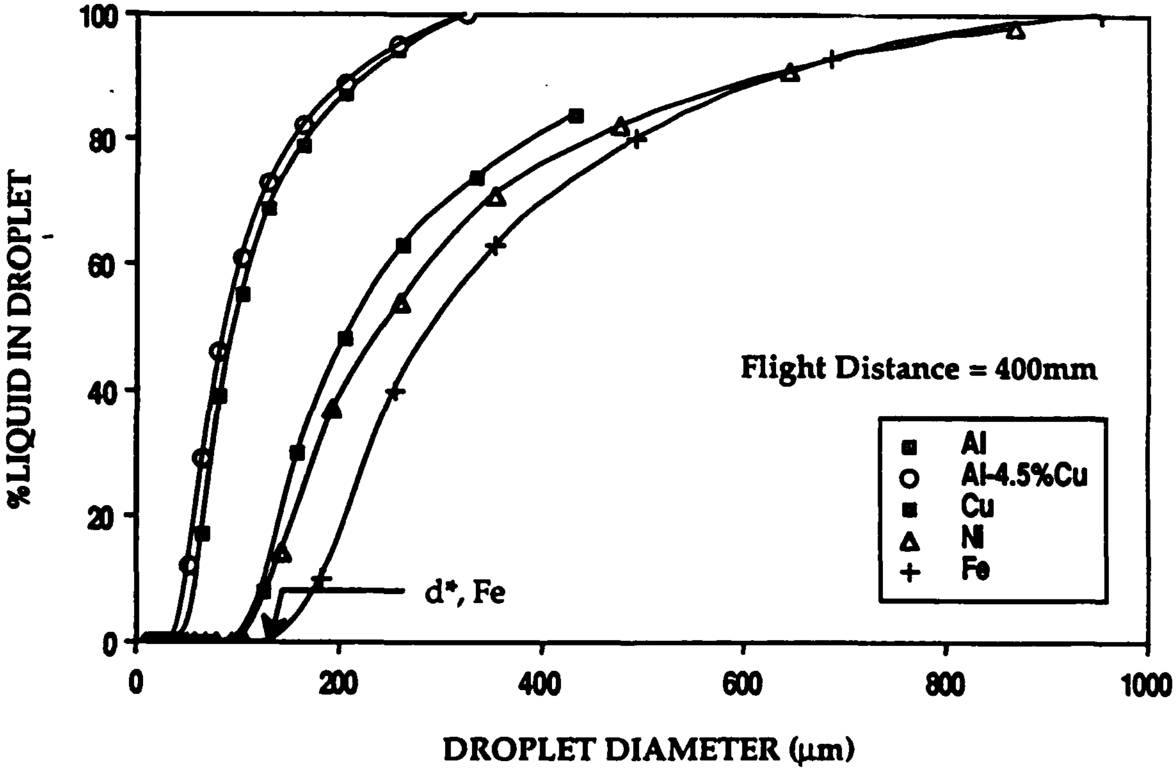

Fig. 6(b) : Extent of droplet solidification at X=400mm vs diameter for five alloys

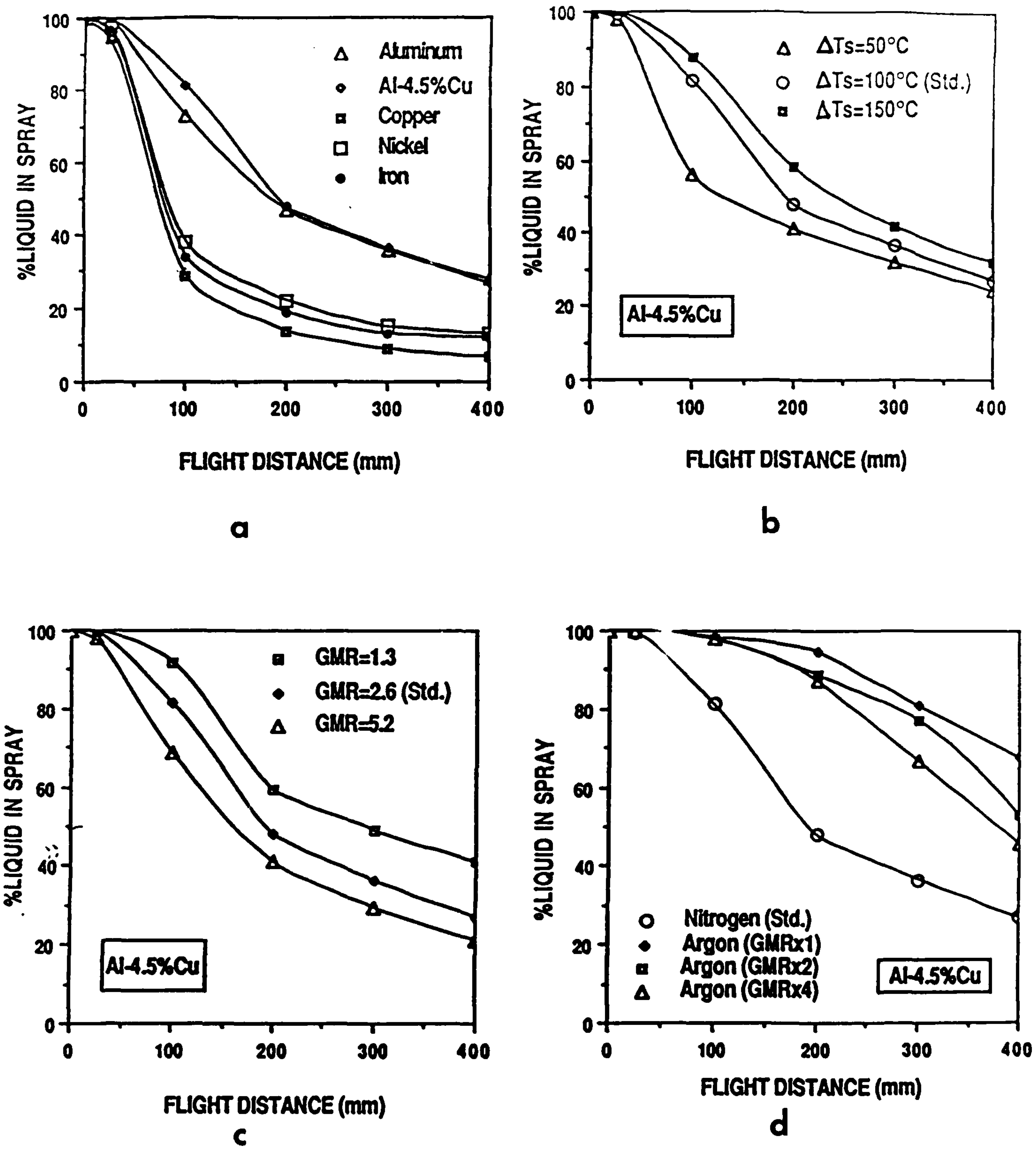

Fig. 7 Variation of the percentage of liquid in the spray with flight distance showing the effect of (a) material, (b) melt superheat, (c) gas : metal flow rate ratio, and (d) type of atomizing gas employed

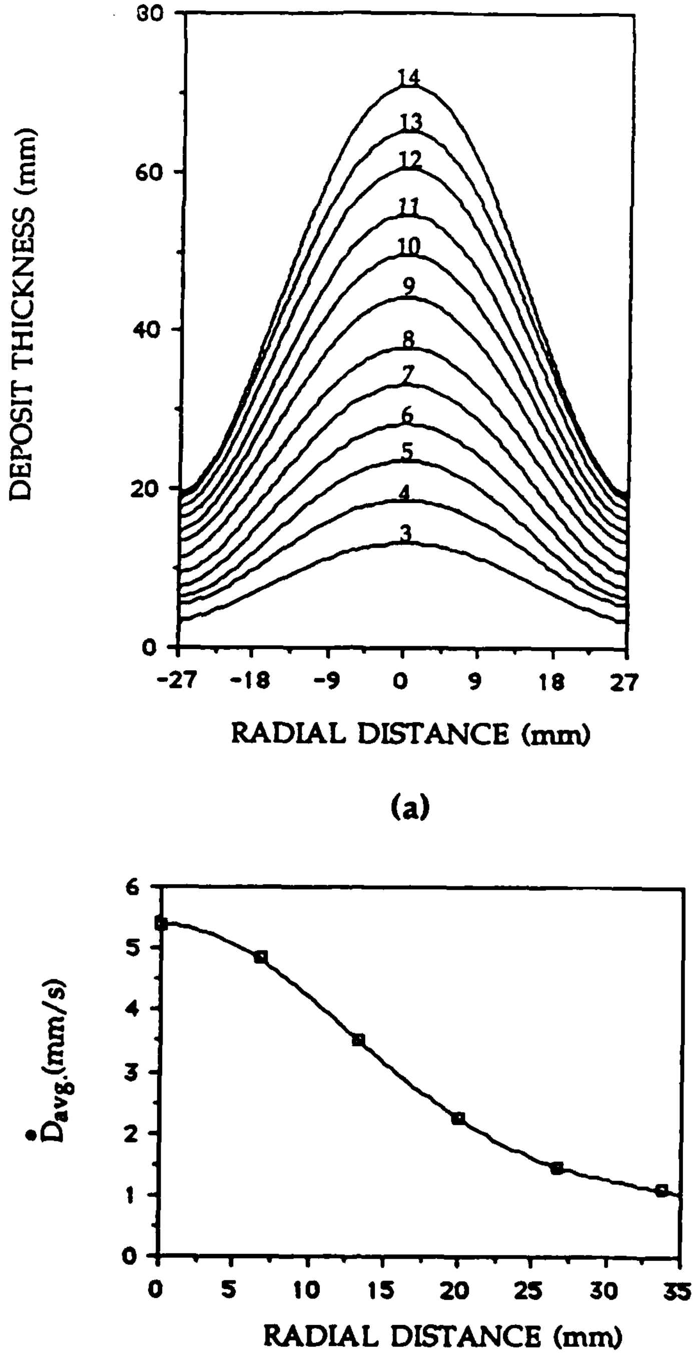

(a)

(b)

Fig. 8 (a) Thickness profiles at different time intervals (sec.) from the start of deposition, and

(b) dependence of time averaged deposition rate on distance from the axis of the spray.

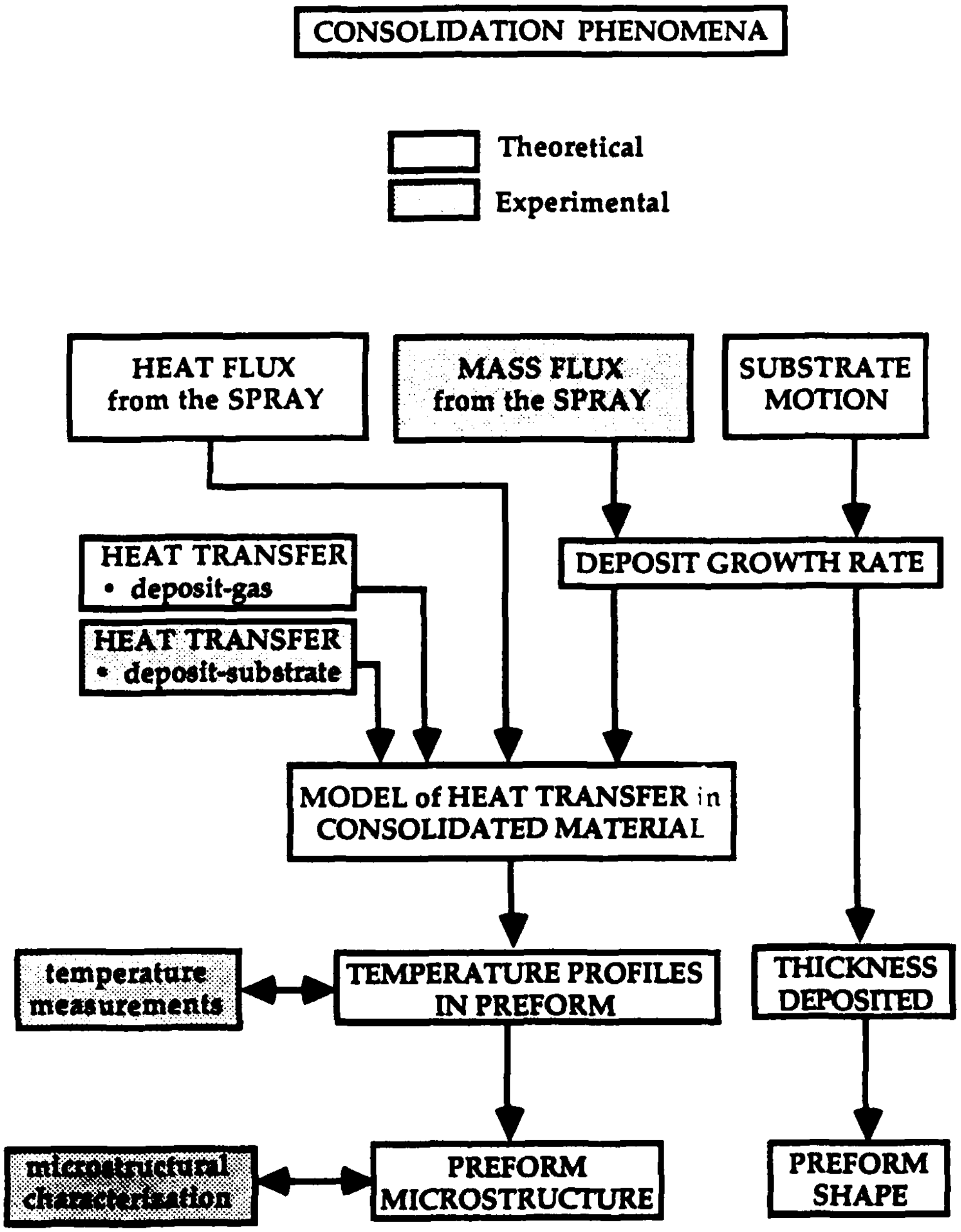
CONSOLIDATION PHENOMENA
Theoretical
Experimental
HEAT FLUX from the SPRAY
MASS FLUX from the SPRAY
SUBSTRATE MOTION
HEAT TRANSFER • deposit-gas
HEAT TRANSFER • deposit-substrate
DEPOSIT GROWTH RATE
MODEL of HEAT TRANSFER in CONSOLIDATED MATERIAL
temperature measurements
TEMPERATURE PROFILES IN PREFORM
THICKNESS DEPOSITED
microstructural characterization
PREFORM MICROSTRUCTURE
PREFORM SHAPE

Fig. 9 Flow chart depicting the approach adopted to determine preform microstructure and shape

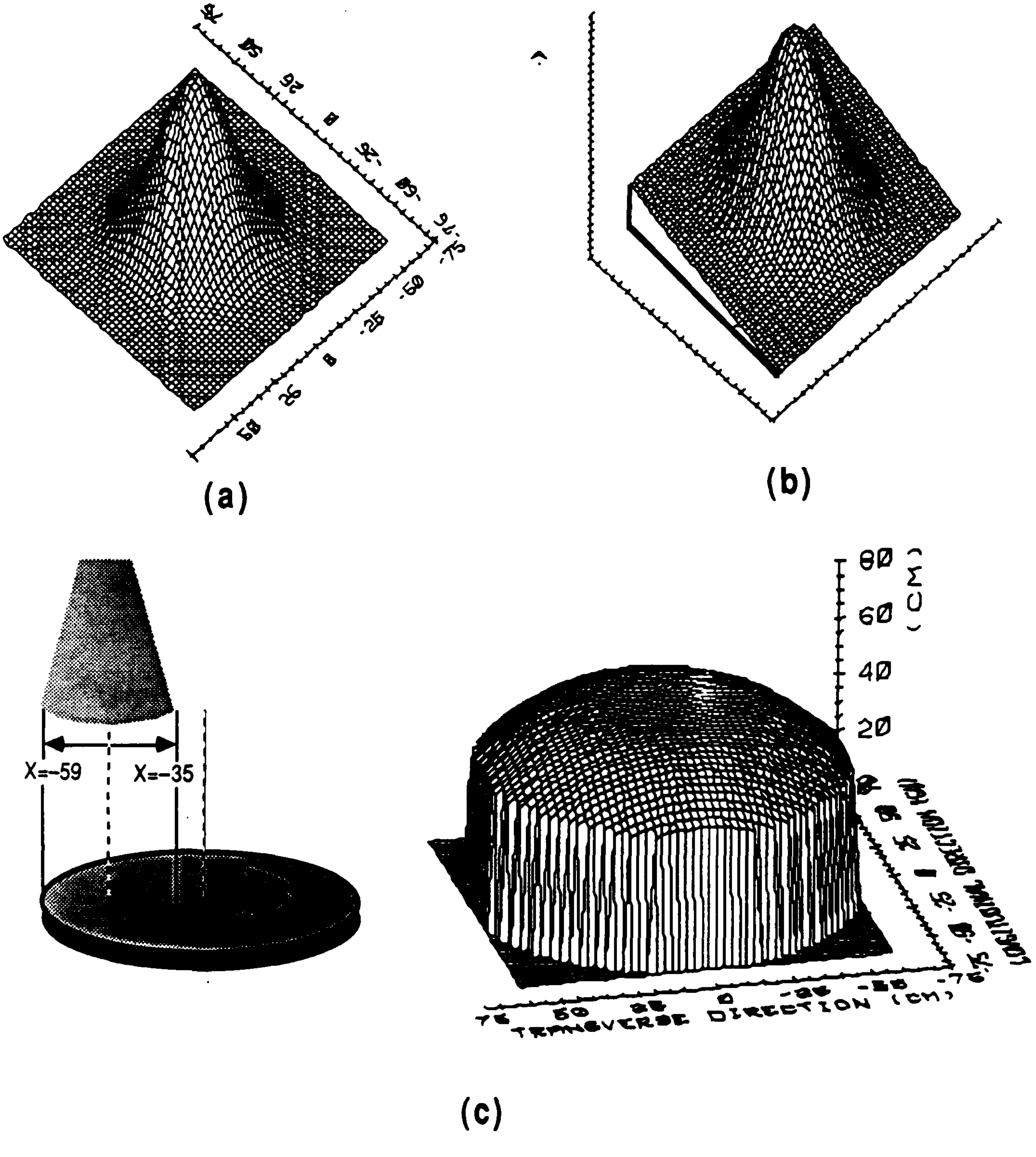

Fig. 10 Computed preform shapes/geometries produced by spray deposition
(a) deposit produced on horizontal, stationary substrate
(b) deposit produced on stationary substrate inclined to the spray axis
(c) disk preform produced by combined rotation and translation

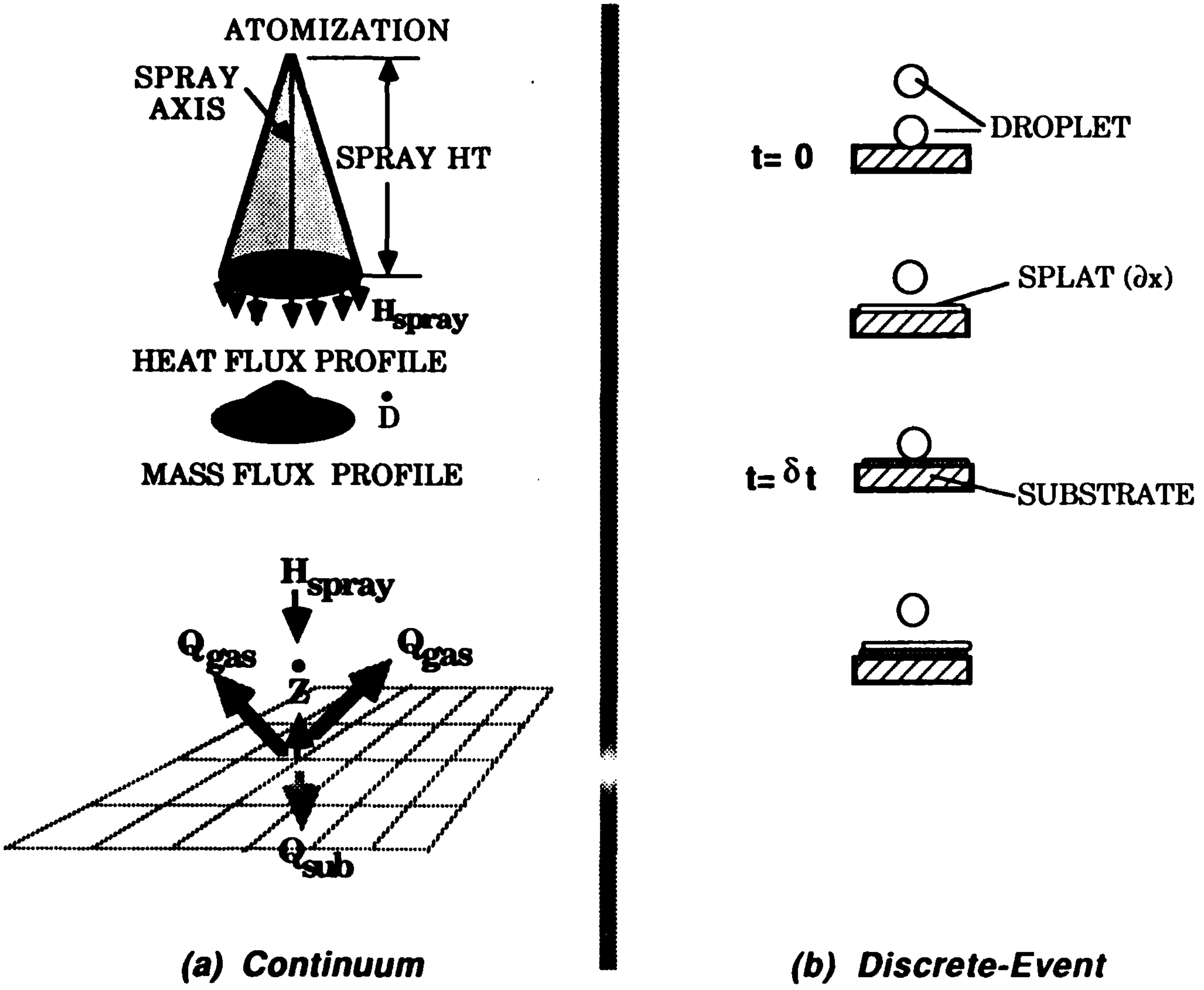
ATOMIZATION
SPRAY AXIS
SPRAY HT
$H_{spray}$
HEAT FLUX PROFILE
$\dot{D}$
MASS FLUX PROFILE
$H_{spray}$
$Q_{gas}$
$Q_{gas}$
Z
$Q_{sub}$
t= 0
DROPLET
SPLAT (∂x)
t= δt
SUBSTRATE

***(a) Continuum***

***(b) Discrete-Event***

Fig. 11 Schematic of the continuum and discrete-event approaches to model preform growth and solidification

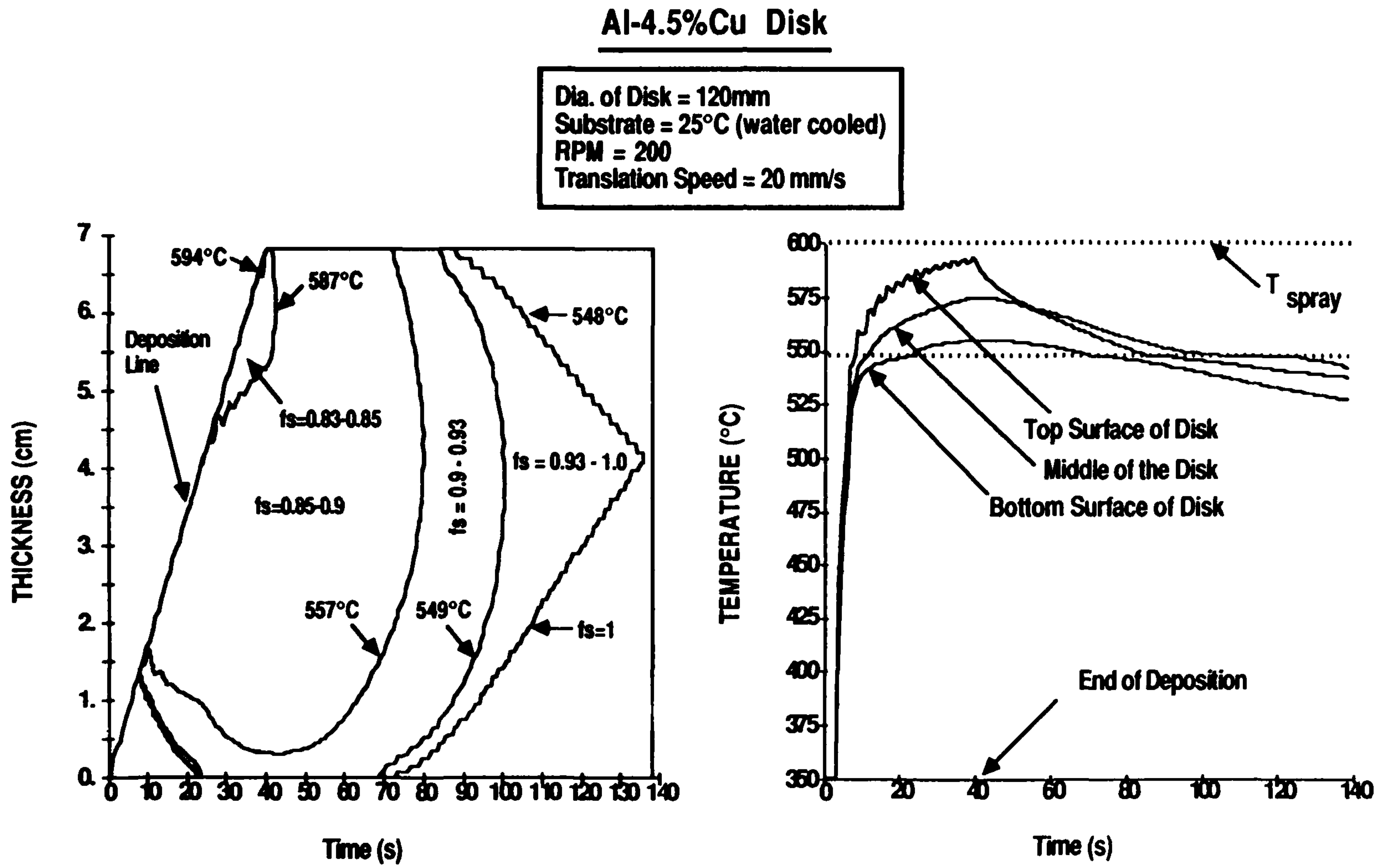

Fig. 12 (a) Predicted thermal profiles in a disk preform, and
(b) Predicted variation of temperature at the top, middle and bottom locations in the disk during spray deposition

Advances in Powder Metallurgy - 1989
Compiled by T.G.Gasbarre and W.F.Jandeska
Metal Powder Industries Federation, Princeton, NJ,
Vol. 2, p.161, 1989

# SPRAY CASTING OF HIGH-STRENGTH LOW-ALLOY STEELS

Daniel J. Schaeffler, Alan Lawley, and Diran Apelian

Department of Materials Engineering
Drexel University
Philadelphia, PA 19104, USA

## ABSTRACT

Osprey™ spray casting has been examined as a means of producing high-strength-low alloy (HSLA) steel. Preforms of HSLA-100, a low carbon bainitic, copper precipitation strengthened HSLA steel, were spray cast under differing conditions of superheat, atomizing gas (nitrogen) pressure, and preform cooling rate. Some of the spray cast material was subjected to thermomechanical treatments involving hot rolling and aging. Microstructure was characterized in terms of grain size, the degree of porosity, and microhardness. The primary constituent of the microstructure was coarse bainite, formed from relatively large austenite grains; these grains were subsequently reduced by thermomechanical processing. In the as-sprayed condition, fine copper-rich precipitates about 50 nm in diameter were present. Differences in the levels of oxygen and nitrogen with respect to location in the preform are the result of the overall combination of spray processing conditions.

## INTRODUCTION

Advances in technology are usually driven by savings in one form or another. For example, in the 1940's, the steel industry was looking for a new type of steel to replace C-Mn steels used for structural applications. Out of this need came the development of high-strength, low-alloy steels (HSLA), with improved properties at lower cost, compared to C-Mn steels. In the past decade, materials technology has been moving towards processes which result in products in final shape, or close to final shape (net or near-net-shape), without the need for additional forming operations.

This study was undertaken to assess the viability of fabricating a high-strength, low-alloy steel by means of a near-net-shape manufacturing process. Specifically, HSLA-100, a copper precipitation strengthened high-strength, low-alloy steel was spray cast via the Osprey™ process. Although other alloys such as stainless steels [1,2], tool steels [2], low alloy steels [2], aluminum alloys [3,4], copper alloys [5], and nickel-based superalloys [5,6,7] have been manufactured by the Osprey™ process, this study represents the first attempt to produce a high-strength, low-alloy steel in this way. The effect of varying selected spray casting process parameters on microstructural characteristics and mechanical properties was investigated.

## HSLA STEELS: PROCESSING, MICROSTRUCTURE AND PROPERTIES

High-strength low-alloy (HSLA) steels exhibit yield strengths in the range 300 to 700 MPa in the as-rolled condition. Primary objectives in HSLA steel technology are to: (i) improve strength, toughness, and weldability, (ii) lower the overall cost of production by employing energy efficient processing techniques and eliminate the need for additional heat treatment procedures, and (iii) limit the amount of alloying additions through microalloying [8]. These goals can be met by using a low-carbon steel which increases weldability and toughness [9]. By appropriate microalloying additions, strength and toughness can be further increased.

HSLA-100 is a low-carbon bainitic, microalloyed copper precipitation strengthened steel with a yield strength of 100 ksi [9,10,11,12]. Developed for the United States Navy, it is a modified HSLA-80, which is the Navy's designation for ASTM A710 steel [10,12,13,14,15,16]. The thrust behind this program was to produce a high strength material which would be easier to fabricate than existing naval steels such as HY-80 and HY-100, and which would permit welding without a preheat [10,15]. A typical fabrication route for the production of HSLA-100 consists of electric furnace melting, vacuum degassing, calcium treating, ingot casting, rolling into plate form, austenitization, quenching, and aging [10].

Each of the alloying additions in HSLA-100 has a specific role. Molybdenum and chromium increase the bainitic hardenability by delaying the onset of proeutectoid ferrite formation [9]. Additionally, they retard copper precipitation during the cooling of the steel from the austenite range [9]. Niobium functions mainly as a grain refiner [14,15] with only minor contributions in precipitation strengthening in the form of niobium carbonitride (Nb(CN)) [11,14]. The bulk of the precipitation strengthening comes from the precipitation of copper during the aging treatment [9,10,15]. Nickel is added to prevent any hot shortness associated with the copper addition [10,17]. Nickel also increases the hardenability and toughness of the steel [13]. Aluminum is present for the purposes of deoxidation and grain refinement [12,16].

The role of copper as an alloying element is paramount since it is the major contributor to strength by precipitation hardening in HSLA-100 steel. Upon aging, coherent BCC clusters of copper form first [18,19,20]. At peak strength, these clusters have a mean diameter of 2.4 nm [19] and have a copper content of about 50 a/o. [20]. Upon further aging, these clusters transform into non-coherent FCC ε–Cu [18]. This transformation occurs when the clusters have a diameter of approximately 4 to 5 nm. [19,20] As the aging process continues, the precipitates become richer in copper and their lattice parameter decreases [14] Typical ε–Cu precipitate diameters range from 10-50 nm. [14] The larger precipitates are oblong in shape, while the smaller ones are more equiaxed [14].

It is not possible to study the initial stages of copper precipitation by electron microscopy because of the coherency of the BCC clusters with the matrix lattice [19]. Only after peak strength is reached can the precipitates (now ε–Cu) be studied by electron microscopy.

Normally HSLA-100 is used in the overaged condition [21]. Although the yield and tensile strength decrease after peak aging, toughness increases dramatically during overaging. Thus, it is necessary to determine the optimal aging temperature for this alloy. The peak aging temperature is 455°C (850°F), but the optimal aging temperature is found to be 621°C (1150°F). [10]

In ingot metallurgy, the as-cast HSLA-100 steel is rolled into plate, aged, and then formed into final shape. This is a labor and time-intensive process. In keeping with the goals of HSLA steel technology, new methods must be examined in order to lower fabrication costs. One approach is to employ a near-net-shape manufacturing technique with a concomitant reduction in processing steps, and hence cost.

An example of a near-net-shape manufacturing technique is the Osprey™ spray forming process (Figure 1). [1,2,5,22] Spray forming in the Osprey™ mode usually produces a fine-grain equiaxed microstructure, no macrosegregation, limited porosity, and improved mechanical properties. Apart from these intrinsic benefits, it should be possible to eliminate the costly rolling processes characteristic of ingot metallurgy.

In the Osprey™ spray forming process, a stream of molten metal droplets is produced by the atomization of a liquid stream using high velocity gas jets. The droplets are directed toward a moving substrate where they consolidate and solidify. The motion of the collector determines the shape of the preform produced. Variables that may be altered in this process include "internal" variables such as atomizing gas pressure, melt superheat and nozzle diameter, and one "external" variable -- the cooling rate of the as-sprayed product.

## EXPERIMENTAL

Five heats of HSLA-100 were prepared using the Osprey™ spray forming facility at Drexel University. Approximately 11.4 kg (25 lbs.) of feedstock, in the form of bars 25.4 mm x 25.4 mm x 305 mm (1"x1"x12") were cut from HSLA-100 steel plate supplied by the David Taylor Research Center. The bars were melted in an alumina crucible under a protective nitrogen cover; melting time was less than 30 minutes. The melt was given a superheat of 50-100 °C and atomized with nitrogen gas at a pressure of either 0.9 or 1.0 MPa (9 or 10 bar). The gas-to-metal flow ratio varied from 1 to 1.3 and the nozzle diameter was kept constant at 4.5 mm. For deposition, a ceramic substrate was used, rotating at 25.1 radians per second (240 RPM). Deposition was completed within one minute after the start of spraying. Four of the preforms were air cooled in the chamber; the fifth preform was quenched into water. The experimental matrix used is shown in Table I.

Preforms were sectioned for metallographic examination and for chemical analysis. The techniques used for microstructural characterization were optical microscopy, scanning electron microscopy, transmission electron microscopy, and quantitative image analysis. Microhardness was also determined on sectioned preforms.

Samples for transmission electron microscopy were prepared by grinding thin sheets of the HSLA-100 steel down to approximately 100μm. Discs approximately 3 mm in diameter were then

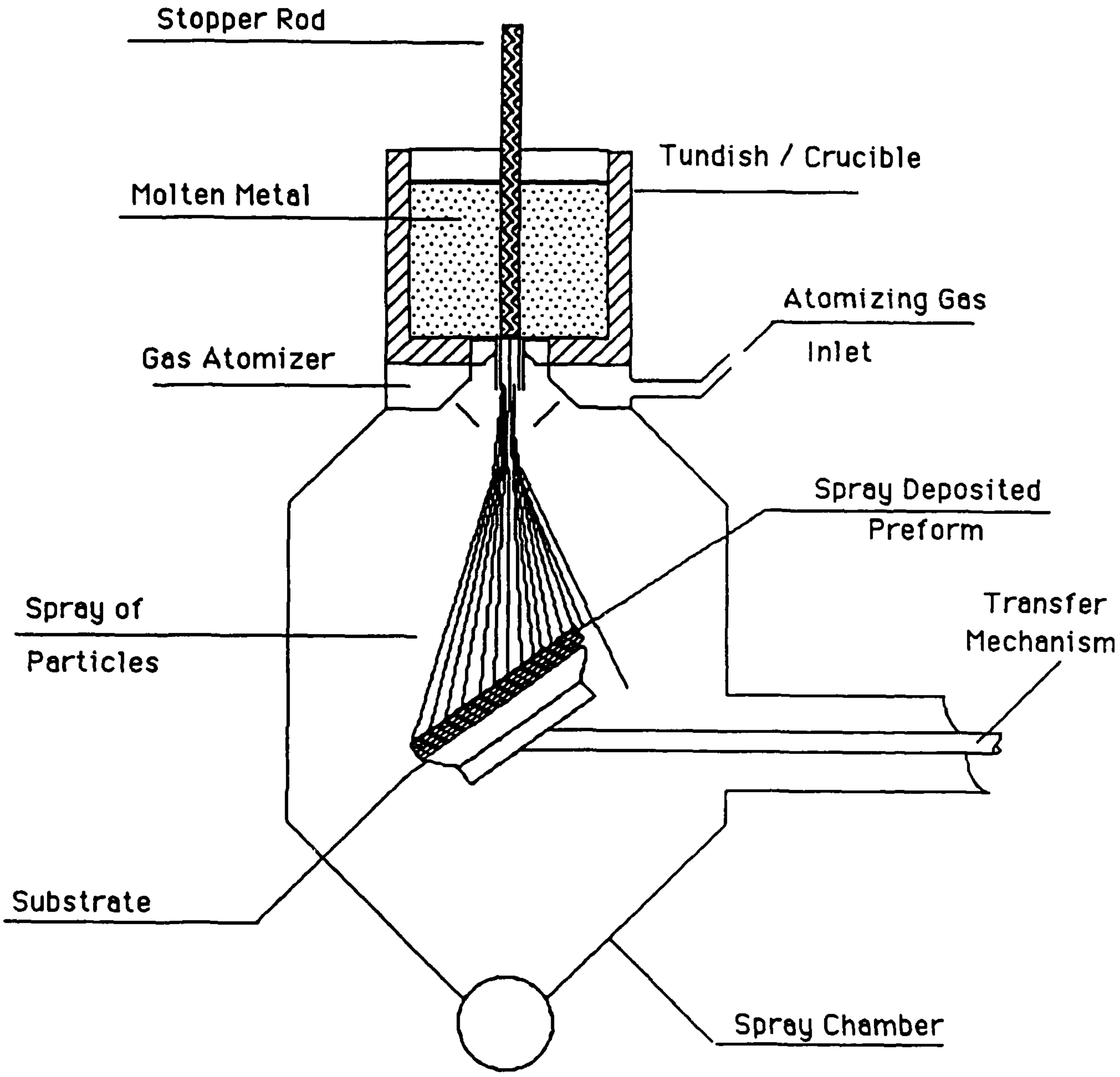
Stopper Rod
Tundish / Crucible
Molten Metal
Atomizing Gas
Inlet
Gas Atomizer
Spray Deposited
Preform
Transfer
Mechanism
Spray of
Particles
Substrate
Spray Chamber

Figure 1. Schematic of the Osprey™ Process.

TABLE I: EXPERIMENTAL MATRIX

| | |
|---|---|
| RUN 1 | 0.9 MPa<br>150 mm DIA. SUBSTRATE |
| RUN 2 | 0.9 MPa<br>150 mm DIA. SUBSTRATE |
| RUN 3 | 0.9 MPa<br>120 mm DIA. SUBSTRATE |
| RUN 4 | 1.0 MPa<br>120 mm DIA. SUBSTRATE |
| RUN 5 | 0.9 MPa<br>WATER QUENCH PREFORM<br>120 mm DIA. SUBSTRATE |

mechanically punched from the sheet. These discs were then thinned to electron transparency in a jet electropolisher using a solution of 33% nitric acid and 67% methanol at a temperature of less than -37°C (-35°F). The voltage was approximately 25 volts.

Because of the large grain size in the preforms, the effect of subsequent thermomechanical processing was examined. In particular, selected preforms were hot rolled and aged. Samples, either 50.8 mm x 50.8 mm x 25.4 mm (2"x2"x1") thick or 50.8 mm x 25.4 mm x 25.4 mm (2"x1"x1") thick, were rolled down to 12.7 mm (0.5") thick in 5 to 6 passes, following the schedule in Table II. The 50.8 mm x 50.8 mm x 25.4 mm samples (runs 2, 3, and 4) were rolled parallel to the spray axis, while the 50.8 mm x 25.4 mm x 25.4 mm sample (run 1) was rolled perpendicular to the spray axis. Two samples each from runs 2, 3, and 4 were aged at 621°C (1150°F) for 1 hour. Porosity and grain size were characterized and microhardness data were taken.

## RESULTS

In runs 1, 2, 4, and 5, a boron nitride stopper rod was used to retain the metal in the crucible until the desired superheat was reached. In run 3 an HSLA-100 "button" measuring 24.5 mm diameter by 7 mm thick was used. The geometry of the melting unit is such that the button is the last part of the charge to melt. Previous work [23] has shown that a button thickness of 7 mm produces a superheat in the range of 50-100 °C.

Superheat was the most difficult parameter to control. A Pt-6%Rh / Pt-30%Rh thermocouple was shielded from the melt by either an alumina or mullite protective sheath. In runs 1, 2, and 3, the sheath broke at the melting temperature (between 1470°C and 1505°C) and the superheat was estimated by extrapolating the time vs. temperature curve for the charge as it was approaching the melting temperature. In runs 4 and 5, the sheath did not break, and the actual spraying temperature was measured. Run 4 was sprayed at 1620°C, and run 5 was sprayed at 1550°C. Cross sections of the preforms from runs 3 and 4 are shown in Figure 2.

Although the degree of superheat was not measured, the spray in the first preform (run 1) was too hot. Qualitatively, the spray exhibited a bright yellow color. The macrostructure bore this out in the form of a large cavity (approximately 25 mm diameter) slightly above the center of the deposit; this void in run 1 is attributed to hot tearing. In contrast, however, the bottom third of the preform was essentially devoid of macroporosity. In runs 2, 3, 4, and 5 no macroporosity was evident. A composite of the porosity data, as measured by optical image analysis, are shown in Figure 3. It is evident that the highest level of porosity exists at the base and edges of the preform.

In the as-sprayed preforms which were allowed to cool slowly in the chamber, the prior austenitic grain size varied from approximately 100 to 500 μm (ASTM 3.5 to -1). This variation depended more on location in the preform than on experimental conditions. Representative microstructures are shown in Figures 4 through 7. A composite of grain size vs. position in the preform is given in Figure 8.

Composite microhardness data for the as-sprayed condition are shown in Figure 9. The hardness level is approximately 300 kgf/mm$^2$, irrespective of location in the cross section of the preform. The equivalent Rockwell A hardness is about 65, or Rockwell C 30. The corresponding tensile strength is about 930 MPa (135 ksi). [24]

Transmission electron microscopy revealed many fine precipitates in the as-sprayed condition,

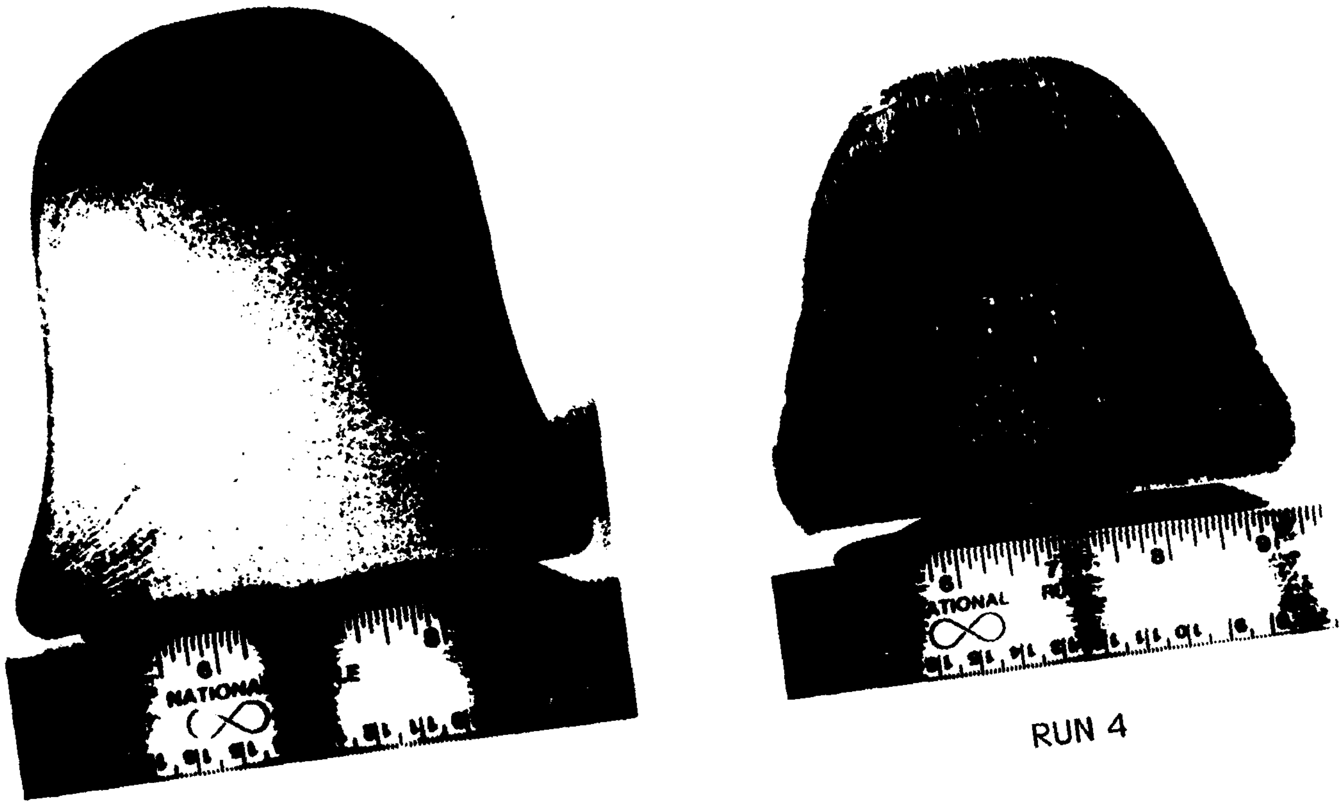

RUN 3

RUN 4

Figure 2. Cross sections of preforms.

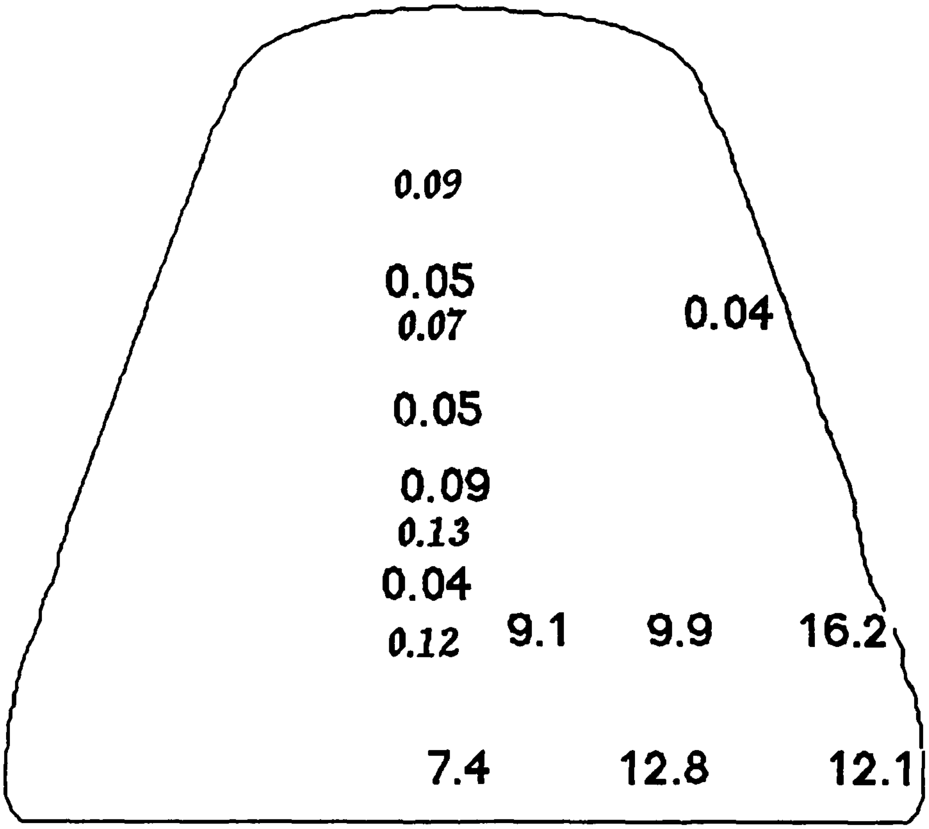
*0.09*
0.05
*0.07*
0.04
0.05
0.09
*0.13*
0.04
*0.12*
9.1
9.9
16.2
7.4
12.8
12.1

Figure 3. Porosity (%) vs. position in the preform
(Italicized text : measurement from face parallel to spray axis;
Plain text : measurement from face perpendicular to spray axis)

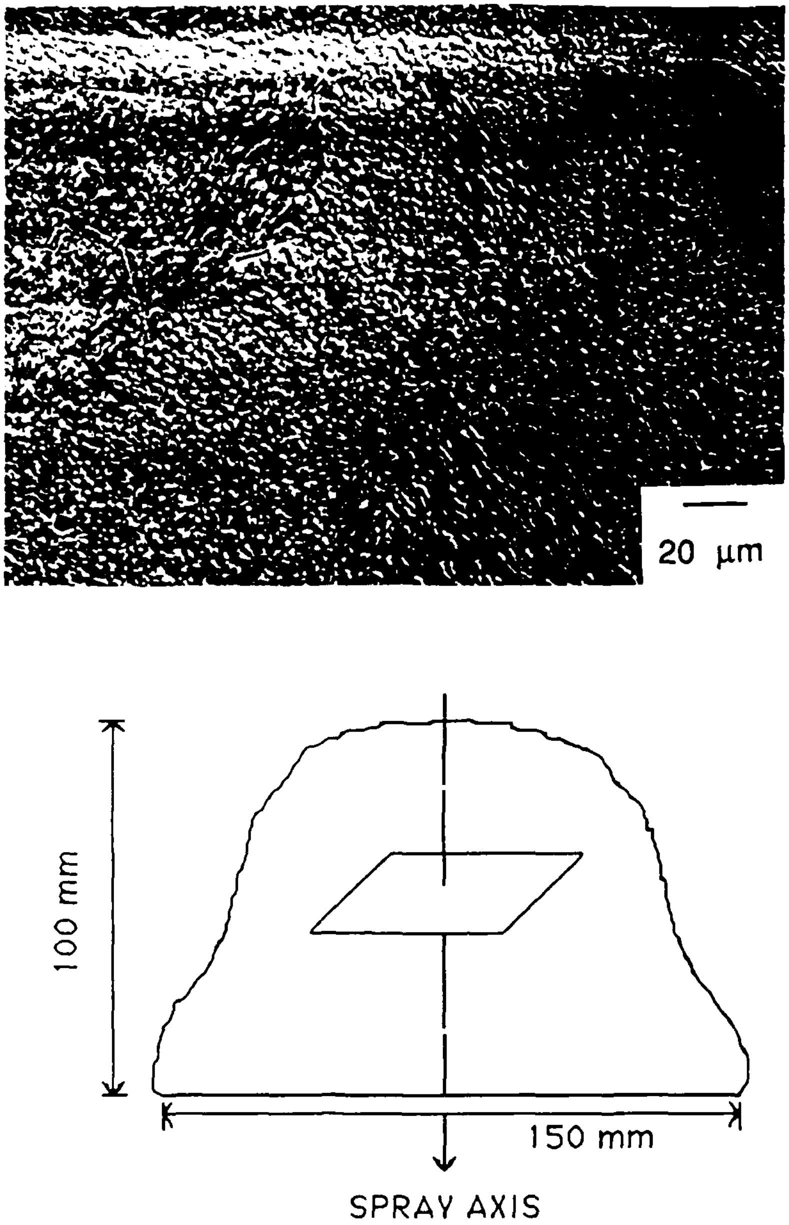
20 µm
100 mm
150 mm
SPRAY AXIS

Figure 4. SEM micrograph from run 2.

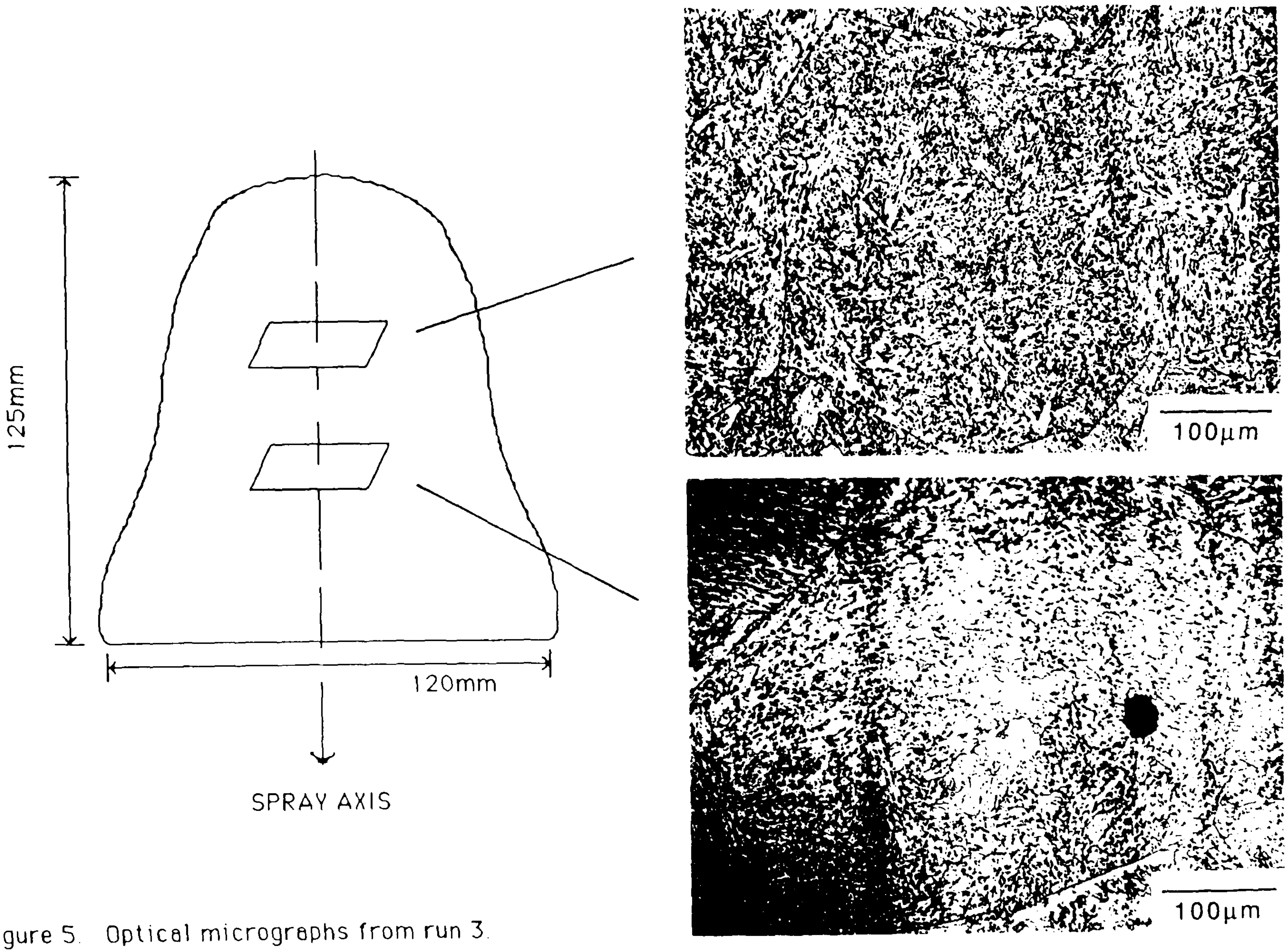
125mm
120mm
SPRAY AXIS
100μm
100μm

Figure 5. Optical micrographs from run 3.

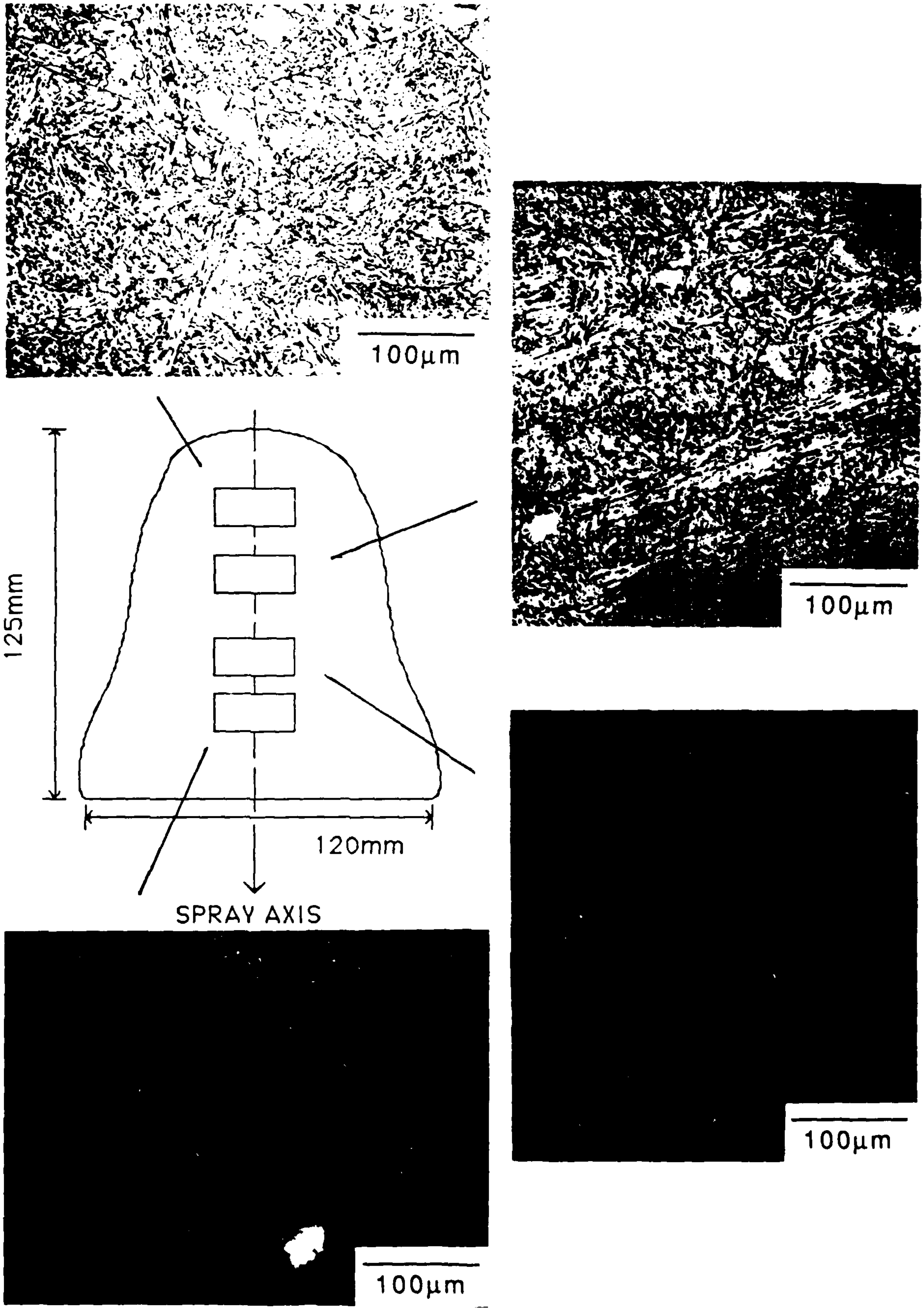
100µm
125mm
120mm
SPRAY AXIS
100µm
100µm
100µm

Figure 6. Optical micrographs from run 3

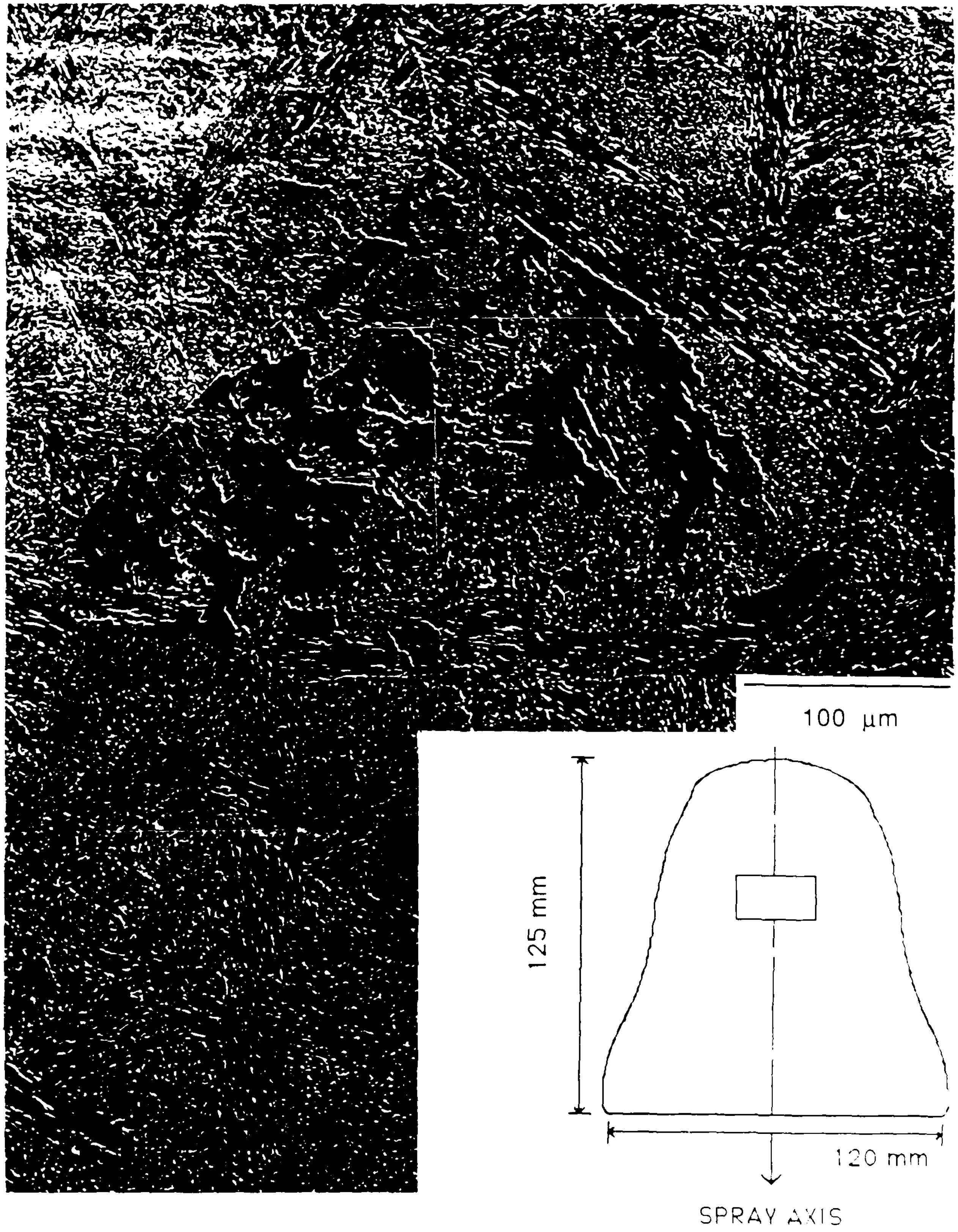
100 µm
125 mm
120 mm
SPRAY AXIS

Figure 7 SEM montage of a single grain from run 3.

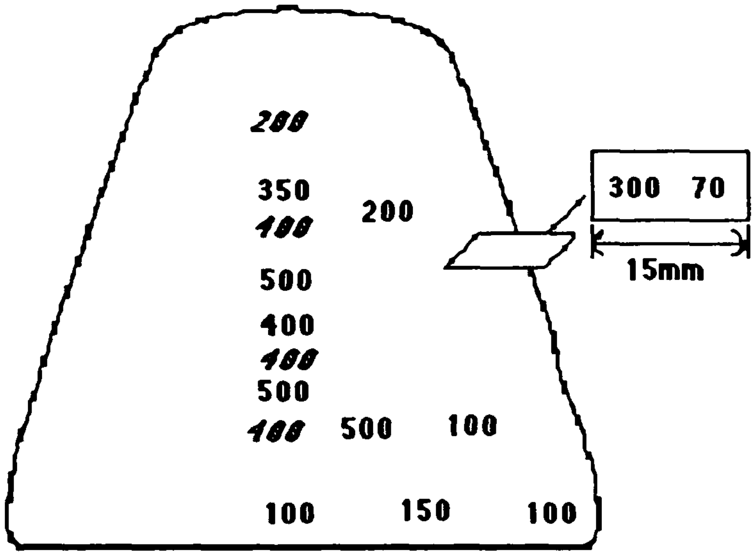

*200*
350
200
*400*
300
70
15mm
500
400
*400*
500
*400*
500
100
100
150
100

Figure 8. Grain size (μm) vs. position in the preform. (Italicized text : measurement from face parallel to spray axis; plain text : measurement from face perpendicular to spray axis.)

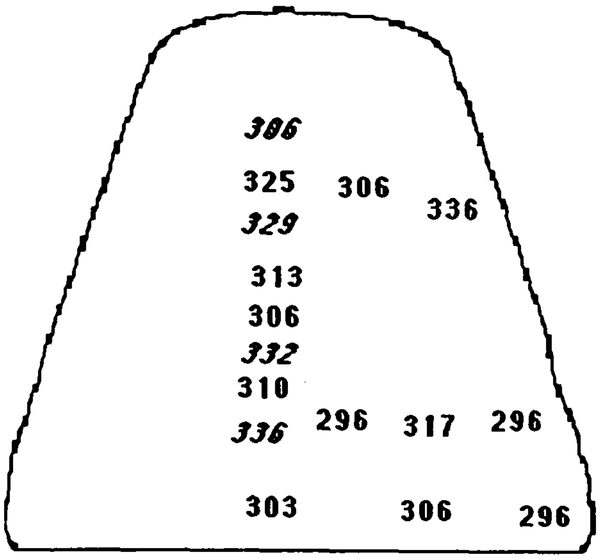

*306*
325
306
336
*329*
313
306
*332*
310
*336*
296
317
296
303
306
296

Figure 9. Vickers microhardness (kgf/mm$^2$) vs. position in the preform. (Italicized text : measurement from face parallel to spray axis; plain text : measurement from face perpendicular to spray axis.)

with diameters ranging from 35 to 70 nm. Typical micrographs with corresponding diffraction patterns from the center of the preform (run 3) parallel to the spray axis are given in Figures 10 and 11.

Since STEM was not used, it is impossible to identify the composition of the precipitates. By analyzing the diffraction patterns, however, it has been shown that the rings correspond to an FCC structure with a lattice parameter of approximately 0.365 nm. Pure copper has a lattice parameter of 0.361 nm.

The microstructure of the as-rolled and rolled+aged samples was also examined. Representative micrographs are given in Figure 12. It is seen that the grain size is reduced to approximately 100μm using the rolling schedule given in Table II.

Microhardness measurements were taken on preforms from runs 2, 3, and 4, in both the as-rolled and the rolled+aged conditions. These values were slightly lower than in the as-sprayed condition, ranging from 289 kgf/mm$^2$ to 330 kgf/mm$^2$ in the as-rolled condition, and from 303 kgf/mm$^2$ to 310 kgf/mm$^2$ after the rolling+aging treatment. In general, microhardness was higher parallel to the rolling direction than perpendicular to the rolling direction. To reiterate, however, the microhardness values centered around 300 kgf/mm$^2$ irrespective of the thermal history of the sample.

Porosity measurements were made by means of optical image analysis. In both the as-rolled and rolled+aged conditions, porosity varied between 0.1 and 0.75 on an area percentage basis.

## DISCUSSION

Interpretation of the observations and results is facilitated by first considering compositional changes during spray casting. Subsequently, we consider the effects of spray processing parameters on the microstructure and macrostructure of the preforms. Finally, the response of the spray cast HSLA preforms to thermomechanical processing is discussed.

### (a) *Composition*

Chemical analyses of the starting material and the spray cast preforms are given in Table III. These show that there is a decrease in the aluminum content from 0.03% in the feedstock to less than 0.01% in the preforms. Niobium also decreased from 0.03% to 0.01% in two of the runs. Since these elements are responsible for grain refinement, their absence in the preform contributed to the large grain size in the as-sprayed condition. In addition to the five runs, a charge was melted and allowed to solidify in the crucible. Table III shows there is a large decrease in the aluminum content at the bottom of the charge. It is postulated that the aluminum combined with the oxygen in the melt and rose to the top of the molten charge.

Another factor which may result in a large grain size is the slow cooling of the preform in the chamber. Quenching of the preform into water immediately after completion of the spray cycle gave a fine grain size at the edge of the preform. However, less than a centimeter inwards from the edge of the preform, a coarse grain size existed, Figure 13. A definite preferred bainitic lath orientation is observed in this structure.

Differences in the oxygen and nitrogen content from the bottom to the top of the preforms

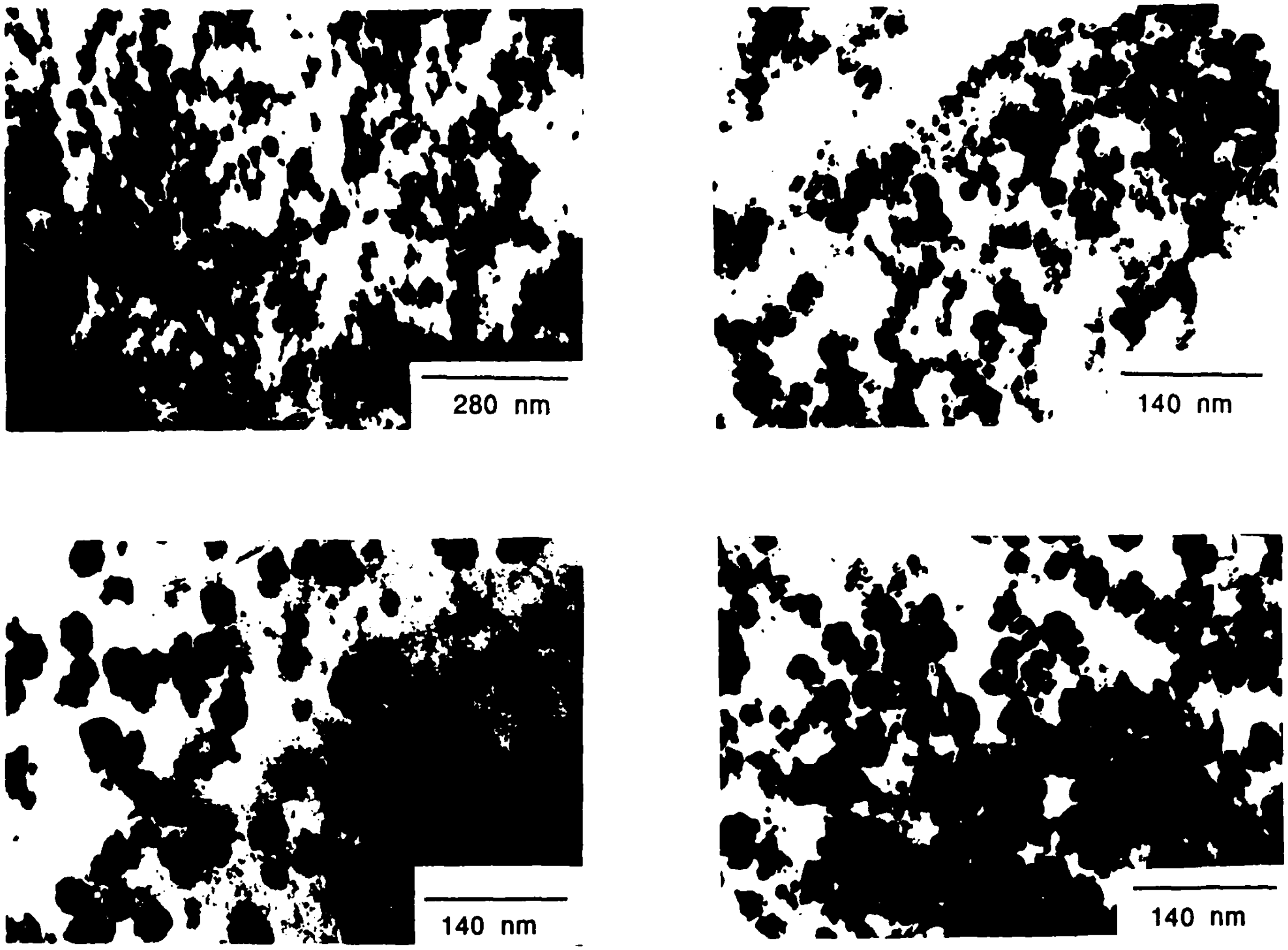
280 nm
140 nm
140 nm
140 nm

Figure 10. TEM micrographs

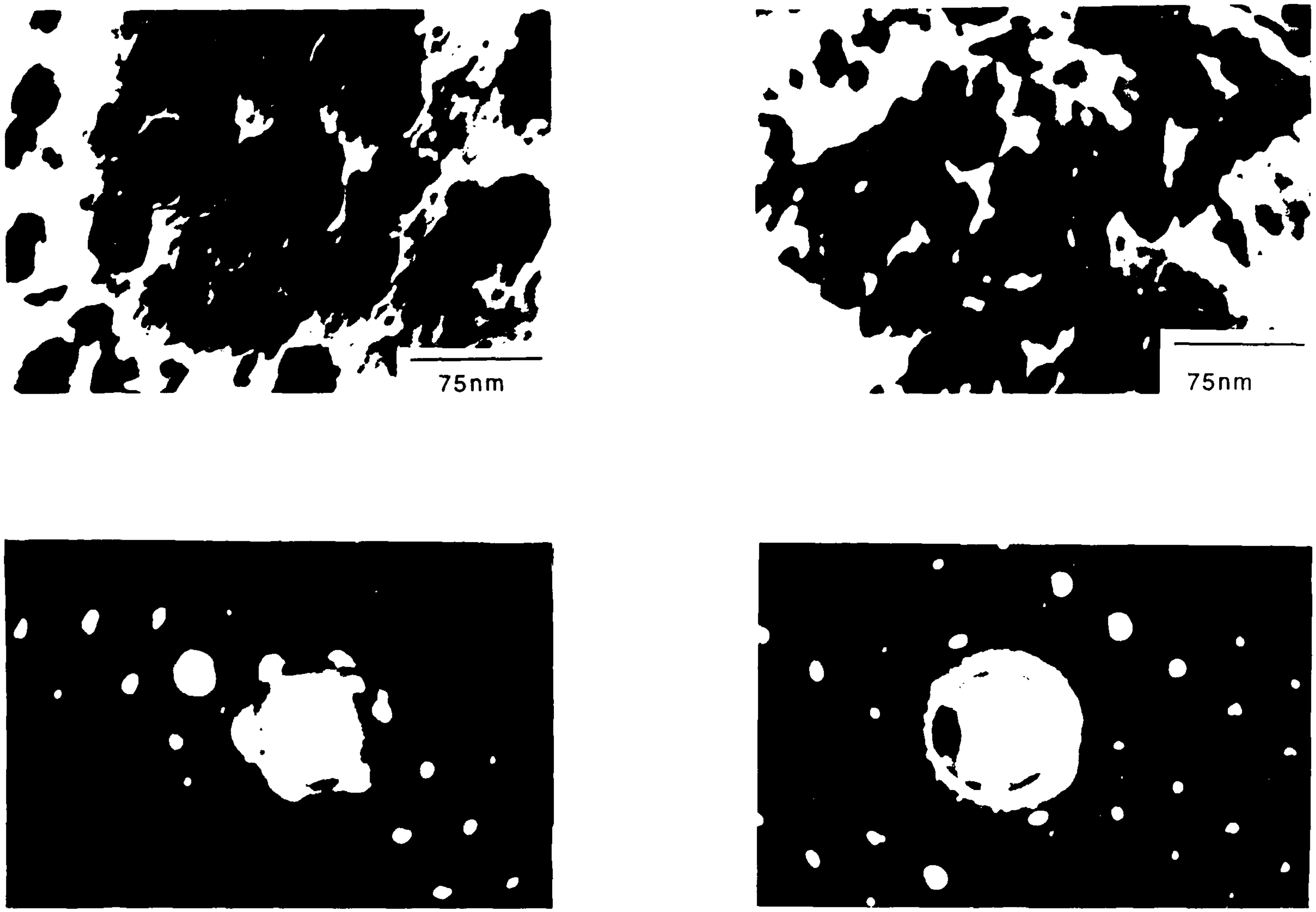

Figure 11. TEM micrographs with corresponding diffraction patterns

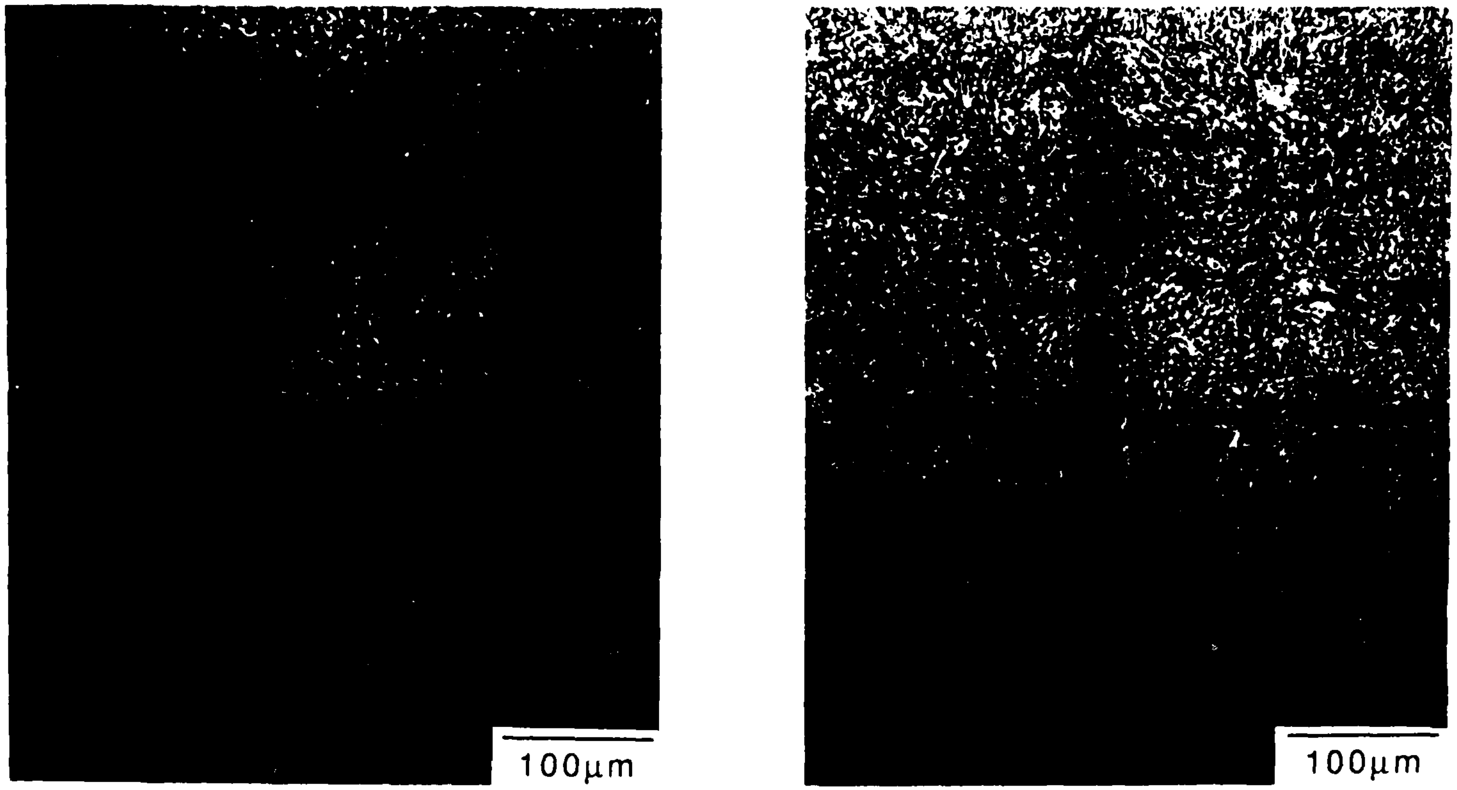
100µm
100µm

AS-ROLLED ROLLED+AGED

Figure 12 Optical micrographs of the as-rolled and rolled+aged samples

## TABLE II : THERMOMECHANICAL PROCESSING SCHEDULE

| RUN 1 | INITIAL THICKNESS (mm) | PASS# | MILL SETTING (mm) | T (°C) MEASURED BEFORE PASS |
|---|---|---|---|---|
| | 22.2 | 1 | 20.6 | 1830 |
| | | 2 | 17.5 | 1620 |
| | | 3 | 15.9 | 1430 *** |
| | | 4 | 14.3 | 1800 |
| | | 5 | 12.7 | 1630 |

| RUN 2 | INITIAL THICKNESS (mm) | PASS# | MILL SETTING (mm) | T (°C) MEASURED BEFORE PASS |
|---|---|---|---|---|
| | 25.4 | 1 | 22.2 | 1900 |
| | | 2 | 20.6 | |
| | | 3 | 17.5 | 1750 |
| | | 4 | 14.3 | |
| | | 5 | 12.7 | 1630 |

| RUN 3 | INITIAL THICKNESS (mm) | PASS# | MILL SETTING (mm) | T (°C) MEASURED BEFORE PASS |
|---|---|---|---|---|
| | 25.4 | 1 | 22.2 | 1882 |
| | | 2 | 20.6 | |
| | | 3 | 17.5 | 1785 |
| | | 4 | 14.3 | |
| | | 5 | 12.7 | 1672 |

| RUN 4 | INITIAL THICKNESS (mm) | PASS# | MILL SETTING (mm) | T (°C) MEASURED BEFORE PASS |
|---|---|---|---|---|
| | 27 | 1 | 23.8 | 1915 |
| | | 2 | 20.6 | |
| | | 3 | 19.1 | 1781 |
| | | 4 | 17.5 | |
| | | 5 | 15.9 | 1650 |
| | | 6 | 12.7 | |
| | | | | TEMP. AFTER ROLLING = 1549 °C |

ALL SAMPLES SOAKED FOR 1 HOUR AT 1125 °C

SURFACE TEMPERATURES WERE MEASURED WITH AN OPTICAL PYROMETER

ALL PIECES WERE AIR COOLED AFTER ROLLING

***REHEATED IN FURNACE FOR 3 MINUTES

TABLE III : CHEMICAL ANALYSIS OF AS SPRAYED HSLA-100

| ELEMENT (*) | C | Mn | P | S | Si | Cu | Ni | Cr | Mo | Al | Nb | N | O |
|---|---|---|---|---|---|---|---|---|---|---|---|---|---|
| | | | | | | | | | | | | | |
| | | | | | | | | | | | | | |
| HSLA-100 | | | | | | | | | | | | | |
| FEEDSTOCK | 0.034 | 0.820 | 0.014 | 0.002 | 0.260 | 1.450 | 3.250 | 0.550 | 0.600 | 0.028 | 0.300 | 140 | 25 |
| | | | | | | | | | | | | | |
| | | | | | | | | | | | | | |
| RUN #1-SIDE (**) | 0.023 | 0.730 | <0.005 | 0.002 | 0.210 | 1.520 | 3.320 | 0.560 | 0.610 | <0.01 | 0.010 | 330 | 63 |
| | | | | | | | | | | | | | |
| RUN #2-TOP (***) | 0.028 | 0.750 | <0.005 | 0.002 | 0.210 | 1.530 | 3.390 | 0.560 | 0.620 | <0.01 | 0.010 | 230 | 46 |
| RUN #2-BOTTOM (****) | 0.034 | 0.750 | <0.005 | 0.002 | 0.210 | 1.530 | 3.360 | 0.550 | 0.610 | <0.01 | 0.010 | 240 | 274 |
| | | | | | | | | | | | | | |
| RUN #3-TOP | 0.026 | 0.770 | 0.014 | 0.002 | 0.240 | 1.450 | 3.250 | 0.550 | 0.600 | 0.006 | 0.030 | 210 | 82 |
| RUN #3-BOTTOM | 0.030 | 0.780 | 0.013 | 0.002 | 0.250 | 1.450 | 3.250 | 0.550 | 0.600 | 0.008 | 0.030 | 230 | 365 |
| | | | | | | | | | | | | | |
| RUN #4-TOP | 0.025 | 0.760 | 0.013 | 0.002 | 0.250 | 1.450 | 3.230 | 0.550 | 0.600 | 0.005 | 0.030 | 310 | 44 |
| RUN #4-BOTTOM | 0.028 | 0.770 | 0.014 | 0.002 | 0.250 | 1.450 | 3.230 | 0.550 | 0.600 | 0.006 | 0.030 | 300 | 30 |
| | | | | | | | | | | | | | |
| RUN #5-SIDE | 0.028 | 0.760 | 0.014 | 0.002 | 0.240 | 1.400 | 3.230 | 0.550 | 0.600 | 0.005 | 0.030 | 280 | 38 |
| | | | | | | | | | | | | | |
| SLOW COOL- | 0.033 | 0.780 | 0.013 | 0.002 | 0.240 | 1.450 | 3.250 | 0.550 | 0.600 | 0.007 | 0.030 | 150 | 49 |
| BOTTOM | | | | | | | | | | | | | |
| OF CRUCIBLE | | | | | | | | | | | | | |

* NITROGEN AND OXYGEN CONCENTRATIONS ARE IN PARTS PER MILLION; ALL OTHER CONCENTRATIONS ARE IN WEIGHT PERCENT

** ANALYSIS SAMPLE TAKEN WITHIN 12.7 mm OF OUTER EDGE OF PREFORM, AT APPROXIMATELY HALF THE TOTAL HEIGHT

*** ANALYSIS SAMPLE TAKEN ALONG SPRAY AXIS, APPROXIMATELY 25 mm FROM TOP OF DEPOSIT.

**** ANALYSIS SAMPLE TAKEN ALONG SPRAY AXIS, APPROXIMATELY 25 mm FROM BOTTOM OF DEPOSIT

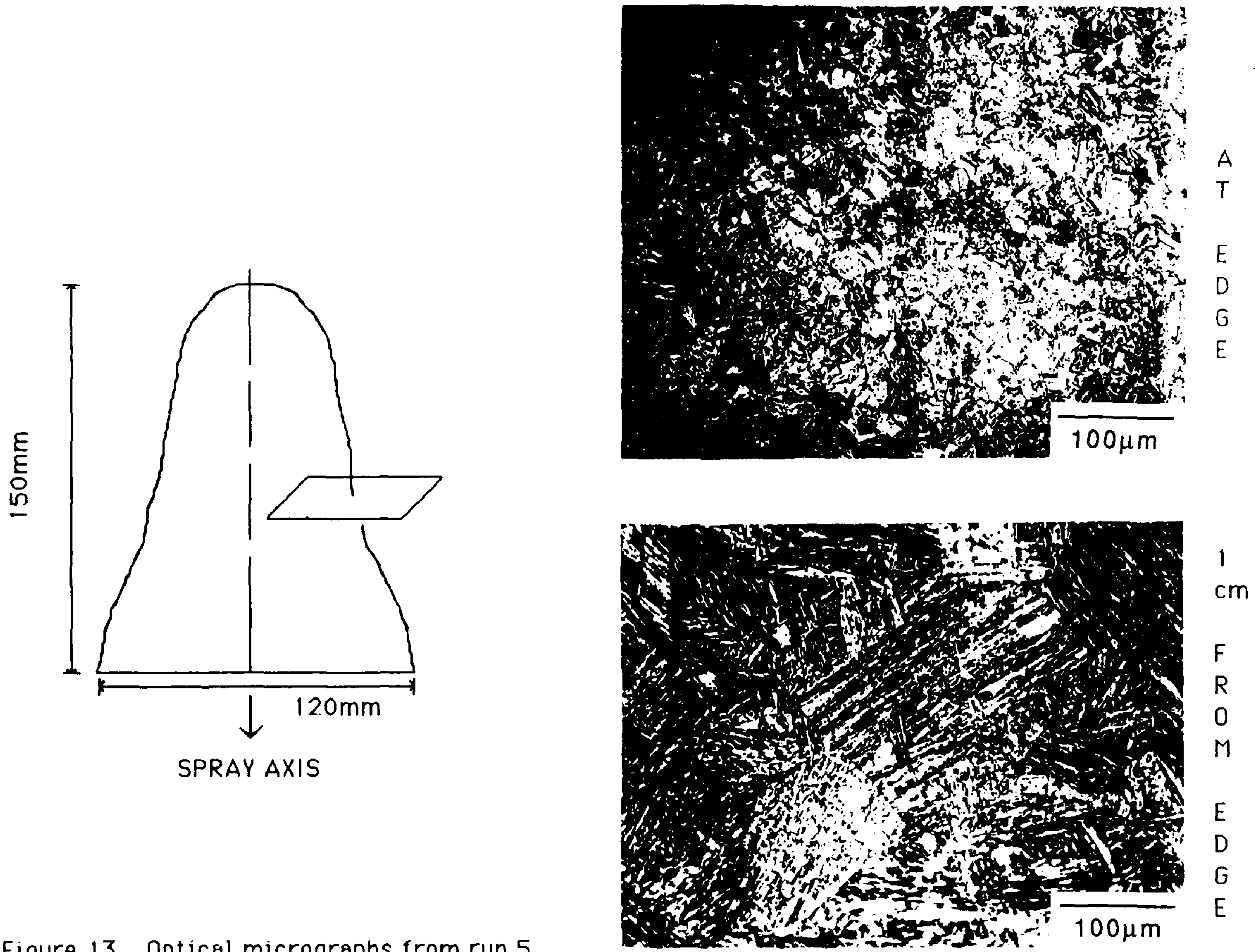
150mm
120mm
SPRAY AXIS
AT EDGE
100μm
1 cm FROM EDGE
100μm

Figure 13. Optical micrographs from run 5.

existed. A possible explanation for the high oxygen levels analyzed at the bottom of runs 2 and 3 (274 and 365 ppm, respectively) and the low oxygen level at the bottom of run 4 (30 ppm) is related to the timing of the nitrogen gas pressure ramp test prior to melting and atomization. It is postulated that in runs 2 and 3, this test was done well before atomization, allowing time for oxygen to egress into the chamber. It is also postulated that the ramp test was done just prior to atomization in run 4, and thus oxygen pick-up in the chamber was minimized.

The data show that more nitrogen was present at the bottom of the preform in run 4 (300 ppm) than was present at the bottom of the preforms in runs 2 or 3 (240 and 230 ppm, respectively). The fact that run 4 was atomized using a gas pressure of 1.0 MPa, and to a lesser extent that the nitrogen gas ramp test was preformed just before atomization, account for the higher nitrogen level in the preform from run 4.

Another way to avoid a high oxygen content in the bottom of the deposit is to spray for a few seconds without a substrate to collect the droplets. These droplets scavenge the chamber of oxygen and are removed from the chamber before the substrate is positioned under the spray.

In addition to aluminum and niobium, other alloying elements decreased in concentration during spray casting, Table III. For example, carbon decreased from 0.04% to 0.03%. It has been shown that at these levels, small differences in carbon content give rise to large differences in hardenability. Hamburg and Wilson showed that HSLA-100 containing 0.06% C was 205 MPa (30 ksi) stronger in the as quenched condition than a 0.04% HSLA-100 [13].

### (b) *Effect Of Process Parameters On Microstructure*

The atomizing gas, usually either nitrogen or argon, serves several functions. First, it breaks up the molten stream into droplets. Second, it accelerates the droplets and directs them towards the substrate. Third, it cools both the droplets and the deposit. Finally, it provides a protective atmosphere which reduces oxygen pick-up throughout the process. The oxygen content in the deposit is generally the same as the feedstock from which it was made [4]. However, this does not appear to hold in these experiments.

An interrelated parameter to the gas pressure is the temperature of the melt. If the melt has too high a superheat, the atomizing gas will not be able to remove the necessary amount of heat energy from the droplets to produce a coherent preform. The liquid layer that exists on the top of the deposit during solidification will exceed a critical thickness, and many benefits inherent to the process will be lost. Any segregation, which would normally be confined to within one splat, can now occur on a larger scale. Additionally, in the preforms made with a rotating substrate, the liquid layer can be accelerated by centrifugal force to the outer edges of the deposit, or off the deposit. The combination of these effects may lead to the formation of large voids in the center of the preform. When making billets, an outside shell will solidify first, leaving a liquid mass in the center of the solidifying deposit. In the final product, this will manifest itself as a cavity. This was the problem in run 1.

Problems are also manifest if the melt superheat is too low. When this happens, droplets will either arrive on the substrate already solidified and will not splat, or they will simply bounce off the substrate. This leads to a large fraction of voids that will not be filled by newly arriving droplets. At a low superheat there is also the danger of the molten metal solidifying in the nozzle due to cooling by the nearby gas jets. This produces what is known as a "freeze-off." One run not included in this study did not pour for this reason.

Another variable that may be changed is the nozzle diameter. Increasing this diameter increases the droplet diameter and the droplet size distribution. Concurrently the cooling efficiency of the atomizing gas is decreased, and thus the spray is hotter with a higher liquid content. By decreasing the nozzle diameter, the spray will be cooler, but the danger of the metal freezing in the nozzle increases. In the present study the nozzle diameter was kept fixed.

Options also exist concerning the cooling of the preform. It is possible to let the preform cool in the spray chamber, place it in a heat insulating box, or to quench it either in an aqueous or gaseous medium. The merit of allowing the preform to cool extremely slowly in an insulating box is that internal delaminations of the preform can be eliminated, thereby increasing macro- and microstructural integrity [25]. The benefit of quenching after spraying is to reduce the amount of grain growth that may occur. As previously stated, quenching produces a fine grain size at the outer edge of the preform, but further inwards the grain size coarsens.

The method by which the as-deposited preform is cooled is easy to control. In this study, the preform either cooled in the spray chamber or was quenched into water. It is difficult to vary the spray temperature and study its effects independent of other process parameters. The position and motion of the substrate, as well as the pressure of the atomizing gas, must be kept constant in order to reliably study the influence of spray temperature on the final product. Although runs 4 and 5 were sprayed with a difference of 50 to 70 °C in melt superheat, the microstructure, porosity, and hardness were similar in both runs.

It was easier to monitor the atomizing pressure. However, this too is not constant for the pressure cycled by ± 0.1 MPa (± 1 bar) during the run. This was dependent on keeping a constant supply pressure, a factor that varied depending on whether the nitrogen supply tank was full or not. Additionally, as the atomizing pressure was increased, it approached the supply pressure (typically 1.2 MPa) which increased the amount of variation in the atomizing pressure. In run 4, a higher atomizing pressure was used than in the other runs. Microstructure, porosity, and hardness, however, did not change significantly.

### (c) *Effect Of Process Parameters On Macrostructure*

The two differences between runs 4 and 5 were the degree of superheat (run 4: $\Delta T$= 120°C, run 5: $\Delta T$= 50°C) and the atomizing gas pressure (run 4: P= 1.0 MPa, run 5: P= 0.9 MPa). These two changes produced a large difference in the overall shape of the preform, as shown in Figure 14. A possible explanation is that since run 4 was atomized with a higher gas pressure, the cross sectional area of the spray was larger. This will give rise to a larger intercept area on the substrate and in turn on the growing deposit. Hence, there will be more droplets available to fill in the outer part of the growing deposit. Changing the superheat is known to vary the size and size distribution of the droplets; the overall shape will not be a function of melt superheat.

### (d) *Thermomechanical Processing*

Fine grain size is touted as a benefit of the Osprey™ spray forming process. Since the aluminum and niobium content of the steel was severely reduced, austenitic grains were allowed to grow without any pinning mechanism to prevent grain growth. Upon transformation to bainite, this manifested itself as a coarse microstructure. The effects of hot rolling this material were studied to see if the properties could be improved over conventionally processed HSLA-100 steels. This was

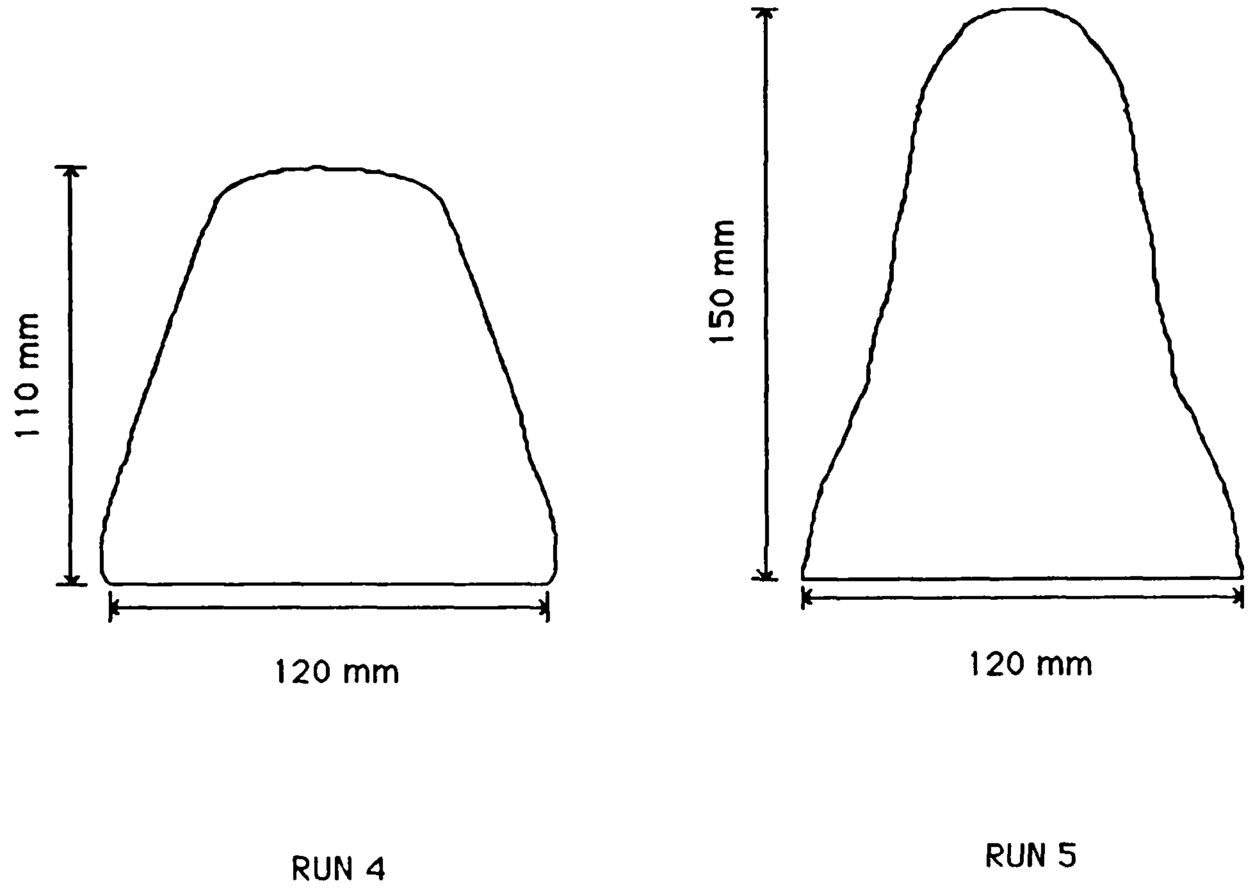
110 mm
120 mm
150 mm
120 mm

RUN 4

RUN 5

Figure 14. Overall shape of runs 4 and 5.

not observed, at least in terms of microstructure, porosity, and hardness. There is a large amount of porosity near the edges of the rolled samples; this is due to edge cracking during rolling. To date, no samples have been taken from the center of the rolled spray cast plate, but it is expected rolling would decrease the pore size in this region.

## SUMMARY AND CONCLUSIONS

- It has been demonstrated that HSLA steels can be spray cast into preforms; microstructural integrity is reflected in an acceptable level/distribution of porosity, and a homogeneous grain structure throughout.
- With the exception of hot tears, the spray cast microstructure of the preforms produced in this study was found to be relatively insensitive to spray processing conditions.
- The prior austenitic grain size in the preforms varied from 100 to 500μm, depending mainly on position in the preform. This larger than expected grain size with a coarse bainitic microstructure is due to the absence of aluminum and niobium in the deposit.
- The grain size of the preforms can be reduced by hot rolling. Results indicate that rolling reduces the grain size to about 100μm. Aging of the rolled HSLA preforms did not significantly alter the microstructure.
- Flexibility in terms of the choice of processing parameters is a major advantage of the spray casting process, particularly for this class of HSLA steels which are difficult to process by conventional ingot metallurgy.

## ACKNOWLEDGEMENTS

This work was sponsored by the Office of Naval Research, Washington, D.C. Thanks are due to G. Vander Voort, Carpenter Technology, for chemical analyses, and B. Bramfitt, Bethlehem Steel Corporation, for making available hot rolling facilities. P. Mathur and G. Gillen assisted with the Osprey runs at Drexel University. K. Kembaiyan and R. Doherty of Drexel University assisted in the interpretation of the diffraction patterns. Personnel at the David Taylor Research Center (A. Moran, W. Palko, M. Vassilaros, E. Czyryca, and P. Kelley) are thanked for their assistance and technical advice.

## REFERENCES

1. P.C. Mathur, D. Apelian and A. Lawley, Acta Metallurgica; Vol. 37, No. 2, p. 429, 1989.
2. S. Annavarapu, D. Apelian and A. Lawley, Met. Trans., Vol. 19A, No. 12, p. 3077, 1988.
3. A.R.E. Singer, Metals and Materials, Vol. 4, p. 246, 1970.
4. Metal Powder Report, Vol. 42, No. 10, p. 712, 1987.
5. R.W. Evans, A.G. Leatham, and R.G. Brooks, Powder Met., Vol. 28, No. 1, p. 13, 1985.
6. R.H. Bricknell, Met. Trans., Vol. 17A, p. 583, 1986.

7. H.C. Fiedler, T.F. Sawyer, and R.W. Kopp, "Spray Forming," G.E. Technical Information Series, Report No. 85CRD073, May 1985.
8. F.B. Pickering, *International Conference on Technology and Applications of HSLA Steels*, organized by M. Korchynsky, 1983, American Society for Metals, Metals Park, Ohio, p.1.
9. A.D. Wilson, E.G. Hamburg, D.J. Colvin, S.W. Thompson, G. Krauss, *Microalloying '88*, 1988, ASM International, Metals Park, Ohio, p. 259.
10. E.G. Hamburg and A.D. Wilson, *Processing, Microstructure and Properties of HSLA Steels,* edited by A.J. DeArdo, 1987, The Metallurgical Society, Warrendale, PA.
11. M.R. Krishnadev, J.T. McGrath, J.T. Bowker, S. Dionne, *Welding Metallurgy of Structural Steels*, edited by J.Y. Koo, 1987, The Metallurgical Society, Warrendale, PA.
12. T.W. Montemarano, B.P. Sack, J.P. Gudas, M.G. Vassilaros, H.H. Vanderveldt, J. Ship Production, Vol. 2, No. 3, p.145, 1986.
13. R.R. Irving, Iron Age, Vol. 2, No. 5, p. 53, 1986.
14. M.T. Miglin, J.P. Hirth, A.R. Rosenfield and W.A.T. Clark, Met. Trans., Vol. 17A, p. 791, 1986.
15. L.G. Kvidahl, Welding Journal, Vol. 64, No.7, p. 42, 1985.
16. G.E. Hicho, C.H. Brady, L.C. Smith, R.J. Fields, DTNSRDC/SME-CR-05-85, September 1985, Final Report.
17. P.P. Hydrean, A.L. Kitchin, F.W. Shaller, Met. Trans., Vol. 2, p. 2541, 1971.
18. E. Hornbogen and R.C. Glenn, Transactions of TMS-AIME, Vol. 218, p. 1064, 1960.
19. S.R. Goodman, S.S. Brenner and J.R. Low, Jr., Met. Trans., Vol.4, p. 2363, 1963.
20. S.R. Goodman, S.S. Brenner and J.R. Low, Jr., Met. Trans., Vol.4, p. 2371, 1963.
21. G.E. Hicho, L.C. Smith, S. Singhal, and R.J. Fields, J. Heat Treating, Vol.3, No. 3, 1984.
22. A.R.E. Singer and R.W. Evans, Metals Tech., Vol. 10, p.61, 1983.
23. Suresh Annavarapu, "Strip Casting of Plain Carbon Steel by Spray Deposition," M.S. Thesis, Drexel University, Philadelphia, Pa., 1987.
24. The Making, Shaping and Treating of Steel, Ninth Edition, edited by H.E. McGannon, United States Steel Corp., 1971.
25. P. Kelley, 1988, David Taylor Research Center, Annapolis, MD., private communication.